UNIVERSITÀ DEGLI STUDI DI PADOVA

Dipartimento di Fisica e Astronomia "Galileo Galilei"

Master Degree in Physics

Final Dissertation

Study of mitigation strategies of beam induced background and Higgs boson couplings measurements at a muon collider.

Thesis supervisor

Prof. Donatella Lucchesi

Thesis co-supervisor

Dr. Lorenzo Sestini

Candidate

Laura Buonincontri

Academic Year 2019/2020

Contents

1 Introduction

The purpose of my thesis is two fold. The first one is to study the properties of the beam-induced background and the proposed mitigation strategies that are necessary to reduce it with full detector simulation at muon collider. In this environment the reconstruction of physical objects, like hadronic jets produced by the fragmentation of quarks, is studied. The second one is the evaluation of the sensitivity on the Standard Model (SM) production cross section measurement of the process $\mu^+\mu^- \to HH\nu\bar{\nu} \to b\bar{b}b\bar{b}\nu\bar{\nu}$ at 3 TeV center of mass energy. This analysis is the foundation for the evaluation of the sensitivity on the determination of the Higgs boson trilinear self-coupling at a muon collider. The trilinear and quadrilinear Higgs self-couplings determine the shape of the Higgs potential, which rule the Electroweak Simmetry Breaking. They have never been measured directly at colliders due to the low production cross section of double and triple Higgs and even at future pp and e^+e^- colliders they can not be determine with enough precision to resolve the Higgs potential. The LHC (Large Hadron Collider) is measuring and will measure the Higgs couplings to bosons and fermions. Current results are in agreement with the SM within the precision reached so far.

The goals of the scientific program of the Higgs boson physics at Future Colliders are: the improvement of the precision on the fermions and bosons coupling measurements, as deviation from the SM could reveal New Physics, and measurement of Higgs boson self-couplings.

The muon collider is a possible future machine in which these physics goals can be reached with enough precision. Indeed, at the high center of mass energies, in the regime of multi-TeV and with the luminosity conditions that are foreseen for such a machine, the single, double and triple Higgs bosons production rates will be high enough to meet the required precision and determine the Higgs potential shape opening a window to cosmological tests.

However, physics measurements at muon collider are strongly affected by the huge amount of background which comes from the muon decays along the beam line. Secondary and tertiary particles produced in the interaction of the muon decay products with the machine-detector interface components can reach the detector and affect its performance. For this reason mitigation strategies have to be applied in order to perform physics measurements.

This thesis is structured as follow:

1. **Chapter 2: Theoretical introduction on Higgs boson physics**
   In the first chapter an overview of the Electroweak theory and of the Brout-Englert-Higgs mechanism of the symmetry breaking will be given. Most recent measurements of the Higgs boson branching ratios and its couplings to bosons and heavy quarks, performed at LHC, will be also presented. The single, double and triple Higgs production processes and trends of relative cross sections as a function of the center of mass energy at future hadrons and lepton colliders will be described. An overview of the expected uncertainties on Higgs couplings, with respect to the SM predictions, at the Future Colliders will be also given.

2. **Chapter 3: Studies of Muon Collider machine and detector**
   In this chapter the muon accelerator scheme developed by the Muon Accelerator Program (MAP) will be presented, starting from the muon production up to the acceleration section. The main technical issues regarding the muon collider and the detector are also described. In particular the beam-induced background composition and mitigation strategies will be discussed. The beam-induced background can be mitigated by inserting two cone-shaped tungsten nozzles inside the detector, which stop part of the background particles at the entrance of the detector. Nevertheless, the flux of particles surviving the shielding is very high. Then by exploiting the time information from the detectors a further reduction, during the data taking, can be obtained. This idea is based on the fact that the time of arrival at the detector components of particles generated in the primary muons collision is different from that of the beam-induced background particles, which can be generated several meters from

the interaction point. By tuning the acquisition time window of the detectors a part of the beam-induced background can be rejected, while keeping most of the physics signal. For this purpose the development of tracker systems and calorimeter detectors providing spatial and time information will be very important in the design of a muon collider detector. Further strategies that are still under study will be also discussed.

3. **Chapter 4: Detector description**
   In this chapter the simulated detector provided by the ILCSoftware framework, which is the software used to perform the full simulation of the process mentioned above, will be described.

4. **Chapter 5: Study of the beam-induced background effects on detector components**
   Effects of the beam-induced background on the detector will be presented. In this chapter the characteristic distributions of the time of arrival of the beam-induced background particles on the detectors are compared to the signal distributions and the relative cuts on the tracker system are determined. The effects of beam-induced background particles on the calorimeter are also presented and discussed.

5. **Chapter 6: Events reconstruction**
   In this chapter the main algorithms used for the particle identification and tracks and jets reconstruction, implemented in the software framework, will be presented, focusing on their functioning and performances. The b-tagging algorithm used to identify jets generated from b-quarks, characterized in previous studies for the determination of the precision on Higgs coupling to b-quark, will be described for what concerns the usage in my thesis.

6. **Chapter 7: Double Higgs boson reconstruction in $b\bar{b}b\bar{b}$**
   In this chapter the methods used for the generation, simulation and reconstruction of the process $\mu^+\mu^- \to HH\nu\bar{\nu} \to b\bar{b}b\bar{b}\nu\bar{\nu}$ and the physics background will be discussed. The signal to background separation will be performed by mean of a Multivariate Analysis based on Boosted Decision Trees (BDT). Quantities relative to the signal and background events are used as input for the BDT, which exploits correlations between them to classify the events. The event selection for the final calculation of the uncertainty on the cross section relies on the BDT output and on the b-tagging. The final result is presented and discussed together with its implications.

2 Higgs boson physics

2.1 Higgs boson in the Standard Model

The Standard Model provides the mathematical framework which gives a quantum-mechanical description of electromagnetic, weak and strong interactions based on fundamental constituents, fermions, interacting via force carriers, photons, W and Z bosons, and gluons. It is based on the gauge symmetry $SU(3)_C \times SU(2)_L \times U(1)_Y$, with the colour group $SU(3)_C$ for the strong interaction and with $SU(2)_L \times U(1)_Y$ for the electroweak interaction spontaneously broken by the Higgs mechanism. Explicit calculations of the electroweak symmetry breaking can be found in [1], here the main concepts are reported.

To break the gauge invariance spontaneously, the Higgs field is introduced in the electroweak theory. The Higgs field is a spin-zero field, a doublet under SU(2), it has $Y = \frac{1}{2}$ hypercharge, and it is a singlet in color space. The dynamics of the Higgs field is described by the Lagrangian density:

$$\mathcal{L}_{Higgs} = (D^\mu \Phi)^\dagger D_\mu \Phi - V(\Phi) \tag{2.1}$$

Φ is the scalar doublet of the Higgs field:

$$\Phi = \frac{1}{\sqrt{2}} \begin{pmatrix} \phi_1 + i\phi_2 \\ \phi_3 + i\phi_4 \end{pmatrix} \tag{2.2}$$

where ϕ_1, ϕ_2, ϕ_3, ϕ_4 are real scalar fields. D_μ is the covariant derivative, defined as:

$$D_\mu = \partial_\mu + \frac{i}{2} g \tau_j W_\mu^j + \frac{i}{2} g' B_\mu$$

where $j = 1, 2, 3$, τ_j are Pauli martices, W_μ^j and B_μ are the gauge fields, g is the weak coupling constant and g' is the coupling constant related to $U_Y(1)$ gauge symmetry. $V(\Phi)$ is the Higgs potential

$$V(\Phi) = \mu^2 \Phi^\dagger \Phi + \lambda (\Phi^\dagger \Phi)^2 \tag{2.3}$$

λ and μ are real constants related to the shape of the Higgs potential. $\lambda > 0$ is required to ensure the potential is bounded from below, guaranteeing the presence of a ground state. $\mu^2 < 0$ is required, as the potential presents a continuum infinite configurations of minimum energy. The choice of a particular ground state leads to spontaneous symmetry breaking. The expression for the Higgs field expansion around the vacuum (the chosen minimum of the Higgs potential), in the unitary gauge is

$$\Phi = \frac{1}{\sqrt{2}} \begin{pmatrix} 0 \\ v + h(x) \end{pmatrix} \tag{2.4}$$

where

$$v = \sqrt{\frac{-\mu^2}{\lambda}}$$

is the vacuum expectation value and $h(x)$ is the real scalar field of the Higgs boson. With this choice the $SU(2)_L \times U(1)_Y$ symmetry gets spontaneously broken to the electromagnetic subgroup $U(1)_{QED}$, which by construction still remains a true symmetry of the vacuum. By inserting this expression into 2.1, it becomes:

$$\mathcal{L}_{Higgs} = \frac{1}{2} \partial_\mu h \partial^\mu h + (v + h)^2 \left[\frac{g^2}{4} W_\mu^\dagger W^\mu + \frac{1}{8} (g^2 + g'^2) Z_\mu^\dagger Z_\mu \right] - \lambda v^2 h^2 - \lambda v h^3 - \frac{\lambda}{4} h^4 \tag{2.5}$$

Here the gauge fields are expressed in terms of the physical fields W_μ^+, W_μ^-, Z_μ and the Weinberg angle $\sin(\theta_W)$:

$$\begin{aligned} W_\mu^+ &= \frac{1}{\sqrt{2}}(W_\mu^1 - iW_\mu^2) \\ W_\mu^- &= \frac{1}{\sqrt{2}}(W_\mu^3 + iW_\mu^4) \\ Z_\mu &= \cos(\theta_W)W_\mu^3 - \sin(\theta_W)B_\mu \\ A_\mu &= \sin(\theta_W)W_\mu^3 + \cos(\theta_W)B_\mu \end{aligned} \tag{2.6}$$

From the second term in 2.5 the expressions for the Z and $W^\pm$ vector boson masses can be extracted:

$$\begin{aligned} m_{W+} = m_{W-} &= \frac{gv}{2} \\ m_Z = \frac{2\sqrt{g^2+g'^2}}{2} &= \frac{m_W}{cos(\theta_W)} \end{aligned} \tag{2.7}$$

The Higgs boson mass is given by the coefficient of the h^2 term.

$$m_H = \sqrt{2\lambda v^2} \tag{2.8}$$

The couplings between the single and double Higgs and vector bosons are expressed as:

$$\begin{aligned} g_{HWW} &= \frac{g^2}{2}v = \frac{2m_W^2}{v} \\ g_{HZZ} &= \frac{g^2+g'^2}{4}v = \frac{m_Z^2}{v} \\ g_{HHWW} &= \frac{g^2}{4} = \frac{2m_W^2}{v^2} \\ g_{HHZZ} &= \frac{g^2+g'^2}{8} = \frac{m_Z^2}{2v^2} \end{aligned} \tag{2.9}$$

The coefficients of the h^3 and h^4 terms give the trilinear and quadrilinear Higgs self-couplings.

$$\begin{aligned} \lambda v h^3 &= \frac{m_H^2}{2v^2}vh^3 = \lambda_3 v h^3 \\ \frac{\lambda}{4}h^4 &= \frac{1}{4}\frac{m_H^2}{2v^2}h^4 = \frac{1}{4}\lambda_4 h^4 \end{aligned} \tag{2.10}$$

In the SM notation λ_3 and λ_4 are equal and expressed as:

$$.\lambda_3 = \lambda_4 = \frac{m_H^2}{2v^2} \tag{2.11}$$

In this chapter they are assumed different in order to be model independent. The mass terms for quarks and charged leptons after the spontaneous symmetry breaking of the Higgs field can be introduced by mean of the Yukawa couplings. For leptons:

$$\mathcal{L}_{Yukawa} = -g_k \bar{l}_L^k \Phi e_R^k - Y_{ij}^u \bar{q}_L^i \tilde{\Phi} u_R^j - Y_{ij}^d \bar{q}_L^i \Phi d_R^j + h.c. \tag{2.12}$$

The index k in the first term runs on the three flavours of leptons, while i, j are the quarks flavour. The coupling constants to the flavour k are g_k, and Y_{ij}^u and Y_{ij}^d are the matrices that contain

the Yukawa coupling constants to quarks. L and R refer, respectively to the left and right chiral projections of the spinors:

$$\begin{aligned} \psi_L &= \frac{1+\gamma^5}{2}\psi \\ \psi_R &= \frac{1-\gamma^5}{2}\psi \end{aligned} \tag{2.13}$$

$$l_L^i = \begin{pmatrix} e_L \\ \nu_e, L \end{pmatrix}, \begin{pmatrix} \mu_L \\ \nu_\mu, L \end{pmatrix}, \begin{pmatrix} \tau_L \\ \nu_\tau, L \end{pmatrix} \tag{2.14}$$

$$l_R^i = e_R, \mu_R, \tau_R \tag{2.15}$$

$$q_L^i = \begin{pmatrix} u_L \\ d_L \end{pmatrix}, \begin{pmatrix} c_L \\ s_L \end{pmatrix}, \begin{pmatrix} t_L \\ b_L \end{pmatrix} \tag{2.16}$$

$$\begin{aligned} u_R^i &= u_R, c_R, t_R \\ d_R^i &= d_R, s_R, b_R \end{aligned} \tag{2.17}$$

By introducing in the Lagrangian of equation 2.12, the Higgs field of equation 2.4 the lepton masses are:

$$m^l = \frac{g^l v}{2} \tag{2.18}$$

In order to obtain the quark masses it is necessary to diagonalize the Y^u and Y^d matrices. A unitary transformation V allows to write:

$$M^u = \begin{pmatrix} m_u & 0 & 0 \\ 0 & m_c & 0 \\ 0 & 0 & m_t \end{pmatrix} = \frac{v}{\sqrt{2}} V_L^u Y^u V_R^u$$

$$M^d = \begin{pmatrix} m_d & 0 & 0 \\ 0 & m_s & 0 \\ 0 & 0 & m_b \end{pmatrix} = \frac{v}{\sqrt{2}} V_L^d Y^d V_R^d$$

Within the Standard Model the Higgs potential is fully characterized by two parameters, m_h and v, free parameters of the theory to be determined experimentally. The vacuum expectation value, v, is inferred by the measurement of the Fermi constant known with a precision of 0.6 ppm from muon decay measurement, $v = 1/\sqrt{\sqrt{2}G_F} \sim 246$ GeV [2]. The mass of the Higgs boson is measured to be $m_H = 125.10 \pm 0.14$ GeV [2]. Trilinear and quadrilinear Higgs self-coupling given by equation 2.11 are then:

$$\lambda_3 = \lambda_4 \sim 0.13$$

New physics can modify the Higgs potential giving different values of λ_3 and λ_4 [3].

2.1.1 Higgs properties measurements at LHC

In order to test the Standard Model assumptions, the Higgs boson couplings to fermions and bosons need to be determined experimentally. The signal strength modifier μ is defined as the ratio between a measured Higgs boson process and its SM expectation value. For each specific process $i \to H \to f$ the μ_i^f is defined as:

$$\mu_i^f = \frac{\sigma_i BR^f}{\sigma_{SM} BR_{SM}}$$

Here σ^i with i=ggH, Vector Boson Fusion (VBF), WH, ZH, ttH and BR^f with f=ZZ, WW,$\gamma\ \gamma$,$\tau\tau$, bb, $\mu\mu$ are respectively, the production cross section for $i \to H$ and the branching fraction for $H \to f$. Expressions for the production μ_i and the decay μ_f can be separated into:

$$\mu_i = \frac{\sigma^i}{\sigma_{SM}}$$

$$\mu_f = \frac{BR^f}{BR_{SM}}$$

Figure 1 shows the combined results of μ_i (left) and μ^f (right) measurements obtained by the ATLAS and CMS experiments [2] [4]. All combined results are in agreement with the Standard Model prediction within 2σ. Only the ttH production signal strength shows a higher displacement from 1, but is however compatible within 2.3σ with the Standard Model.

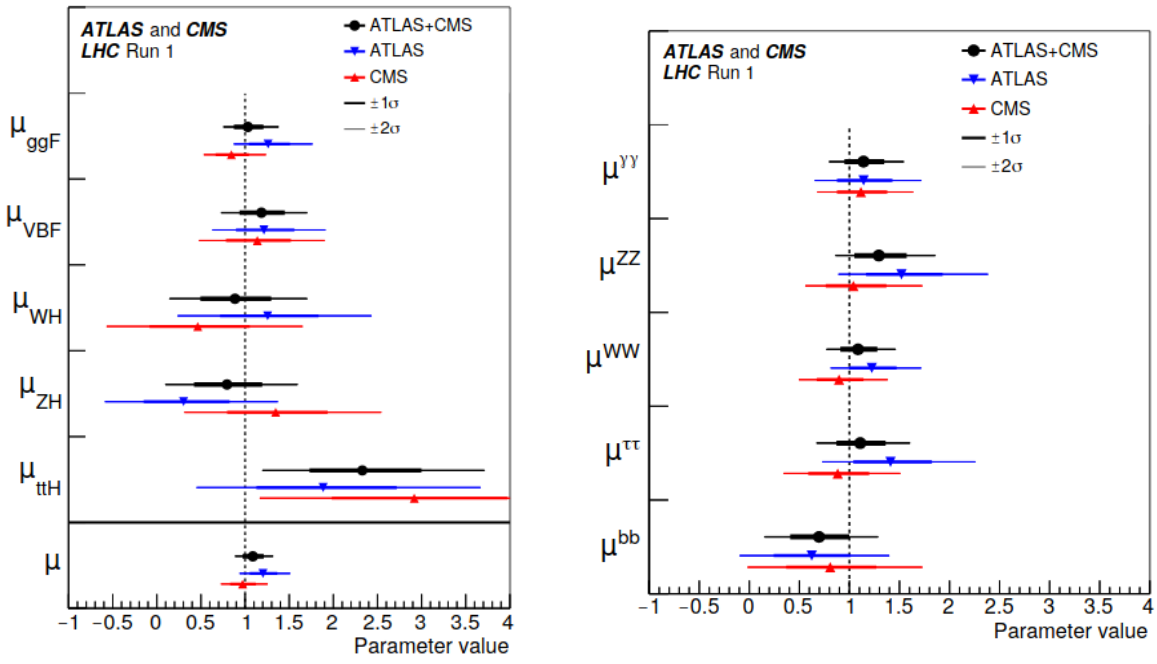

Figure 1: Left: Higgs production signal strength measurements at the ATLAS (blue points) and CMS (red points) experiments and combined results (black points). The cross section in the production modes are measured by $\mu^f = 1$. Right: signal strength measurements for the five Higgs boson main decay modes measured by the ATLAS (blue points) and CMS (red points) experiments and combined results (black points). The branching ratios in the decay modes are measured by assuming $\mu_i = 1$. In both Figures the error bars indicate the 1σ (thick lines) and the 2σ (thin lines) intervals.

2.1.2 Higgs boson couplings

Once the Higgs mass is known, the branching ratio can be fixed by the theory. In Figure 2 the variation of the branching ratio as a function of the Higgs mass is presented. The width of each curve represents the error. As seen in 2.1 coupling of fermions with Higgs particles grows linearly with the fermion mass, while the HWW and HZZ vertices are proportional to m_W^2 and m_Z^2, respectively. Therefore, the Higgs boson is favoured to decay into the heaviest kinematically accessible particle, which is the $b\bar{b}$ pair. The couplings to electrons, muons and light quarks (u,d,s) are extremely small. The Higgs boson decay modes and the relative branching ratio are summarized in Table 1.

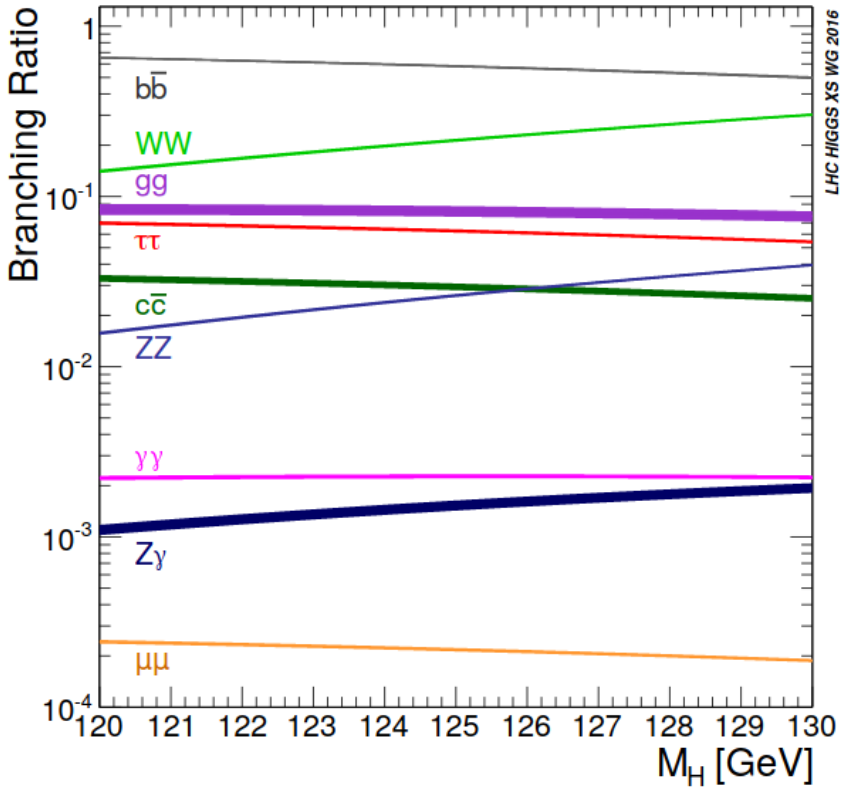

Figure 2: Branching ratios for different Higgs decay modes as a function of the Higgs mass [2]

Decay mode	Branching fraction	Rel. uncertainty [%]
$H \to bb$	5.82×10^{-1}	$^{+1.2\%}_{-1.3\%}$
$H \to WW$	2.14×10^{-1}	$\pm 1.5\%$
$H \to \tau\tau$	6.27×10^{-2}	$\pm 1.6\%$
$H \to cc$	2.89×10^{-2}	$^{+5.5}_{-2.0}$
$H \to ZZ$	2.62×10^{-2}	$\pm 1.5\%$
$H \to \gamma\gamma$	2.27×10^{-3}	$\pm 2.1\%$
$H \to Z\gamma$	1.53×10^{-3}	$\pm 5.8\%$
$H \to \mu\mu$	2.18×10^{-4}	$\pm 1.7\%$

Table 1: Branching fraction for different Higgs decay modes [2]

The current measurements of the Higgs boson properties are limited to the couplings of the Higgs boson to the SM particles except the neutrinos. The *kappa* framework is used to characterize the Higgs coupling properties in terms of a series of Higgs coupling stregth modifier parameters which are defined as the ratio of the couplings of the Higgs boson to a given elementary particle to their corresponding Standard Model values. Within the *kappa* framework the cross section times the branching ratio can be decomposed as:

$$(\sigma \cdot BR)(i \to H \to f) = \frac{\sigma_i \Gamma_f}{\Gamma_H} \tag{2.19}$$

where σ_i is the production cross section through the initial state i, Γ_f is the partial decay width into the final state f and Γ_H is the total width if the Higgs boson.

The κ parameters are introduced to express each component of eq. 2.19 as the Standard Model expectation values multiplied by the square of a coupling strength modifier. In this way the rate relative to the SM expectation μ_i^f becomes:

$$\mu_i^f = \frac{(\sigma \cdot BR)(i \to H \to f)}{\sigma_{SM} BR_{SM}} = \frac{\kappa_i^2 \kappa_f^2}{\kappa_H^2} \tag{2.20}$$

where κ_H^2 is the expression that adjust the SM Higgs width to take into account modifications, κ_i, of the SM Higgs coupling strength:

$$\kappa_H^2 = \sum_j \frac{\kappa_j^2 \Gamma_j^{SM}}{\Gamma_H^{SM}} \tag{2.21}$$

This notation is introduced to parameterise possible deviations from the SM prediction where κ_i are equal to one.

Current results on measurements of the the Higgs boson couplings to gauge bosons, fermions and self-couplings are summarised in Figure 3 where they are compared to SM predictions [4]. On the y axis the couplings to fermions and weak vector bosons, defined as $\kappa_f \cdot \frac{m_f}{v}$, $\kappa_V \cdot \frac{\sqrt{m_V}}{v}$, are shown as a function of the particle mass. The dashed blue line indicates the predicted dependence of the couplings on the particle mass in the case of the SM. The solid red line indicates the best fit result in the phenomenological model of Ref. [5] with the corresponding 68% and 95% CL bands. From these plots it is possible to conclude that the Higgs properties measured at the LHC Run I and Run II agree with the theoretical predictions within experimental and theoretical errors.

For what concerns the Higgs self-couplings, as can be seen from Figure 5, the cross section is predicted to be about three orders of magnitude smaller than the single Higgs production at the LHC at 14 TeV, which makes these measurements very challenging. To fully exploit the 14 TeV energy regime, an upgrade of LHC, the High Luminosity LHC (HL-LHC), is scheduled to start operation in 2026, with the aim of increasing the luminosity (and hence collision rate) by a factor of 5 beyond the design value of LHC. The LHC high luminosity phase (HL-LHC) will improve the accuracy of the measurements of the Higgs-boson couplings to the vector bosons and third generation, and access for the first time the couplings to the second generation fermions. Nine coupling modifiers corresponding to the Higgs boson couplings to the standard model particles $(\kappa_W, \kappa_Z, \kappa_t, \kappa_b, \kappa_\tau, \kappa_\mu, \kappa_\gamma, \kappa_{Z\gamma}, \kappa_g)$ are presented in Figure 4, and are compared for LHC and HL-LHC. In this case the κ framework is extended to allow for the possibility of Higgs boson decays to invisible or unrevealable beyond the standard model particles. This aspects are taken into account by modifying the Higgs total width

$$\Gamma_H = \frac{\Gamma_H^{SM} \kappa_H^2}{1 - (BR_{inv} + BR_{unr})} \tag{2.22}$$

where BR_{inv} is the branching ratio of the Higgs decay to invisible particles and BR_{unr} is the branching ratio to unrevealable particles. For details see ref. [3].

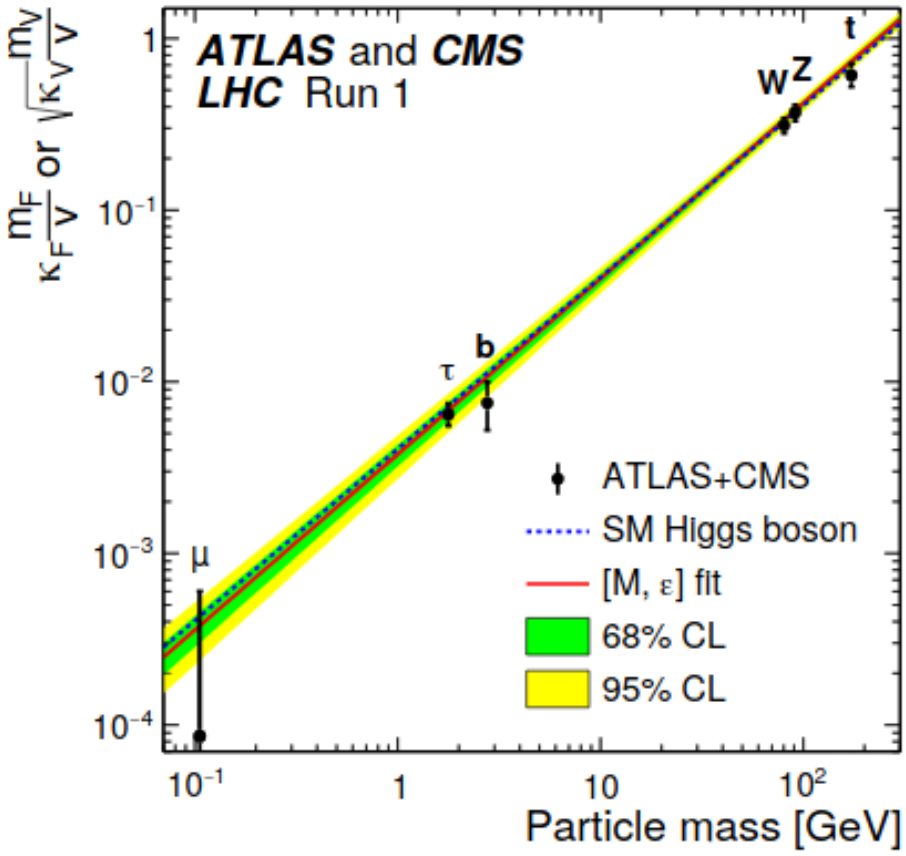

Figure 3: Combined results of the measurements of the Higgs couplings at ATLAS and CMS Run I, as a function of the particle masses. Blue dashed line represents the Standard Model prediction. The solid (red) line indicates the best fit result to the $[M, \epsilon]$ phenomenological model [4].

2.2 Higgs boson physics at Future Colliders

A precise determination of the Higgs boson's properties is one of the main goals at Future Colliders. In order to verify the SM a precision on the Higgs coupligs around 1% is required. Furthermore direct measurements of the trilinear and quadrilinear Higgs self-couplings will not be possible at LHC or HL-LHC. Multi-TeV center of mass energies would allow the discovery of new heavy particles with mass at the TeV scale. Furthermore the cross section of some challenging processes which are actually difficult to measure grows up with the center of mass energy, while high luminosity will increase the number of interaction per bunch crossing. The number of signal events for a certain process in a collider depends from the luminosity and the cross section:

$$N_{sign} = \sigma_{sign} L_{int}$$

where N_{sign} is the number of signal events, σ_{sign} is the signal cross section, L_{int} is the integrated luminosity ($L_{int} = \mathcal{L} \cdot t$, where $\mathcal{L}$ is the istantaneous luminosity and t the time of data collection).

Increased statistics allows for more precise measurement and the possibility to observe rare processes. Then at Future Colliders the production of interesting processes, such as single and double Higgs production, can be greatly enhanced (in next section a more precise description will be given).

Some of the proposed project for future colliders are Future Circular Collider (FCC)[7], the International Linear collider (ILC) [8], the Compact Linear Collider (CLIC)[9] and the Circular

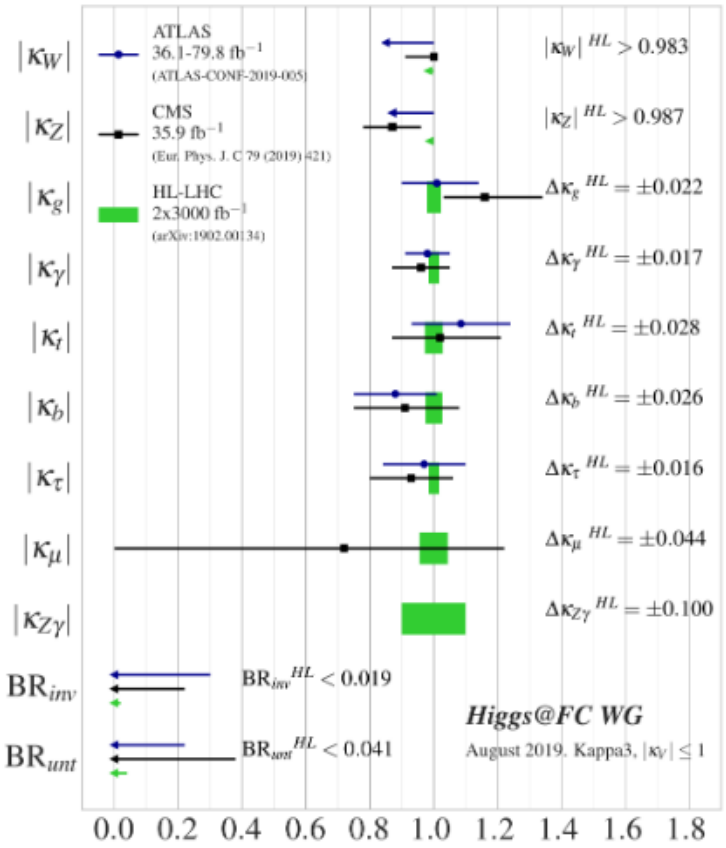

Figure 4: Relative precision on Higgs coupling modifiers, determined by ATLAS and CMS with the LHC data, and as expected for HL-LHC. Constraints on the BR_{inv} and BR_{unt} are also shown [6].

Electron-Positron Collider (CEPC) [10]. The Future Circular Collider (FCC) is a proposed post-LHC particle accelerator, hosted in a 100 km tunnel at CERN which developed and evaluated three accelerator concepts for its conceptual design report:

- FCC-ee: is a lepton collider which would operate at multiple centre of mass energies (from 91 GeV to 365 GeV);
- FCC-hh: is a proton proton collider with the goal to reach center-of-mass collisions energies of 100 TeV;
- FCC-he: is a proton- electron collider with 50 TeV proton beams colliding with 60 GeV electrons.

Compact Linear Collider, CLIC , is a proposed e^+e^- collider at the TeV scale. CLIC is intended to be built and operate at collision energies of 380 GeV to 3 TeV, for a site length ranging from 11 to 50 km respectively.

The Circular Electron Positron Collider (CEPC) is a large international scientific facility to be hosted in China in a circular underground tunnel of approximately 100 km in circumference.

The International Linear Collider (ILC) is a proposed linear particle accelerator. It is planned to have a collision energy of 250 GeV initially, with the possibility for later upgrades up to 1 TeV.

A brief summary of the proposed Future Colliders and their characteristics in terms of luminosity and time is presented in table 2

Collider	Type	$\sqrt{s}$	$\mathcal{L}_{inst}$ $[10^{-34} cm^{-2} s^{-1}]$	$\mathcal{L}$ $[ab^{-1}]$	Time [years]	Refs	Abbreviation
FCC-hh	pp	100 TeV	30	30.0	25	[7]	FCC-hh
FCC-ee	ee	91 GeV	100/200	150	4	[7]	
		160 GeV	25	10	1-2		
		240 GeV	7	5	3		FCC-ee$_{240}$
		365 GeV	0.8/1.4	1.5	5		FCC-ee$_{365}$
FCC-he	ep	3.5 TeV	1.5	2.0	25	[7]	FCC-eh
CEPC	ee	91 GeV	17/32	16	2	[10]	CEPC
		160 GeV	10	2.6	1		
		240 GeV	3	5.6	7		
CLIC	ee	380 GeV	1.5	1.0	8	[9]	CLIC$_{380}$
		1.5 TeV	3.7	1.5	7		CLIC$_{1500}$
		3.0 TeV	6.0	5.0	8		CLIC$_{1000}$
ILC	ee	250 GeV	1.35/1.7	2.0	11.5	[8]	ILC$_{365}$
		350 GeV	1.6	0.2	1		ILC$_{350}$
		500 GeV	1.8/3.6	4.0	8.5		ILC$_{500}$
		1000 GeV	3.6/7.2	8.0	8.5		ILC$_{1000}$

Table 2: Summary of the Future Colliders considered in this section in terms of operative center of mass energy $\sqrt{s}$, integrated ($\mathcal{L}$) and instantaneous luminosity $\mathcal{L}_{inst}$ and time years [3]

Circular muon colliders have the potential to reach center of mass energies of tens of TeV. As will be explained in the next chapter, the muon collider is still under development, therefore the characteristic parameters like center of mass energies and istantaneous luminosity are not established yet. Working hypothesis are given in Table 3.

Collider	Type	$\sqrt{s}$	$\mathcal{L}_{inst}$ $[10^{-34}$ cm^{-2} s$^{-1}]$	$\mathcal{L}$ [ab^{-1}]	Time [s]
Muon Collider	$\mu\mu$	1.5	1.25	0.5	$4 \cdot 10^7$
		3.0	4.4	1.3	
		10	20	8.0	

Table 3: Characteristic parameters of a muon collider [11]

In the following section 2.2.1 the production mechanisms with the relative cross sections are presented for each future collider. The performance of such colliders are also discussed.

2.2.1 Higgs production at hadron and lepton colliders

The SM Higgs boson production cross sections in pp collisions as a function of the center of mass energy ($\sqrt{s}$) up to 100 TeV are reported in Figure 5. Higgs production can happen through five main process:

1. Gluon fusion $gg \to H$. Since no direct gluon-Higgs coupling exists within the Standard Model, the process is mediated at leading order by a massive fermion loop. Main contribution to the loop comes from the top quark.

2. Vector Boson Fusion (VBF) $qq \to VV \to H$ in which the Higgs is produced from a W^+ W^- or ZZ pair originated by initial state quarks with a change of flavour in the case of W boson.

3. Associated production $qq \to Z/WH$. Here a off-shell gauge boson produced at tree level from a quark-quark interaction, generates a W/Z and Higgs.

4. Associated $t\bar{t}H$ higgs production $gg \to t\bar{t}H$.

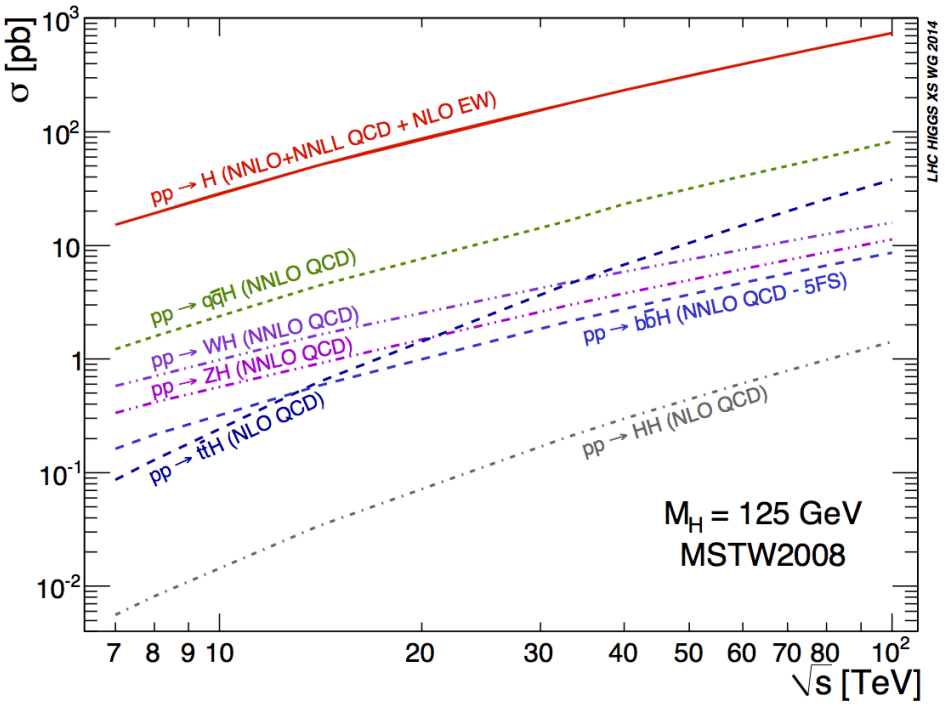

Figure 5: Higgs boson production cross section in a pp collider as a function of the center of mass energy [12]

As can be seen from Figure 5 the cross section of Higgs production grows with the increasing of the center of mass energy up to order of magnitude.

In a lepton collider, the Higgs production mechanism strongly depends from the center of mass energy. In Figure 6 the cross sections for Higgs production is reported for center of mass energies up to 30 TeV. At center of mass energy $\sqrt{s} < 1$ TeV the higgs-strahlung process in which Higgs is emitted by an off shell Z dominates. At energies well above 1 TeV, the VBF production process becomes the most relevant.

2.2.2 Double and triple Higgs production at hadron and lepton colliders

Information on trilinear and quadrilinear couplings are experimentally accessible through double and triple Higgs production processes. At pp colliders, Higgs pairs are produced through gluon fusion, vector boson fusion, and double Higgs-strahlung, whose main representative digrams can be seen in Figure 7. Among all these processes only three contains the triple Higgs vertex, and are highlighted with a red circle. As can be seen in Figure 8 the gluon-gluon fusion remains the dominant process over the entire range of different centre of mass energies, also in Higgs pair production.

The dominant triple Higgs production mechanism is gluon fusion, mediated by a heavy-quark loop. The much smaller triple Higgs production rate makes the determination of λ_4 prohibitive at the LHC. The total NNLO cross section production at a 100 TeV center of mass energy pp interactions is:

$$\sigma_{NNLO} = 5.56^{+5\%}_{-6\%} \pm 20\% fb$$

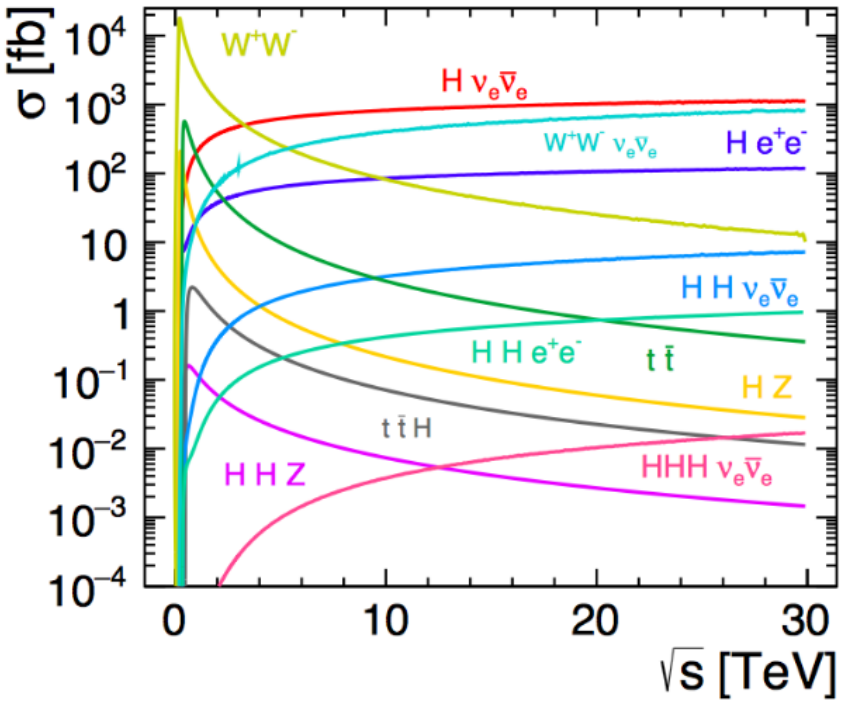

Figure 6: Cross section as a function of centre-of-mass energy for the main Higgs boson production processes at an electron-positron collider [13].

the first uncertainty is an estimate for higher order effects from scale variations, while the last one is an estimate for the missing finite top mass effects.

At lepton colliders, depending on the center of mass energy, the double Higgs can be produced via Higgs-strahlung $l^+l^- \to ZHH$, particularly relevant at low energies, or via vector boson fusion $l^+l^- \to HH\nu_l\bar{\nu_l}$. The Feynman diagrams contributing most to double Higgs production can be seen in Figure 9. Only diagrams with the red circle contains the triple higgs coupling.

The triple Higgs production is dominated by processes shown in Figure 10 and the corresponding cross section can be seen in black in Figure 11. In a muon collider, as shown in Figure 10, the triple Higgs production process involves several diagrams that are not sensitive to the quadrilinear coupling, but contain the trilinear coupling.

2.2.3 Higgs measurements at Future Colliders

The reaches of future collider on the Higgs couplings are evaluated following the same procedure used for LHC and HL-LHC (see section 2.1.2). In this case the BR_{inv} and BR_{unr} shown in equation 2.22 are set to zero. The results on the sensitivity on coupling modifiers that can be reached by the considered Future Colliders are reported in Table 4.

The muon collider numbers are in progress. The only precision on coupling was performed very recently in [17], where the results obtained on the uncertainty of coupling of the Higgs boson with the b quark $\frac{\Delta g_{Hbb}}{g_{Hbb}}$ are compared with the CLIC estimation in [18], and are reported in Table 5. The statistical uncertainties estimated for CLIC take the three energy stage successively into account: each new stage includes all measurements of the previous stages and is represented in Table 5 with a + in the integrated luminosity.

Deviations from the trilinear and quadrilinear Higgs self-coupling from the Standard Model are

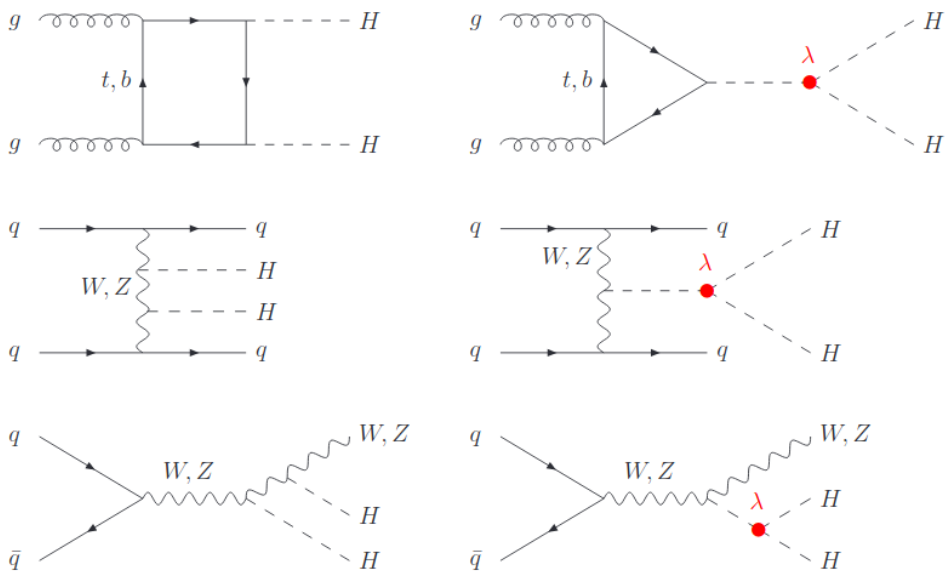

Figure 7: Representative diagrams for double Higgs production at a pp collider. Those containing the triple Higgs vertex are highlighted with red circle [14].

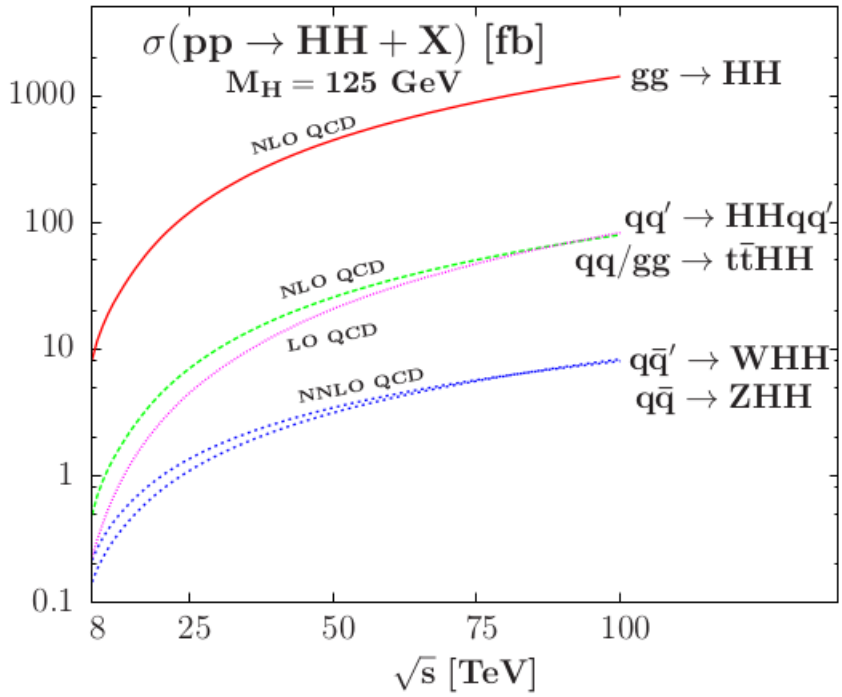

Figure 8: Cross section of double Higgs production at a pp collider as a function of the center of mass energy [15].

usually parametrised by using the Standard Model Effective Field Theory framework (SMEFT) instead of the *kappa* framework. In the SMEFT framework:

$$\lambda_3 = \lambda^{SM}(1+\delta_3) = \kappa_3 \lambda_{SM} \tag{2.23}$$

$$\lambda_4 = \lambda^{SM}(1+\delta_4) = \kappa_4 \lambda_{SM} \tag{2.24}$$

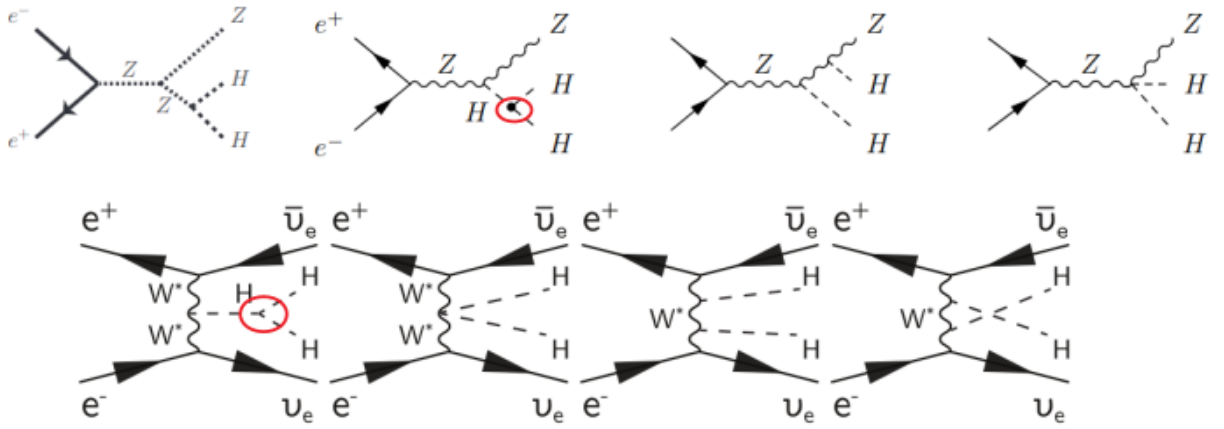

Figure 9: Representative Feynman diagrams of double Higgs production at an electron-positron collider.

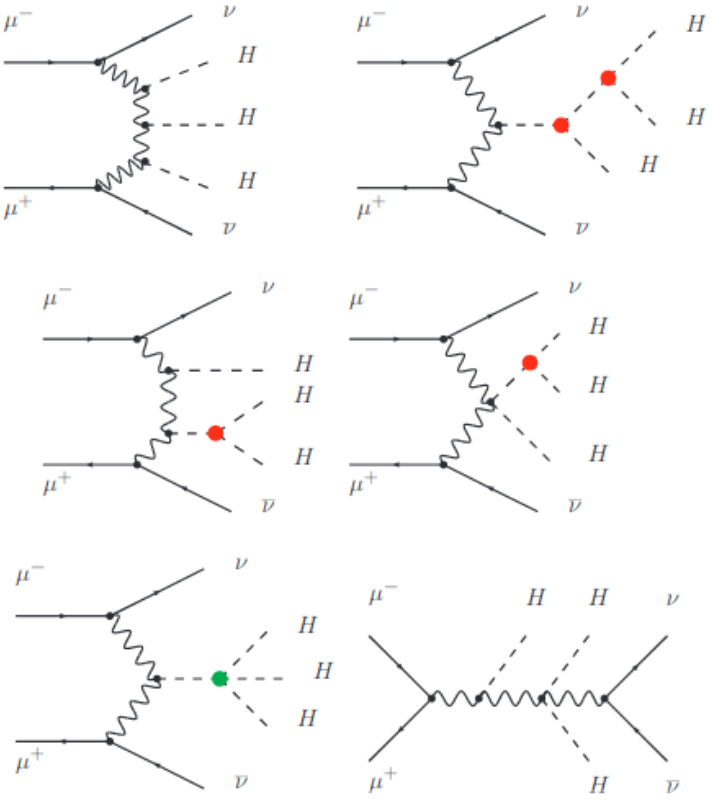

Figure 10: Representative Feynman diagrams contributing to the process $\mu^+\mu^- \to HHH\nu\bar{\nu}$. With red circles are highlighted triple Higgs self-couplings, while the bottom-left diagram is the only sensitive to the quadrilinear Higgs self-coupling [16].

where $\lambda_{SM} = \frac{m_H^2}{2v^2}$ is the trilinear or quadrilinear Higgs self-coupling predicted by the Standard Model (see equation 2.11) and δ_3 and δ_4 contains deviations from the SM. For details about δ_3 and δ_4 expressions within the SMEFT see [3].

The uncertainty expected at the proposed future colliders on the measurement of $\kappa_3 = \frac{\lambda_3}{\lambda_3^{SM}}$ in

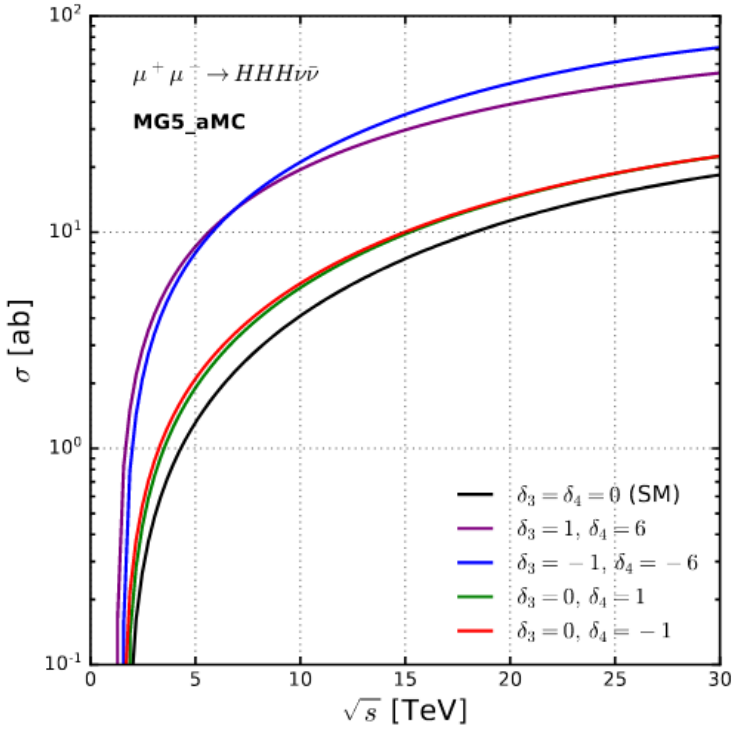

Figure 11: Cross sections of triple Higgs production at a muon collider, for different assumptions on the trilinear and quadrilinear Higgs self-couplings within the SMEFT framework [16].

kappa	HL-LHC	ILC			CLIC			CEPC	FCC-ee/eh/hh
		250	500	1000	380	1500	3000		
κ_W [%]	1.7	1.8	0.29	0.24	0.86	0.16	0.11	1.3	0.14
κ_Z [%]	1.5	0.29	0.23	0.22	0.5	0.26	0.23	0.14	0.12
κ_g [%]	2.3	2.3	0.97	0.66	2.5	1.3	0.9	1.5	0.49
κ_γ [%]	1.9	6.7	3.4	1.9	98⋆	5.0	2.2	3.7	0.29
$\kappa_{Z\gamma}$ [%]	10.	99 ⋆	86⋆	85⋆	120⋆	15	6.9	8.2	0.69
κ_c [%]	-	2.5	1.3	0.9	4.3	1.8	1.4	2.2	0.95
κ_t [%]	3.3	-	6.9	1.6	-	-	2.7	-	1.0
κ_b [%]	3.6	1.8	0.58	0.48	1.9	0.46	0.37	1.2	0.43
κ_μ [%]	4.6	15	9.4	6.2	320⋆	13	5.8	8.9	0.41
κ_τ [%]	1.9	1.9	0.7	0.57	3.0	1.3	0.88	1.3	0.44

Table 4: Expected relative precision (%) of the κ parameters for HL-LHC and Future Colliders. For more details about the entries with $\star$ and $-$, see [3].

combination with the expectation from HL−LHC is summarized in Table 6.

The most optimistic estimate of the sensitivity on the quadrilinear Higgs self-coupling is at FCC-hh [19], under the assumption that $\lambda_3 = \lambda_3^{SM}$:

$$\frac{\lambda_4}{\lambda_4^{SM}} \in [-2, +13]$$

at 2σ with 20 ab^{-1}. It is obtained by studying HHH production with $6b$ in the final state.

	$\sqrt{s}[TeV]$	$\mathcal{L}[ab^{-1}]$	$\frac{\Delta g_{Hbb}}{g_{Hbb}}(\%)$
Muon Collider	1.5	0.5	1.9
	3.0	1.3	1.0
	10	8.0	0.91
CLIC	0.35	0.5	3.0
	1.4	+1.5	1.0
	3.0	+2.0	0.9

Table 5: Precision on Higgs boson coupling to b quark at muon collider [17] and at CLIC [18].

collider	sensitivity on λ_3
HL-LHC	$\sim 50\%$
ILC_{500}	27 %
ILC_{1000}	10 %
$CLIC_{1500}$	36 %
$CLIC_{3000}$	~ 10 %
FCC-ee/eh/hh	5 %

Table 6: Sensitivity at 68% probability on the Higgs cubic self-coupling at HL-LHC and Future Colliders [3].

The first analysis of the muon collider potential on the quartic Higgs self-coupling precision has been performed in [16]. In Figure 12 is presented the expected cross section and the number of $\mu^+\mu^- \to HHH\nu\bar{\nu}$ events for a luminosity of 100 ab^{-1} as a function of the center of mass energy. As can be seen a muon collider at several TeV of center of mass energy and with an integrated luminosity of several tens of attobarns could provide enough events to allow a determination (a SM) quartic Higgs self-coupling with an accuracy in the tens of percent [16].

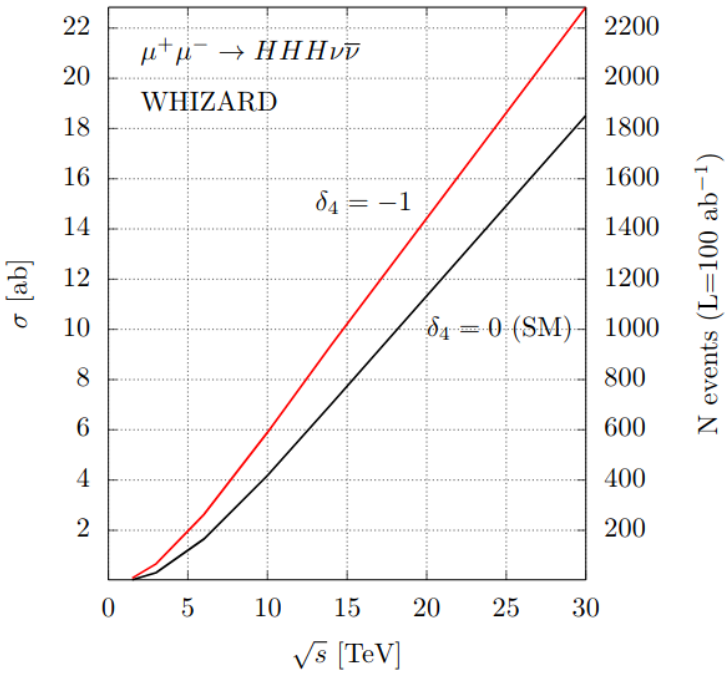

Figure 12: Expected cross section (left) and signal event number (right) for triple higgs production in a muon collider as a function of center of mass energy. [16]

As shown in section 2.2.2 the total cross section of triple Higgs production depend on λ_3. Assuming $\lambda_3 = \lambda_3^{SM}$ for a 14 TeV muon collider and integrated luminosity of $33ab^{-1}$, λ_4 can be constrained with an uncertainty of 50% at 1σ [16].

2.3 Muon collider potential

The potential reaches at a multi-TeV muon collider have been studied in [20]. Some results of the study are reported in this section. The physics reaches of a pp collider have been compared to those obtained in a $\mu^+\mu^-$ collisions for two categories of processes:

- the single particle final state;
- the two particles final state.

Given a muon collisions cross section $[\hat{\sigma_\mu}]$ for a on threshold process $\mu^+\mu^- \to Y$ ($\sqrt{s_\mu} = M_Y$), the equivalent proton energy collider is defined as the corresponding pp collisions energy $\sqrt{s_p}$ such that the process $pp \to Y$ has $\sigma_p = [\hat{\sigma_\mu}]$. However protons are not elementary particles then the equivalent total cross section σ_p is evaluated in terms of the partons level cross section $\hat{\sigma_p}$, since the colliding particles in $pp \to Y$ process are quarks or gluons.

In 13 the equivalent pp collider energy for the single particle final state Y with mass $M = \sqrt{s_\mu}$ is shown as a function of the $\mu\mu$ collider energy. Red (blue) lines represent the case in which gluons (quarks) collide. The comparison is done for different assumptions on the couplings involved in the Y production. By labelling colliding partons as (ij):

- for $[\hat{\sigma}_\mu] = [\hat{\sigma}_p]$ (solid line) both $ij \to Y$ and $\mu^+\mu^- \to Y$ processes are governed by the same physics;
- for $[\hat{\sigma}_p]$ =10$[\hat{\sigma}_\mu]$ (dashed line) the former is governed by QCD and $\mu^+\mu^- \to Y$ by QED;
- for $[\hat{\sigma}_p]$ =100$[\hat{\sigma}_\mu]$ (pointed line) the former is governed by QCD and the latter by electroweak coupling.

As can be seen, a larger pp collider energy is necessary to achieve the same cross section as a $\mu\mu$ collider. This follows from the fact that muons are elementary particles, then all the beam energy $\sqrt{s_\mu}$ is available for the hard collisions. At a proton collider the relevant interactions occur between the proton constituents, which carry a small fraction of the beam $\sqrt{s_p}$ energy. The same study has been done for pair production of heavy particles with $2M^2 = \sqrt{s_\mu}$. Figure 14 shows the equivalent proton collider energy as a function of the muon collider energy. In this Figure 14 are also shown the scaling in energy of the two colliders for the pair production of supersimmetric particles, stops (dot) and chargino (diamond) pair production. Also in this case a much higher center of mass energy pp collider exhibits the same reach of a $\mu^+\mu^-$ collider.

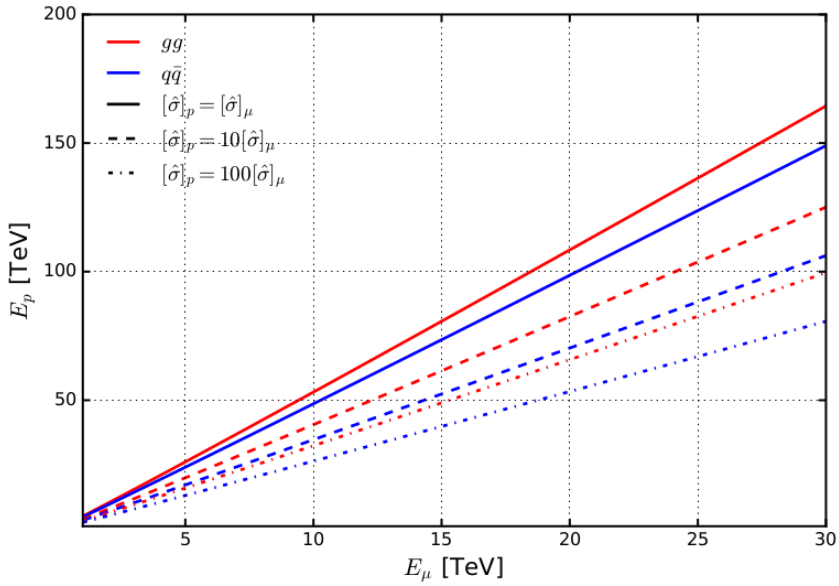

Figure 13: The equivalent proton collider energy E_p [TeV] required to reach the same cross section as a $\mu^+\mu^-$ collider with energy E_μ [TeV] for the annihilation of initial-state particles into a single-particle final state.

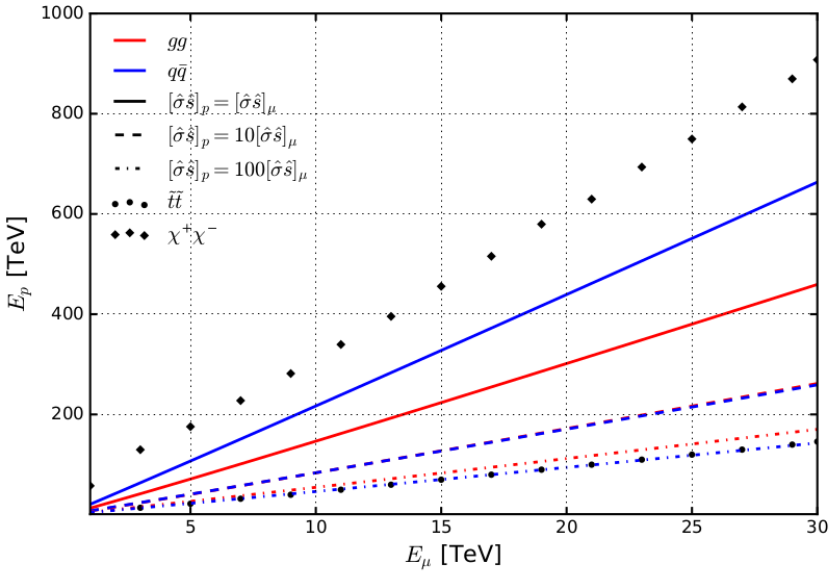

Figure 14: The equivalent proton collider energy E_p [TeV] required to reach the same cross section as a $\mu^+\mu^-$ collider with energy E_μ [TeV] for pair production process.

3 Studies on Muon Collider machine and detector

3.1 Muon Accelerator Complex

The idea of a muon collider has been discussed since 1960 [21] and its design was developed over the years, up to the creation of the Muon Accelerator Program (MAP) in the US, which has conducted its activities for seven years, between 2011 and 2018.

A muon collider accelerator presents several technical challenges [22]. In order to reach high luminosities, it is necessary to produce high collimated and compact beams. Difficulties in obtaining such beams arise from the fact that muons are produced with high energy spread. Furthermore, since muons have a short lifetime they have to be produced and accelerated before a significant loss has occurred.

Accelerating muons to relativistic velocities will increase their lifetime in the laboratory frame to:

$$\tau_{lab} = \tau \cdot \gamma$$

where $\gamma = \frac{E}{m_\mu}$, E is the energy and m_μ is the mass of muons. However even at high center of mass energies, the rate of muon decays along the beam pipe is not negligible, and their decay products give origin to high beam-induced background level [23].

3.1.1 Luminosity

In a collider where two bunches collide with frequency f, the instantaneous luminosity can be expressed by the equation [24]:

$$\mathcal{L} = \frac{f n_1 n_2}{4\sigma_x \sigma_y} \tag{3.1}$$

where n_1 and n_2 are the number of particles in each bunch and, under the assumption that beam have Gaussian profiles, σ_x, σ_y characterize the width in the horizontal and vertical directions with respect to the beam direction. They can be expressed as:

$$\begin{aligned} \sigma_x &= \sqrt{\beta_x^* \epsilon_x} \\ \sigma_y &= \sqrt{\beta_y^* \epsilon_y} \end{aligned} \tag{3.2}$$

β^* is the β function at the collision point (IP). It depends on the magnet lattice and is related to the beam size at the IP, while ϵ_x and ϵ_y are, respectively the emittance in the horizontal and vertical directions (transverse emittances). In beam dynamics each particle at any point along a beam transport line is represented by a point in the six-dimensional phase space [25]. The emittance is a measure for the average spread of particle coordinates in position and momentum phase space in a beam. In a low-emittance beam particles are confined to a small phase space area and have nearly the same momentum. The description of a beam of particles in the transverse phase space can be done with coordinates x, x', y, y', where $x' = \frac{dx}{ds}$ and $y' = \frac{dy}{ds}$. s is the coordinate of the nominal beam trajectory [25]. In an x, x' (or y, y') plane, the beam has a elliptical shape with area $A = \epsilon_x \pi$. The ellipse area is conserved when the beam is focused or defocused, and thus also the transverse emittance is conserved. This is a consequence of the Liouville Theorem that states that under the influence of conservative forces the density of the particles in phase space stays constant.

In order to achieve high luminosity, all these parameters have to be appropriately tuned, and the main challenge in a muon collider, is to find a system to produce low emittance muon beams, as will be shown in section 3.1.2.

3.1.2 Muon production

Production of muon beams can be obtained in two ways:

- proton beam impinging on a thick target. Muons are produced as decay products of $\pi^{\pm} \rightarrow \mu^{\pm} + \overset{(-)}{\nu}$ generated in the spallation process.
- positron beam on target: $e^+e^- \rightarrow \mu^+\mu^-$.

The first method was adopted by the MAP collaboration and will be explained in detail in the next section 3.1.3.

The second method is exploited by the Low EMittance Muon Accelerator (LEMMA scheme) [26]. In the LEMMA scheme shown in the lower part of Figure 15 muon pairs are produced by sending 45 GeV positrons bunches into a target where they collide with material electrons. The annihilation of positrons with the electrons take place close to the threshold energy for $\mu^+\mu^-$ pair production $\sqrt{s} \sim 0.212$ GeV in the center of mass frame. This allow to produce high collimated and low emittance muon beams. The main limitations of this scheme are due to the low cross section for muon production $\sigma(e^+e^- \rightarrow \mu^+\mu^-) \sim 1$ μb for $\sqrt{s} = 0.230$ GeV. In order to produce enough muons the intensity of the positron beam source is required to be very high, and this would induce a high stress on the target system. Studies on this scheme are still underway, therefore analysis and results presented in the next chapters are based on the MAP configuration.

3.1.3 Muon collider scheme

The MAP collaboration developed innovative concepts and tested new technologies for muon production and acceleration [27]. The full facility is divided in different sections as shown in the upper part of Figure 15:

- **Proton Driver**: The high-power proton beam for pion production will be provided by a chain of high power accelerators developed by Project X [28]. A 3 GeV proton beam with will be accumulated and re-bunched in a ring for further acceleration to 8 GeV in a pulsed linac. The current design assumes $\sim$ 2 ns bunches of intense protons ($2 \cdot 10^{14}$) at a 15 Hz repetition rate. Pions are produced by the interaction of the proton beam with a high Z material, such as liquid-metal mercury jet, which has been tested at CERN in the MERIT experiment [29]. The cross sections involved in this process are of the order of $\sigma \sim mb$. The pions are confined transversely by strong longitudinal magnetic field (20 T at the target) lowering to 1.5-2 T in the decay channel.

- **Front End**: pions decay into muons and neutrinos, producing a beam of muons with high emittance. These muons have a momentum of about 100-200 MeV/c. The decay channel is followed by a buncher section, which consists on a system of RF cavities (with frequency in the range 200-360 MHz) to form the muon beam into a train of bunches of both signs and by a phase rotator section in which the leading high-energy bunches are decelerated and the late low-energy bunches are accelerated. At this level the normalised r.m.s. emittance of muons captured in a bunch is $\sim$2 cm in all planes.

- **Cooling**: ionization cooling is needed to reduce the emittance in the 6D phase space by at least six orders of magnitude. The reduction of the beam emittance in the 4D phase space (referred as a reduction of transverse emittance) can be achieved by passing a magnetically focused beam through a material (the absorber). As illustrated in Figure 16, beam particles with initial momentum p_{in} loose momentum in three directions (Δp_{abs}) while a system of radio-frequency cavities (RF) restore momentum only along the beam direction Δp_{RF} [30].

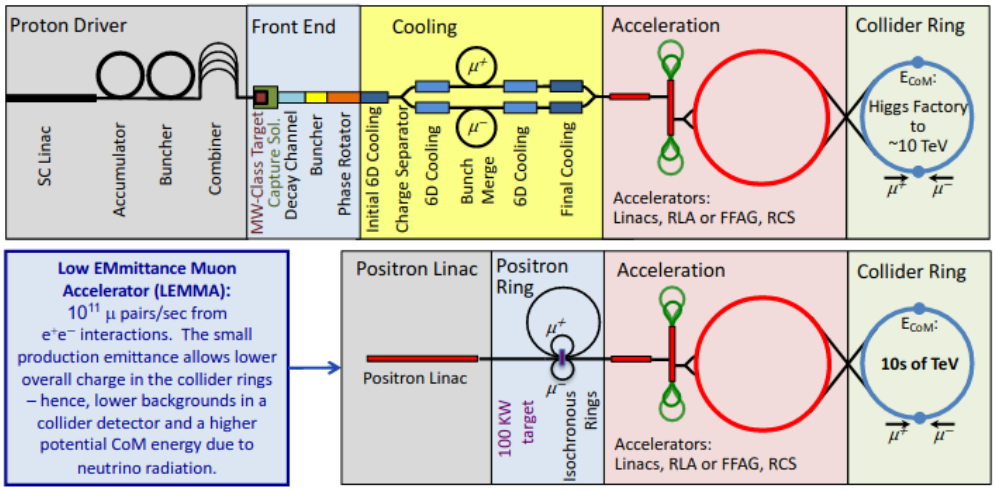

Figure 15: Schematic layouts of the muon collider proton driver scheme explored by MAP (top) and the low emittance positron driver scheme (bottom) [22].

In this way a reduction of the beam size and the particles momentum spread in the transverse plane with respect to the axis of motion of the beam is achieved. The first experimental demonstration of the ionization cooling in 4D has been published by MICE [31].

The next important step towards a muon collider would be to design and build a cooling module combining the magnets and absorbers, and to achieve full 6D cooling. The additional step consists on a bending magnet to separate particles with different momentum and, by properly designing the absorber geometry, to have greater energy loss at higher momenta [32]. The cartoon in Figure 17 shows a simple idea of how this can be done: particle beam pass through a wedge absorber with variable thickness [33]. The result will be a beam with a higher position spread in the transverse plane but with lower momentum dispersion in the longitudinal direction. This method is called emittance exchange because longitudinal emittance is reduced at the expense of increasing transverse emittance. Combined emittance exchange with transverse cooling would allow to achieve 6D cooling, which is assumed by MAP simulation of the machine. After an initial ionization cooling, muons of opposite charge are separated. Then the longitudinal emittance is reduced until it becomes possible to merge the trains into single bunches, one of each sign. Further cooling in all dimensions is applied to the single bunches in the following 6D cooling lattices.

- **Acceleration**: the beam is accelerated by a series of fast acceleration stages to take the muon beams to the relevant energy before injection in the muon collider Ring, where the final collisions occur. For this section a final design is not available yet and some proposed approaches are under study: Recirculating Linacs Accelerators (RLA) [34] or Fixed Field Alternating Gradient (FFAG) [35] and Rapid Cycling Synchrotron(RCS)[36].

- **Collider Ring**: the beams are injected in the collider ring for the collision. The number of muons in the beams decreases over time due to the random decays of muons. High magnetic field ($\sim$ 10 T) in bending magnets is needed to minimise the ring circumference and thus maximise the average number of muons that reach the interaction point. The collider ring has been designed for center of mass energies $\sqrt{s} = 125$ GeV [37], $\sqrt{s} = 1.5$ TeV [38], 3 TeV [39] and 6 TeV [40].

The MAP collaboration developed a start-to-end design for a 1.5 TeV center of mass energy muon

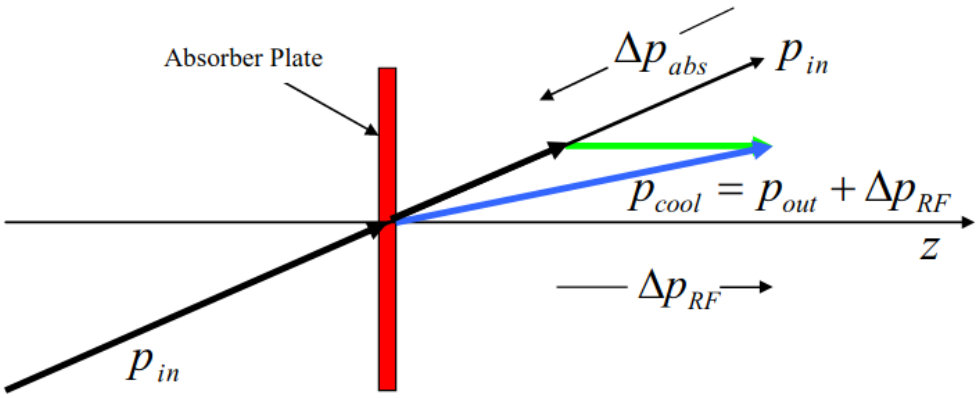

Figure 16: Conceptual picture of ionization cooling. Particles with initial momentum p_{in} loose momentum in all direction via ionization by passing through an absorber. In a RF cavity the longitudinal momentum only is restored. Taken from [30]

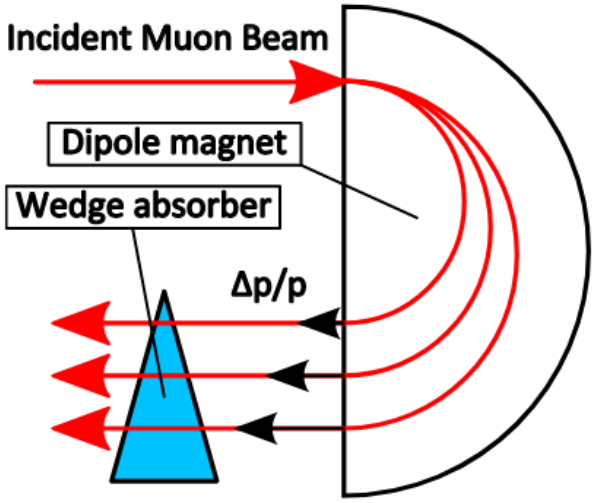

Figure 17: Principle of emittance exchange [33]. The incident muon beam is passed through a dipole magnet to create position spread and a wedge absorber designed to have greater energy loss at higher momenta, in order to reduce momentum dispersion.

collider. The basic parameters of the muon beams in a 1.5 TeV muon collider are given in Table 7. In the Table the normalized emittance is reported. When a beam accelerates, the transverse beam size shrinks [41]. The idea of invariant emittance can still be used if the emittance is scaled according to the beam energy. For this reason the values of the beam emittances are usually normalized by the relativistic factor:

$$\epsilon^* = \beta\gamma\epsilon$$

in which β and γ are the relativistic functions.

3.2 The interaction region and machine-detector interface

The MAP collaboration developed the detailed design of the interaction region (IR) and of the machine detector for $\sqrt{s}$=1.5 TeV and $\sqrt{s}$=125 GeV that can be found in [23] and [42].

The model of the IR for 1.5 TeV center of mass energy is shown in Figure 18. The 125 GeV is

Parameter	Unit	Value
Luminosity	$10^{34} cm^{-2} s^{-1}$	1.25
Repetition Rate	Hz	15
β^*	cm	1
Normalized Emittance $\epsilon_\perp$	$\pi \cdot \mu m \cdot rad$	25
Number of muons / bunch	10^{12}	2

Table 7: Basic parameters for a muon collider at $\sqrt{s} = 1.5$ TeV, taken from [11]

not considered in this study. In green is represented the outside of the accelerator. The two arcs of the collider ring tunnel converge to the interaction point, where the detector is located. The vacuum vessel inside the tunnel, is composed by Nb_3Sn superconducting dipole magnets. In light blue are parts not filled with material.

Figure 19 is a zoom on the detector and the final triplet region of superconducting magnets with shell-type Nb_3Sn coil [38]. Different colors represent different materials: the red parts are iron/steel elements, while grey parts are composite blocks. The final focus of muon beams is provided by quadrupole doublets formed by five quadrupole magnets Q1-Q5 (the first quadrupole Q1 is not clearly visible in Figure 19 as it is hide by the yellow tungsten nozzle, whose function is fundamental for the background reduction, as it will be explained in section 5). The first two quadrupoles provide the beam final focus for the bunch crossing while the following three are defocusing ones. The nominal field in the quadrupoles magnet coils is around 11 T.

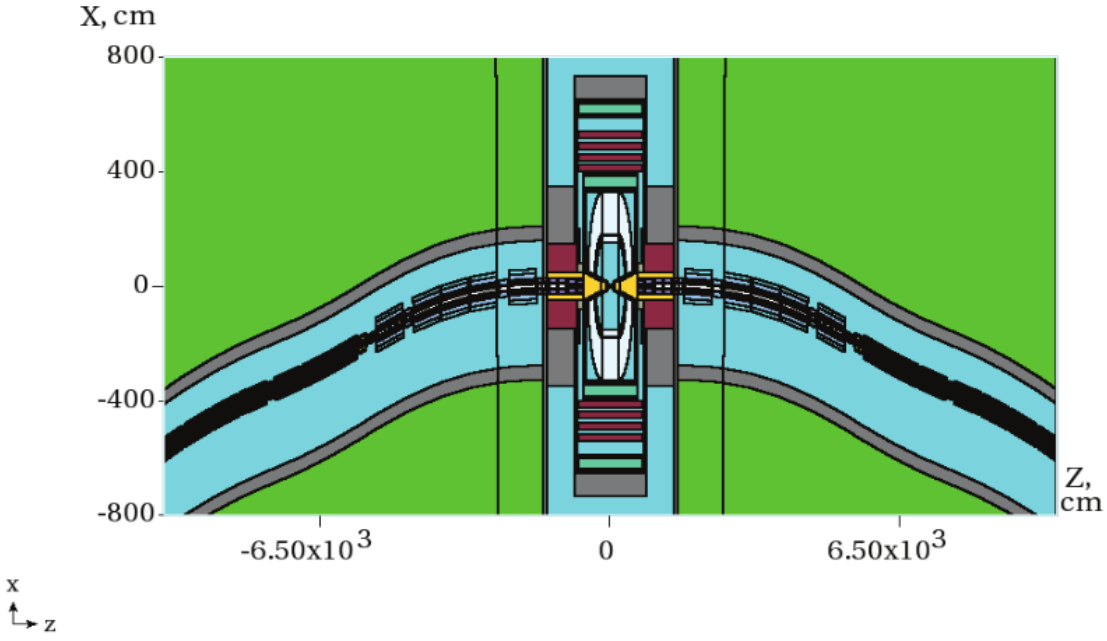

Figure 18: Plan view of MARS25 model for IR at | z |<10000 cm with the muon collider detector in the central part with the tungsten components in yellow, empty spaces in light blue, iron components in red and concrete supports in grey. At both sided the final sections of the collider ring arcs with the scheme of the magnet lattice. Vertical black lines indicate the position at $z = \pm 25$ m that will be used for the beam-induced background simulation in section 3.4. Picture taken from [23].

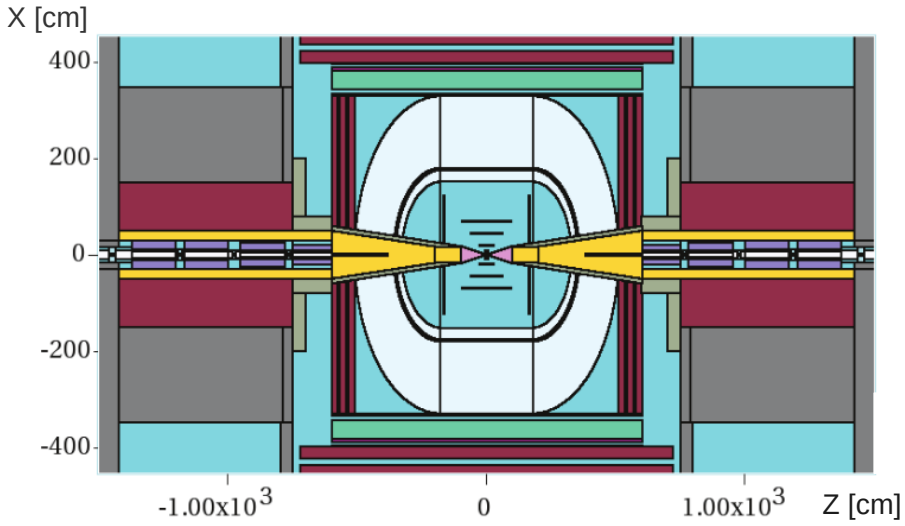

Figure 19: Details of MDI at | x |<500 cm and | z | <1500 cm. The detector model is located in the central part, with the tungsten components in yellow, empty spaces in light blue, iron components in red and concrete supports in grey. The models of four out of the five quadrupole magnets are visible around the beam pipe, surrounded by iron and concrete. The closest magnet to the interaction point is not visible in the picture as it is hidden by the nozzles [23].

3.3 Beam-induced background studies

The decay length of 0.75 TeV muon is $\lambda_D = 4.7 \cdot 10^6 m$. With $2 \cdot 10^{12}$ muons in a bunch, one has $4.28 \cdot 10^5$ decays per meter of lattice in a single pass. This results in $1.28 \cdot 10^{10}$ decays per meter per second for two 0.75 TeV muon beams [23].

Muons decay inside the beam pipe produce energetic decay electrons, which emit synchrotron photons in the presence of the high magnetic field of the ring magnets, and neutrinos. Electrons and synchrotron photons hitting the beam pipe produce electromagnetic showers in the collider and detector components, hadrons via photo-nuclear interactions and muons via Bethe-Heitler process. In turn these particles interact with the lattice, detector and experimental hall components and produce other electromagnetic showers and hadronic cascades via deep inelastic nuclear interaction processes.

The results of all these interactions is a high flux of particles, which deposits energy on the surrounding machine components and eventually reach the interaction point and the detector, if the muon decay takes place in proximity of the machine-detector interface. Without any protection systems the flux of beam-induced background particles in the detector and in the storage ring found to be 0.5-1 kW/m, while a good practice number should be few W/m [23].

The high energy deposition damage the superconducting (SC) magnets and may result in magnet quench and in high heat load to the cryogenic system which also requires special protection measures.

This high level of background has several effects on the detector performance and consequently on physics measurements: detector component can be damaged, the reconstruction of objects not related to the products of muons collisions becomes difficult and the detector resolution worsen.

Several studies were performed since 90s [43] [44] in order to characterize the beam-induced background properties and propose mitigation strategies. Energy deposition and detector back-

grounds are simulated with MARS15 code. All related details of geometry, materials distribution and magnetic field lattice elements and tunnel in the ±200 m region from IP, detector components and machine detector components are implemented in the model. These simulations [43] demonstrated the effectiveness of the two yellow cone shaped shields, in the reduction of the high flux of particles which reach the IR and the detector. The optimization of these shields was done by testing cones of different material, inner radius, starting distance from the interaction point and aperture angle and by looking at the surviving particles distribution in the external surface of the nozzle.

The best design of nozzle for the background reduction at 1.5 TeV is represented in Figure 20 and can provide the reduction of muon beam background by more than three orders of magnitude. Each nozzle shielding starts at 6 cm from the intraction point and the entire length is 6 m. The angle in the region closest to the IP (between 6 to 100 cm) is 10° with respect to the beam pipe, while in the 100 to 600 cm region the angle is reduced at 5°, in order to minimize the impact on the detector performance, in particular the detector angular acceptance. The nozzles are built in tungsten which is a high-Z material and, assisted by the detector solenoid field, which will be described in section 4, is particularly effective in reducing the electromagnetic component of the background. In the region between 100 and 600 cm the tungsten is also encapsulated in a borated polyethylene shell to reduce the flux of low-energy neutrons.

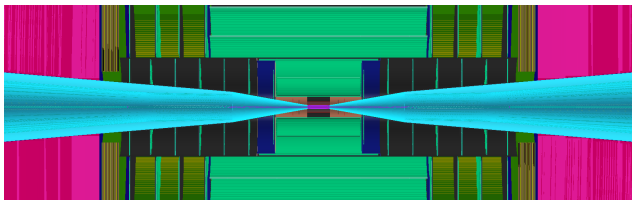

Figure 20: Detector design of nozzle, coloured in cyan, for background reduction at center of mass energy $\sqrt{s} = 1.5$ TeV.

In order to reduce the energy deposited on the machine components, an appropriate design for the magnets in the final focus region and a protection system for the superconducting magnets which consists on tungsten masks was also found and improved over the years [45].

3.4 Beam-induced background characteristics

In a 1.5 TeV center of mass energy muon collider, the beam-induced background particles are mostly produced by muons decaying in a range of ±25 meters around the IP. It has been verified by MAP collaboration [23] that outside that range, the background contribution become negligible for all components except for Bethe Heitler muons, whose range of interest is $\pm 100m$ from IP. The beam-induced background is computationally high demanding. Then with only a fraction of the μ^+ μ^- decays on the 26 m beam length is generated, that is successively reweighted to get the total number of background particles per bunch crossing (BX).

The number of background particles entering the detector through the MDI surfaces as a function of the distance from IP to muon decay point along the beam can be seen in Figure 21. Bethe Heitler muons are not the full sample, because only a fraction was available for the simulation.

The most abundant particle type entering the detector through the MDI surface consists of photons and neutrons, followed by electrons and positrons, charged hadrons and muons. The relative fractions are reported in Table 8. In parentheses are shown the thresholds on the minimum kinetic energy used in the MARS15 simulation, particles with lower energy do not arrive on the detector.

In Figure 22 is shown the momentum spectra. The electromagnetic component presents relatively soft average momenta ($\langle p_{ph.} \rangle = 1.7$ MeV and $\langle p_{el.} \rangle = 6.4$ MeV), which increases for charged

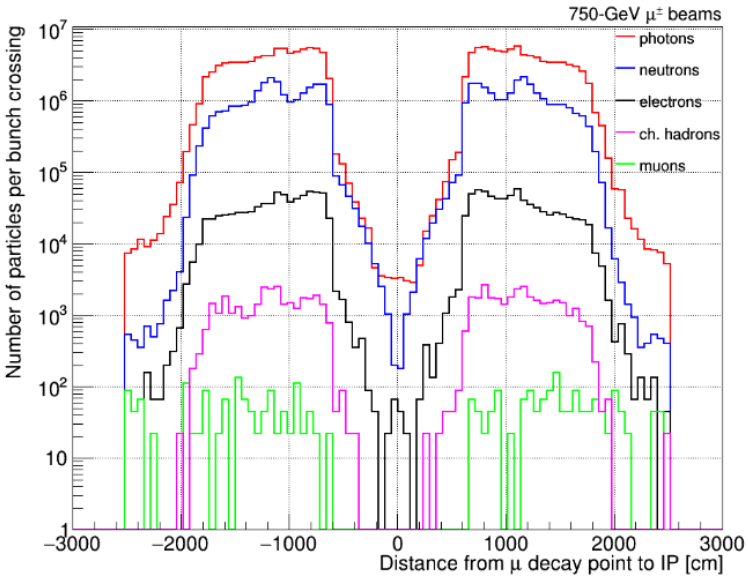

Figure 21: Number of background particles as a function of distance from IP to muon decay point along the beam [43]

Particles (Energy threshold)	Fraction
photons ($E^{kin}_{ph} > 0.2$ MeV)	94 %
neutrons ($E^{kin}_{n} > 0.1$ MeV)	4 %
electrons ($e^{\pm}$) ($E^{kin}_{e} > 0.2$ MeV)	1 %
other particles: charged hadrons ($E^{kin}_{chhad} > 1$ MeV) muons ($E^{kin}_{\mu} > 1$ MeV)	< 1 %

Table 8: Fraction of particles which compose the beam-induced background

and neutral hadrons ($\langle p_n \rangle = 477$ MeV and $\langle p_{ch.hadr.} \rangle = 481$ MeV). Muons are the component with the highest values for the momenta.

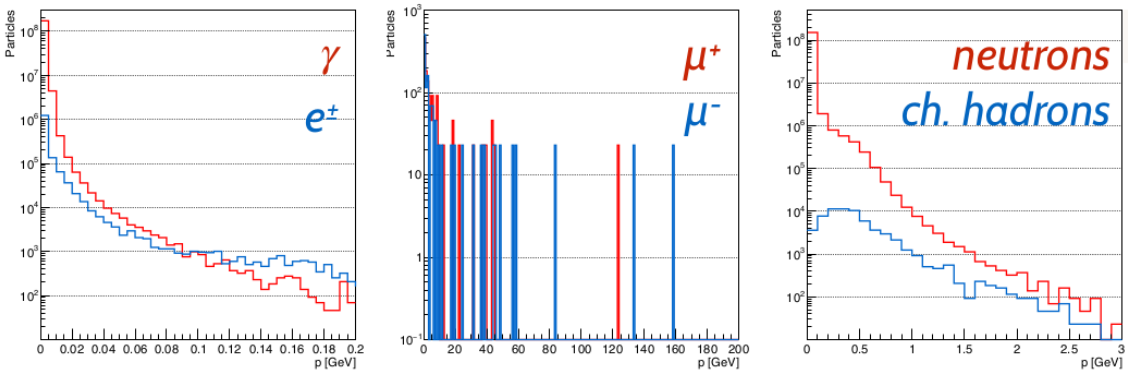

Figure 22: Momentum distribution of beam-induced background particles [46].

It is important to stress that the optimization of the nozzle design and the magnet shielding have to be done for each center of mass energy center of mass energy and the beam-induced background

has to be studied consequently because:

- At different center of mass energies the expected muons decay rate will be different because the muon decay length will change and products of muon decays reach the interaction region from distances which depend on the center of mass energy. The studies of a 125 GeV center of mass energy muon collider, shows that the background level expected is higher with respect to the 1.5 TeV case [42], since the expected number of muon decays per meter of the lattice is 10^7 in a single pass.

- As it was explained in this chapter, the design of the machine-detector interface depends on the amount of beam-induced background and have to be optimized to reduce it. On the other hand the background composition on the detector depends on the design of the machine-detector interface. To give an example, in the 125GeV machine (see [45]), the last triplet magnets configuration is different, then the material distribution will be different.

3.5 Further mitigation strategies

Despite the mitigation effect provided by the shielding nozzles, a large particle flux reaches the detector, causing a very high occupancy in the first layers of the tracking system that impact the detector performance. A further reduction of the beam-induced background is possible by investigating the time of arrival of particles at the detector with respect to the bunch crossing time. The time of flight of background particles surface has a significant spread with respect to the bunch crossing, as can be seen in Figure 23 for different backgorund components. The peak at $t = 0$ s is due to:

- particles generated by muon beam decays next to the interaction region that arrives at the external surface almost on time with the bunch crossing

- particles generated by muon beam decays that interact with the nozzle surface and are re-emitted at times close to the time of bunch crossing

The long tails for photons, electrons and positrons and neutrons are due to their bouncing and multiple interactions in the MDI components or that have been produced at large distances from IP.

This timing distribution will be compared to the one of particles coming from the interaction point and, as will be shown in section 5, a proper choice of the acquisition time window will allow to reduce the amount of beam-induced background during the data taking.

Other characteristics of the beam-induced background particles can be exploited to reduce the amount of particles that reaches the detector. As shown in Figure 22 beam-induced background particles have low momentum, then on average they will released higher fraction of their energy when passing through the material with respect to particles coming from the $\mu^+\mu^-$ collisions. Then, a cut on the energy released in the detector components can be applied to reject low-momentum beam-induced background particles. Furthermore, the usage of double-layers silicon detector in the tracking system can be useful to reject low-momentum particles, that with high probability release energy in only one of the two layers.

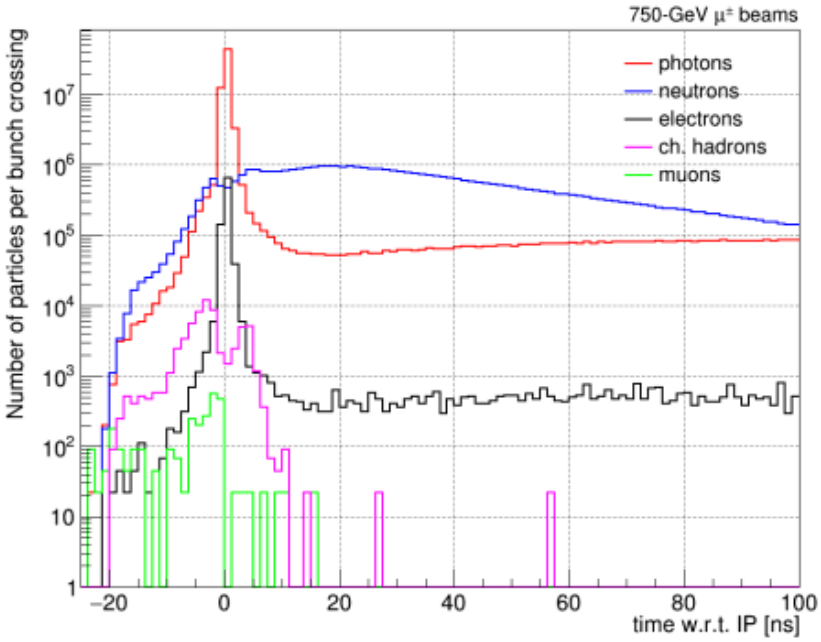

Figure 23: Time of arrival distribution of beam-induced background particles at the detector surface

4 Detector Description

The analysis described in this thesis have been performed by using the full detector simulation with the ILCSoftware package, described more in detail in the Section 5. The original design of the detector has been provided by the CLIC collaboration in the version that can be found in [47]. Several detector components were changed, according to the MAP studies on the muon collider detector [48]: main modifications involves the insertion of the tungsten nozzles, the design of the vertex and tracker detectors and the removal of the two small electromagnetic calorimeters LumiCal and BeamCal, installed in the very forward region.

4.1 Overview of the detector

The detector has a cilindrical shape and it has a $11,4$ m long and has a diameter of $12,8$ m. By going from the inside to the outside it is composed by:

- A vertex and a tracker detector
- An electromagnetic calorimeter
- An hadronic calorimeter
- A superconducting solenoid which provide a magnetic field of 4 T
- An iron joke instrumented with a resistive plate chamber for the muons detection

The origin of the space coordinates is the beam interaction point. The z-axis has direction parallel to the beam pipe, the y-axis is parallel to gravity acceleration and the x-axis is defined as perpendicular to the y and z axes.

4.2 Vertex detector and tracking system

The transverse momenta of charged particles in collision products are measured by the tracker system, which is composed by a vertex detector, closest to the beam pipe, a inner tracker and an outer tracker detector. The vertex detector and the tracker system are composed by barrels and endcaps. Barrels are cylindrical surface with variable length and radius, whose axis coincides with the beam pipe and cover the central part of the detector. The endcaps are annulus centered on the z axis, with variable distance from the interaction point and radius which cover the forward part of the detector.

4.2.1 Vertex detector

The vertex detector (VTX) needs to be close to the interaction point in order to identify seconday vertices, which can be a signature of b and c hadrons decay.

The building blocks of the barrel detection layers are rectangular staves of sensors, arranged to form a cilinder (see left Figure 24), while the endcaps are constituted by trapezoidal modules of sensor, arranged as "petal" to form the disk. They are all composed by double-sensor layers, two sensitive layers fixed on one support structure, in both barrel and forward region, with 2 mm gap. In Figure 24 the full vertex detector is shown: on the left the longitudinal $(y-z)$ view of the vertex detector barrel layers, with the z axis rotated of $\sim 35°$ with respect to the $y-z$ plane. On the right the half section of the longitudinal view of the vertex detector is reported, with $z \in [-17$ cm, 28 cm] and the z axis rotated of few degrees with respect to the $y-z$ plane.

The vertex detector is composed by:

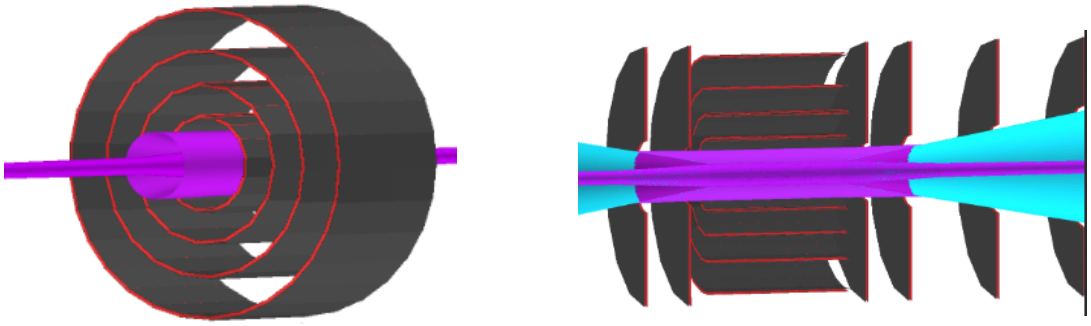

Figure 24: Left: longitudinal view of the vertex detector barrel layers, with the z axis rotated of $\sim 35°$ with respect to the $y-z$ plane. Right: longitudinal section of the vertex detector with $z \in [-17$ cm, 28 cm] and the $zaxis$ rotated of few degrees with respect to the $y-z$ plane.

Barrel	Radius (cm)	N. staves
R_1	3.1	16
R_2	5.1	15
R_3	7.4	21
R_4	10.2	29

Table 9: Vertex barrel layers geometrical characteristics

- four barrel layers with silicon pixel of size 25×25 μm^2, and thickness 50 μm whose radius and geometrical characteristics are summarized in Table 9
- eight endcaps layers, four for each side of the interaction point are composed by silicon pixel of size 25×25 μm^2 and thickness 50 μm and 16 modules. Their positions along the z axis and the geometrical characteristics are reported in Table 10.

Endcap	$\lvert\Delta z\rvert(cm)$	R_{min} (cm)	R_{max} (cm)
$\lvert\Delta z_1\rvert$	8.0	2.5	11.2
$\lvert\Delta z_2\rvert$	12.0	3.1	11.2
$\lvert\Delta z_3\rvert$	20.0	3.8	11.2
$\lvert\Delta z_4\rvert$	28.0	5.3	11.2

Table 10: Vertex endcap disks geometrical characteristics

4.2.2 Tracker System

By going from inside to outside, surrounding the vertex detector, there are the inner tracker barrel and the outer tracker system. The scheme of the full tracker system is shown in Figure 25. They are composed by a single layer of silicon sensors of 100μ m thickness.

The inner tracker is composed by:

- three barrel layers whose radius and geometric characteristics are summarized in Table 11. Strips on the barrels have size 50 μm $\times$ 1 mm and thickness 100 μ m are oriented with the long side parallel to the beam axis.

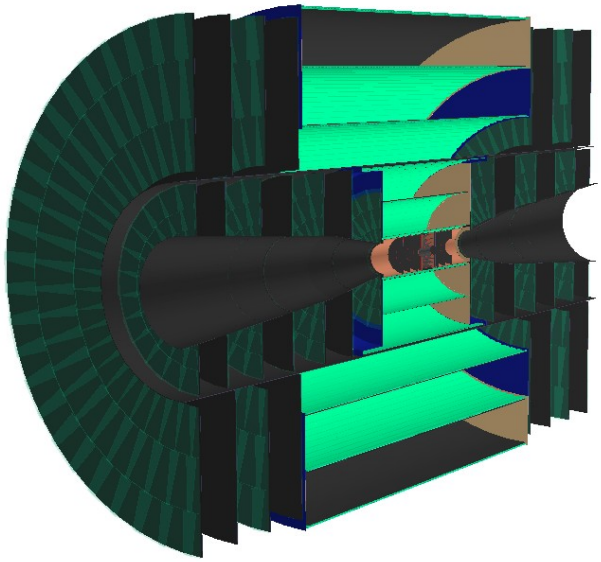

Figure 25: Longitudinal section of the full tracker system, with the z axis rotated of $\sim 35°$ with respect to the $y-z$ plane. The inner tracker is located in the central part, surrounded by the outer tracker layers.

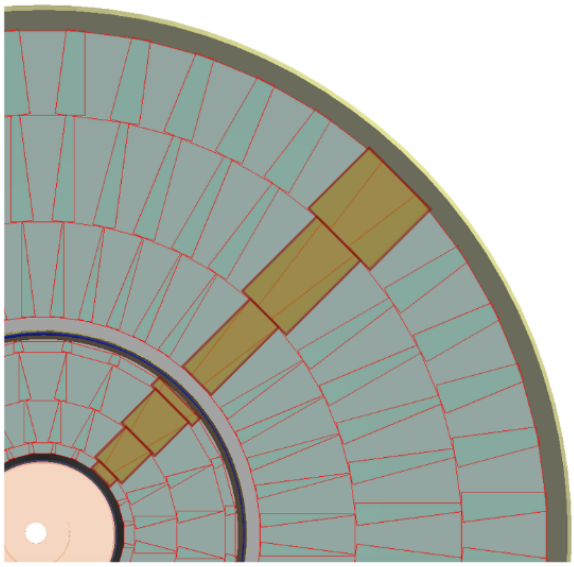

Figure 26: Transverse view of the sixth inner disk and the third outer tracker disk.

Barrel	Radius (cm)	Half length	N. staves
R_1	12.7	48.2	28
R_2	34.0	48.2	76
R_3	55.4	69.2	124

Table 11: Inner tracker barrels layers geometrical characteristics

- fourteen endcaps, seven for each side of the interaction point. Each of them is composed by 26 modules. Their positions along the z direction and characteristics are reported in Table

12. The first endcap is composed by pixel sensors of size 25×25 μm^2, while all other endcaps by strips of size 50 μm $\times$1 mm. Strips are oriented along the radius of the disk. All sensors have thickness 100 μm. The inner tracker and outer tracker endcaps are composed by radial modules composed by rectangular pads. In Figure 26 is presented a transverse view of the sixth inner disk and the third outer tracker disk [49]. Pads are highlighted in brown. The overlay between petals is visible as darker, smaller wedges.

Endcap	$\lvert\Delta z\rvert$ cm	R_{min} cm	R_{max} cm
$\lvert\Delta z_1\rvert$	52.4	9.5	42.7
$\lvert\Delta z_2\rvert$	80.8	14.7	55.8
$\lvert\Delta z_3\rvert$	109.3	19.0	55.6
$\lvert\Delta z_4\rvert$	137.7	21.2	56.1
$\lvert\Delta z_5\rvert$	166.1	23.7	55.7
$\lvert\Delta z_6\rvert$	194.6	26.4	55.4
$\lvert\Delta z_7\rvert$	219.0	28.4	55.8

Table 12: Inner tracker endcap disks geometrical characteristics

In the outermost part is located the Outer Tracker. All the subdetectors are composed by silicon strips of size $50\mu m \times 10mm$. In particular in the Outer tracker there are:

- three barrel layers whose radius and characteristics are reported in Table 13. They are composed by strips of size 50 μm $\times$10 mm and thickness 100 μm. As in the inner tracker, the strips are oriented with the long side parallel to the beam axis.

Barrel	Radius cm	N staves
R_1	81.9	184
R_2	115.3	256
R_3	148.6	328

Table 13: Outer tracker barrels layers geometrical characteristics

- eight endcaps, four for each side of the interaction point. Their positions along the z direction and characteristics are reported in Table 14. They are composed by 48 modules with sensor strips of size 50 μm $\times$10 mm and thickness 50 μm. As in the inner tracker, strips are oriented along the radius of the disk.

Endcap	$\lvert\Delta z\rvert$ cm	R_{min} cm	R_{max} cm
$\lvert\Delta z_1\rvert$	131	61.7	143
$\lvert\Delta z_2\rvert$	161.7	61.7	143
$\lvert\Delta z_3\rvert$	188.3	61.7	143
$\lvert\Delta z_4\rvert$	219	61.7	143

Table 14: Outer tracker endcap disks geometrical characteristics

4.3 Calorimetry

The calorimeter detector is divided in the electromagnetic and the hadronic calorimeter part following the CLIC design. Figure 27 shows both systems: the electromagnetic calorimeter in yellow

and the hadronic calorimeter in purple. In the future a detailed study will be performed to determine the most appropriate technology and design of a calorimeter system for the muon collider.

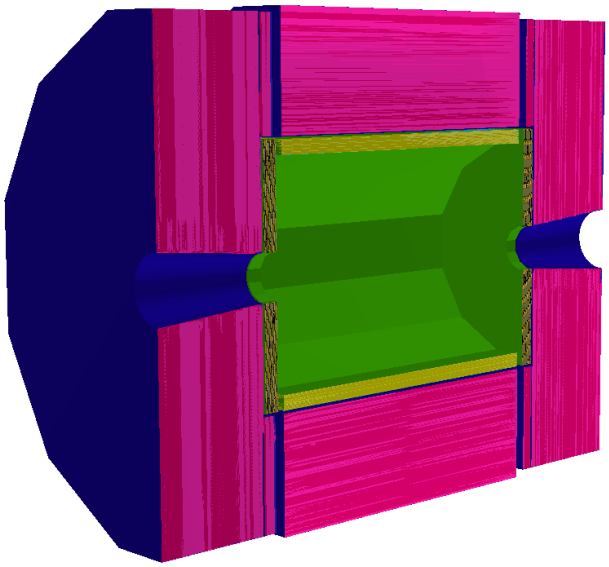

Figure 27: Longitudinal section of the calorimeter system, with the z axis rotated of $\sim 35°$ with respect to the $y-z$ plane: the electromagnetic calorimeter is in yellow, the hadronic calorimeter is in purple.

4.4 Electromagnetic and hadronic calorimeter

The electromagnetic calorimeter (ECAL) consists of a dodecagonal barrel and two endcaps systems, located inside the hadronic calorimeter. It is composed by 40 layer of interlaced layers of Tungsten as absorber material 1.9 mm thick and Si sensor as active material with 5×5 mm^2 silicon detector cells. Tungsten is a dense material with a large ratio of interaction length to radiation length. A small radiation length will promote the start of the electromagnetic shower earlier in the calorimeter, while a large interaction length will reduce the fraction of hadronic showers starting in the ECAL. The choice of thin silicon layers offers an optimal spatial resolution. The total thickness of the ECAL corresponds to about 22 X_0. The overall dimensions of the ECAL as implemented in the simulations are provided in Table 15.

The role of the hadronic calorimeter (HCAL) is to separate neutral hadron showers from other particles and to measure hadron energies. It consists of a dodecagonal barrel and two endcaps systems. The hadronic calorimeter is composed by 60 layers of interlaced layers of steel absorber 19 mm thick and plastic scintillating tiles with cell size 30×30 mm^2. Both, the endcap and the barrel HCAL, are around 7.5 λ_I deep, which brings the combined thickness of ECAL and HCAL to 8.5 λ_I. The overall dimensions of the HCAL are summarized in Table 16.

4.5 Calorimeter system performance

The energy resolution of the calorimeter system has been studied for the CLIC configuration and running conditions. Since the Muon Collider condition will be different, that will have to be studied in detail. Here the CLIC numbers are reported just for reference. The ECAL energy resolution [47] is determined by using single photon events as a function of the true energy of photons ($E(\gamma_{true})$)for three different angular regions of the calorimeter: $|cos\theta|$ <0.65, 0.78 < $|cos\theta|$ <0.83,

ECAL absorber	W
ECAL X_0	22
ECAL barrel r_{min} [cm]	150.0
ECAL barrel r_{max} [cm]	170.2
ECAL barrel δr [cm]	20.2
ECAL barrel z_{max} [cm]	221.0
ECAL endcap z_{min} [cm]	230.7
ECAL endcap z_{max} [cm]	250.9
ECAL endcap δz [cm]	20.2
ECAL endcap r_{min} [cm]	41.0
ECAL endcap r_{max} [cm]	170.0

Table 15: Table ECAL dimensions

HCAL absorber	Fe
HCAL λ_I	7.5
HCAL barrel r_{min} [cm]	174.0
HCAL barrel r_{max} [cm]	333.0
HCAL barrel δr [cm]	159.0
HCAL barrel z_{max} [cm]	221.0
HCAL endcap z_{min} [cm]	253.9
HCAL endcap z_{max} [cm]	412.9
HCAL endcap δz [cm]	159.0
HCAL endcap r_{min} [cm]	25.0
HCAL endcap r_{max} [cm]	324.6
HCAL ring z_{min} [cm]	236.0
HCAL ring z_{max} [cm]	253.9
HCAL ring r_{min} [cm]	173.0
HCAL ring r_{max} [cm]	324.6

Table 16: Table HCAL dimensions

$0.83 < |cos\theta| < 0.94$ to take into account three different parts of the detector (the endcaps, the transition region and the barrels).

The energy resolution in ECAL, is reported in Figure 28 as a function of the true energy of the photons. The energy resolution for the electromagnetic calorimeter has been calculated for different ranges of η in [50] and the overall result is:

$$\frac{\sigma_E}{E} = \frac{0.2}{\sqrt{E}} \bigoplus 0.01$$

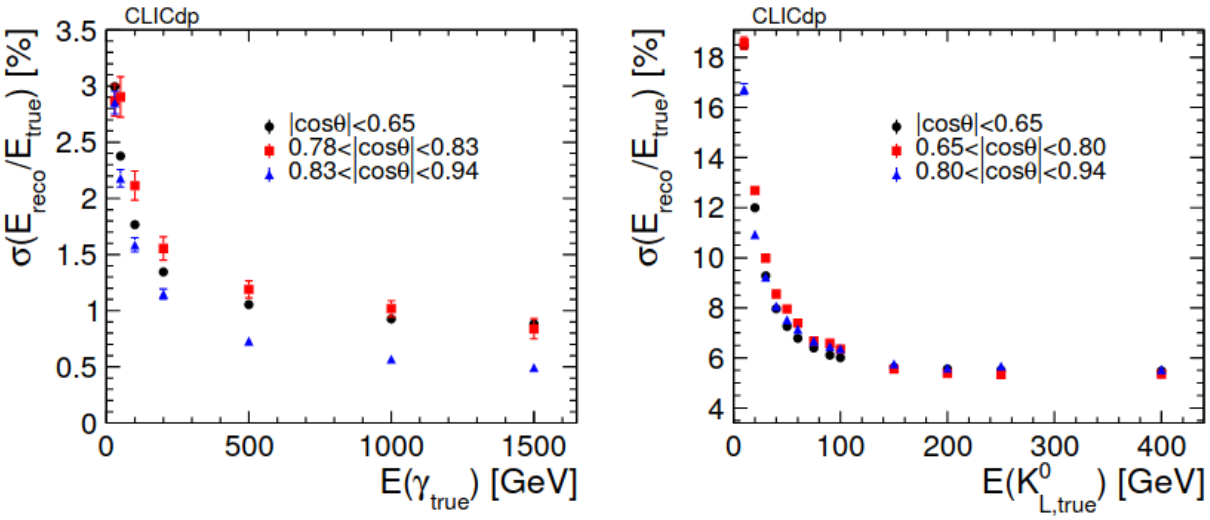

Figure 28: Photon energy resolution (left) and neutral hadron resolutions of K_L^0's (right) as a function of the energy. Results are shown for three different angular regions: barrel region, transition region and endcap.

The energy resolution of the hadronic calorimeter, determined by using K_L^0 is shown as a function of the true energy in Figure 28 right.

The energy resolution for the hadronic calorimeter has been calculated for different ranges of η in [50] and the overall result is found to be:

$$\frac{\sigma_E}{E} = \frac{0.3}{\sqrt{E}} \bigoplus 0.05$$

4.6 Solenoid and Muon detector

A large superconducting solenoid located outside the calorimeters, contains a coil of radius 382 cm, producing a nominal 4 T magnetic field. The solenoid is represented in cyan in Figure 29. The iron yoke return the magnetic flux, and has a magnetic field of 1.5 T pointing in the opposite direction with respect to the inner field. The iron yoke is instrumented with Resisitive Plate Chamber (RCP) sensor layers to act as a muon detector. There are seven RCP layers in the barrel and six layers in the endcaps, with 30×30 mm^2 cell size. The free space between yoke steel layers is 40 mm.

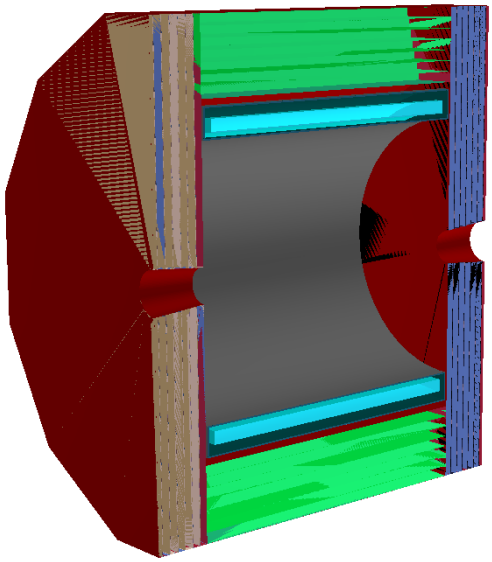

Figure 29: Longitudinal section of the solenoid and muon detectors. In cyan is represented the solenoid. In green and blue are represented the Resistive Plate Chamber layers for the muon detection.

5 Study of the beam-induced background effects on detector components

In this chapter the effects of beam-induced background particles on the detector components are presented. The characteristic distributions of the time of arrival of these particles on the detectors are compared to the distributions of prompt particles, muons coming from the interaction point, to find how to further reduce the amount of background during the data taking by exploiting the time information. In addition to that the software tools used for the analysis presented in this thesis are illustrated.

5.1 Main tools for the simulation

The software for the event simulation and reconstruction used in this thesis is ILCSoftware [51]. The main packages are listed below:

- DD4HEP [52] provides the tools for both the geometry description of the detector and the simulation, by providing the interface with GEANT4 and the reconstruction software;
- GEANT4 [53] [54] provides the tools for the simulation of the passage of particles through matter
- the toolkit Marlin [55] performs the full reconstruction framework, based on processors dedicated to specific tasks: digitization of the simulated hits and event reconstruction.

The relevant processors will be described as they will be encountered.

To study of the effects of the beam-induced background particles on the detector, a Monte Carlo simulation is performed with MARS15 for the beam-induced background particles, that are tracked to the external surface of the detector (see Section 3.3). The simulation of the propagation through the detector is done with GEANT4 toolkit by using the $QGSP\_BERT\_HP$ physics list that allows a precise simulation of thermal neutrons.

5.1.1 GEANT simulation of the beam-induced background

The hits released in the tracker detector layers and in the calorimeter cells, are the output of the GEANT simulation. The spatial positions, the energy deposition and the time of arrival on the detector are stored. The simulation of the beam-induced background in a bunch crossing is CPU intense, therefore, to reduce the computational time, preliminary cuts are applied in order to remove the particles that are not expected to contribute to the signals in the detectors. A conservative time window cut of 10 ns is applied to hits released on the tracker system and on the detector components to mimic data acquisition. Hits outside that time window are rejected. Is has been verified that all beam-induced background particles with time of arrival at the external surface of the detector $t \geq 25ns$ and neutrons with energy $E_n \leq 150$ GeV can be excluded by the GEANT simulation as they will never reach the detector within the data acquisition time window.

5.1.2 Hits digitization

The output of GEANT4 simulation is given as input to the Marlin toolkit for the reconstruction. In order to simulate the effect of the pixels/strips detectors, the hits produced by the particles are digitized. In the framework, the tracker detector does not have yet the complete digitization implemented, and therefore it is approximated by smearing the hits position with a gaussian distribution with a σ equal to the single point resolution of the subdetector in both directions. The corresponding position uncertainties are then set as the single point resolution of the subdetector

resolutions of vertex 3 μm $\times$ 3 μm, inner tracker 5 μm $\times$ 5 μm and all the other elements 7 μm $\times$ 90 μm [56].

Moreover, for the simulation of the timing response, resolutions of σ_T=50 ps and σ_T=100 ps are assumed for the vertex detector and the tracker respectively, applied even in these case as gaussian smearings. These values depend on the thickness of the silicon sensors [57].

For the calorimeter the full digitization is implemented. Each cell of the calorimeter can be crossed by several particles, whose released energy is stored. In the digitization procedure the energies released by particles in each cell with arrival time within the chosen time window are summed. To each cell the time relative to the earlier hit in the time window is associated as time measured by the cell, and the information of the time of arrival of different particles is lost.

5.2 Effects of beam induced background on detector components

The effects on the detector of the large flux of beam-induced background particles surviving the tungsten nozzle are described in this section.

Background particles release a large number of hits in the innermost layers of the tracking system and in the vertex detector.

In order to exploit the different arrival times, the timing distribution of beam-induced background particles is compared to that of particles coming from the interaction point (IP). To this purpose a sample of 10000 muons generated at the interaction point with a flat p_T spectrum between 0.1 and 10 GeV, the polar angle between 8° and 172° and the azimuthal angle between 0° and 360°. They are then propagated through the detector with *GEANT*4. The timing distributions on the first layer of the vertex barrel (left) and the outer barrel (right) are shown in Figure 30.

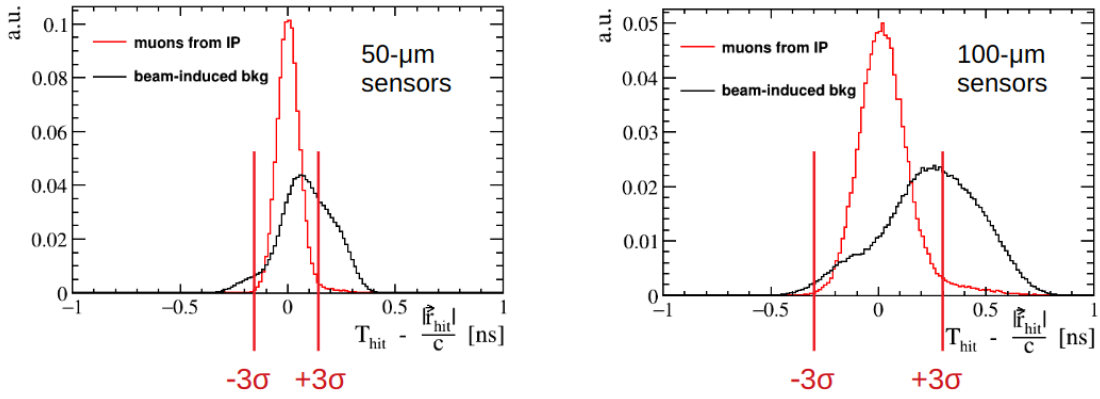

Figure 30: Timing distribution of the hits released by muons generated at the IP and by the beam-induced background particles in the first layer of the vertex barrel (left) and the outer barrel (right). In abscissa T_{hit} is the time of arrival of particles at the layer, and the second term is the time of flight of a photon from the interaction point to the position $r = \sqrt{x^2 + y^2 + z^2}$ of the hit.

With a time cut of $\pm$ 3 σ_T window around 0, where σ_T varies depending on the layer (see section 5.1.2) a huge amount of background hits can be suppressed (black curve of Figure 30), while the major part of the hits released by prompt particles is kept (red curve of Figure 30). The occupancy with the beam-induced background only is shown as a function of the vertex and tracker layers in Figure 31 before (red) and after (blue) the time cut. By applying this cut, the occupancy in the layers of the vertex detector is reduced by more than one third. This have important consequences since the high occupancy in the first layers of the tracking system impacts the track reconstruction.

In the calorimeters, the beam-induced background generates a diffused distribution of energy as displayed on Figure 32. This is similar to the underlying event in pp collider and can be subtracted

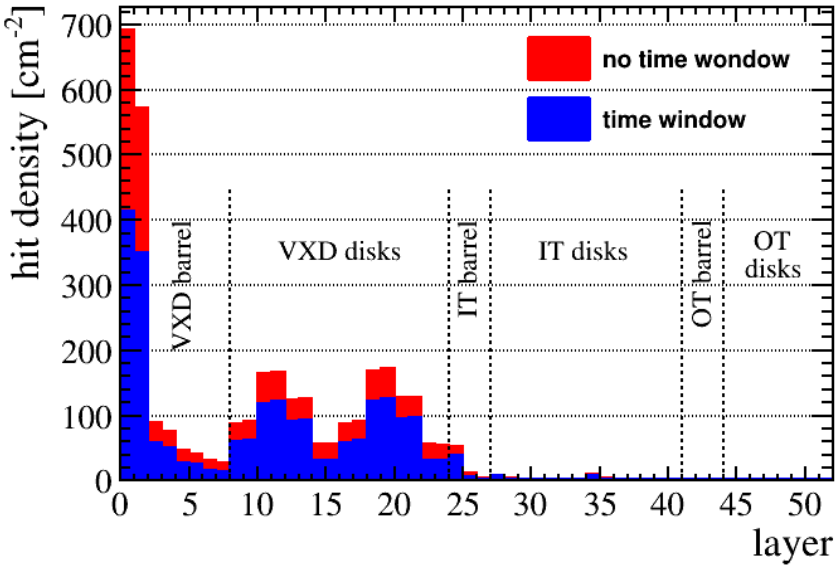

Figure 31: Occupancy for each tracker layer before (red) and after the time cut (blue).

before reconstruction. In Figure 33 the distribution of arrival time of beam-induced background particles on the cells of the calorimeter is shown in black and compared with the same distribution for prompt muons, in red. Also in this case, by applying a proper time window, part of the beam-induced background on the calorimeter can be removed. In the analysis performed in this thesis, the timing window of calorimeters is fixed at 10 ns for each cell. The occupancy defined as the number of energy deposits per mm^2 as a function of the distance from the beam axis is shown in Figure 34. As can be seen it decreases by going deeper in the calorimeters and it is higher in the layers of the electromagnetic calorimeter. In Figure 35 the energy deposited on the barrel of the electromagnetic calorimeter by the beam-induced background particles is shown, compared to the signal $\mu^+\mu^- \rightarrow H\nu\bar{\nu} \rightarrow b\bar{b}\nu\bar{\nu}$ at $\sqrt{s} = 1.5$ TeV. As can be seen most of the energy of the beam-induced background particles (red curve) is released in the first layers of the calorimeter, while the signal releases its energy deeper in the calorimeter (blue curve). A possible solution to reduce the energy released by background particles is to insert an absorber pre-shower in front of the calorimeters.

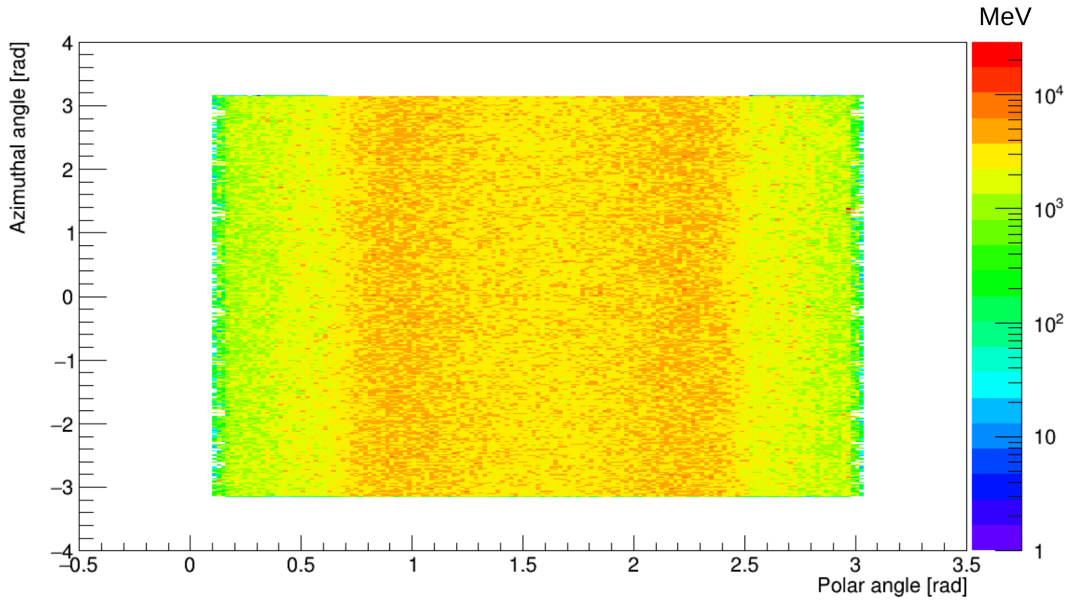

Figure 32: Energy distribution of beam-induced background particles in the calorimeters as a function of the polar and azimuthal angle

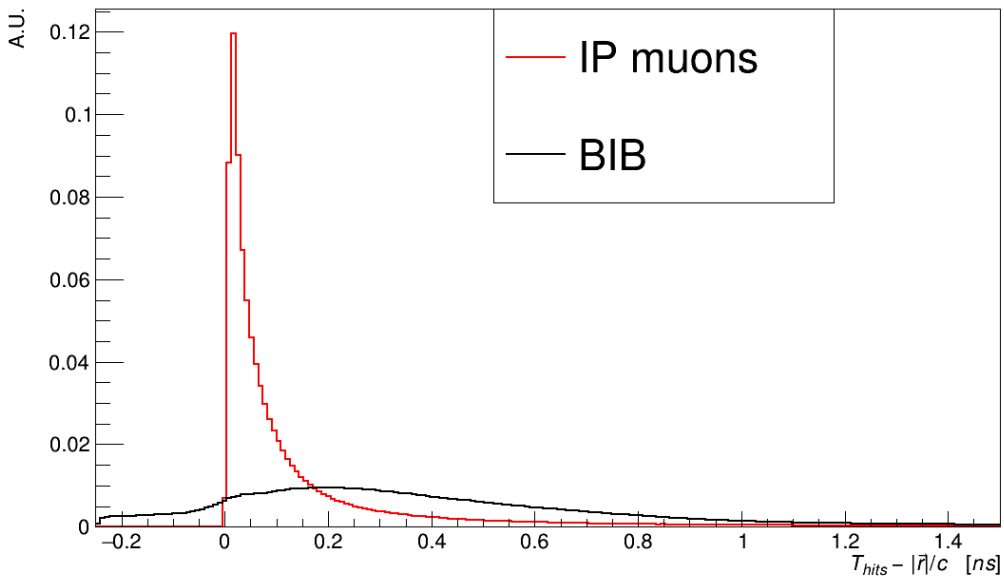

Figure 33: Distributions of the time of arrival of particles at the calorimeter cells for prompt muons (red) and beam-induced background particles (black).

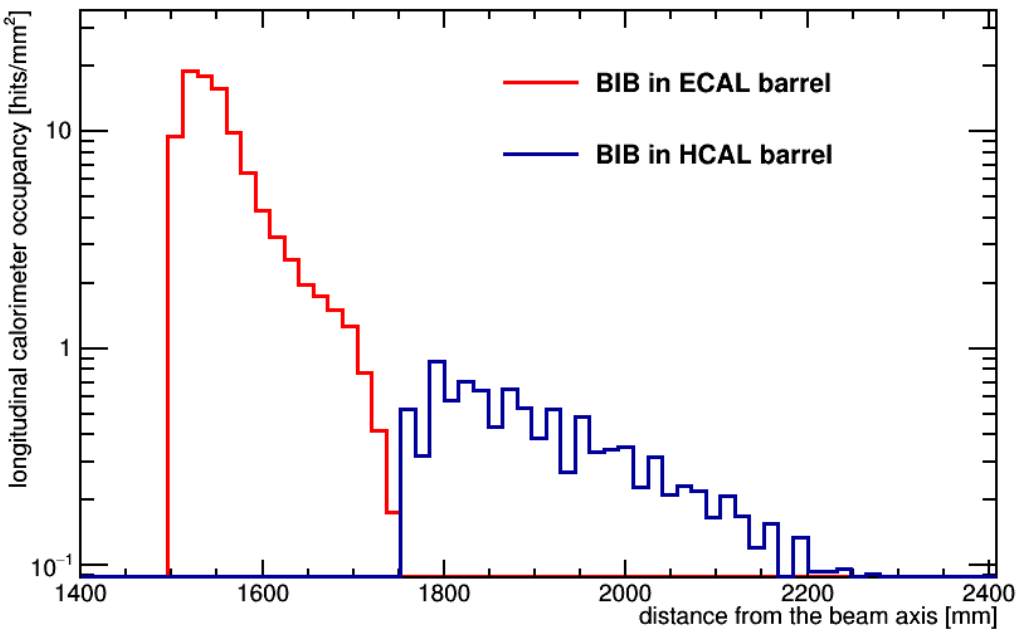

Figure 34: Hits density on the barrel of the electromagnetic calorimeter (red) and the hadronic calorimeter (blue) as a function of the distance from the beam axis.

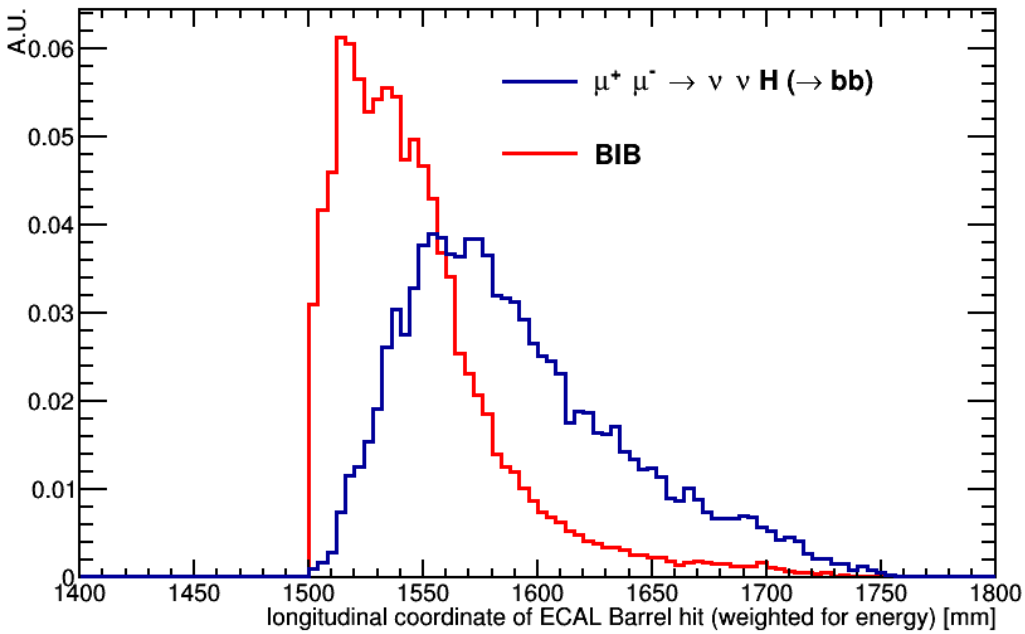

Figure 35: Distribution of the energy released by beam-induced background particles in the barrel of the electromagnetic calorimeter (red), compared to the signal $\mu^+\mu^- \rightarrow H\nu\bar{\nu} \rightarrow b\bar{b}\nu\bar{\nu}$ at $\sqrt{s} = 1.5$ TeV.

6 Event reconstruction

The experimental signatures of quarks and gluons produced in high energy experiments are jets, collimated streams of particles produced in the fragmentation process, whose reconstruction is presented in this chapter together with the track finding methods. The event reconstruction foresees also the electrons, photons and muons identification. In the software this is performed by combining information from the various sub-detectors.

The full reconstruction consists of the following steps:

- tracks reconstruction in the tracking system;
- identification of muons, hadrons, electrons and photons with PandoraPFA;
- jet reconstruction with FastJet.

6.1 Track finding and fitting

The digitization of tracker hits was described in Section 5.1.2, after that, the track reconstruction can be divided in three main steps:

- the conformal algorithm, that performs the pattern recognition;
- the track fitting done by using a Kalman method;
- good tracks selection.

6.1.1 Conformal tracking method

The Conformal Tracking [56] is a pattern recognition technique for track finding that combines the concepts of conformal mapping and cellular automata.

The conformal mapping [58] consists in the transformation of point coordinates in global Euclidean space (x, y) into the conformal space coordinates (u, v). The idea behind this coordinates transformation is that curved tracks left by charged particles bent by that magnetic field are mapped into straight lines in the conformal space by defining the (u, v) coordinates as:

$$\begin{aligned} u &= \frac{x}{x^2 + y^2} \\ v &= \frac{y}{x^2 + y^2} \end{aligned} \tag{6.1}$$

The equation of a circle, $(x - a)^2 + (y - b)^2 = r^2$, is translated into a straight line:

$$v = -\frac{a}{b}u + \frac{1}{2b} \tag{6.2}$$

In the conformal space the radial order of the hit positions is inverted with respect to the (x, y) coordinates, then track hits in the inner layers of the tracker system described in section 4.2 correspond to larger (u, v) coordinates than hits in the outer layers. This approximation by a straight line is not valid for all particle trajectories, as they can be not originated at the origin of the (x, y) plane (displaced tracks) and possible deviation in real experiment can be caused by particle multiple scattering. By performing the pattern recognition in the conformal space with a cellular automaton (CA), these deviations are taken into account.

Full tracks are then created by the CA algorithm [59] in several steps, that are briefly reported. A more detailed description can be found in appendix A, where the default parameters of the algorithms are also reported (Table 21).

- **Building of cellular tracks candidates**
  Hits surviving the timing windows fixed in Section 5.2 are used as input. In this first step, the hit collection relative to the first layer of the vertex detector is taken as input and all hits are considered the starting point of a cellular track candidate. Cellular tracks are built by chaining *cells*, that are defined as follow [60]: *seed cells* are built by connecting *seed hits* to hits belonging to layers with smaller conformal radius, that satisfy the criteria: lay within a window of polar angle $\Delta\Theta_{neigh}$ in the conformal space and they are not already part of a track. Seed cells are then prolonged in the radial direction of the conformal space: new cells of maximum length l_{max} are created and chained. The new cells that forms an angle larger than α_{max} with respect to the seed cell are discarded. A *weight* is associated to each cell, that is much higher when a cell can potentially be linked to more cells. Finally cellular tracks are created starting from the highest weighted seed cell. A minimum number of hits N_{min}^{hits} for each candidate is required. The candidates are then fitted with a linear regression to obtain the parameters in Equation 6.1.1 and cellular track are selected if the normalized χ^2 is less than a χ^2_{max}.

- **Extension of cellular track candidates**
  Cellular tracks are extended according to the particle transverse momentum estimated from the linear regression fit. Tracks with a transverse momentum above a threshold $p_{T,cut}$ are extended first. The extension procedure and the best track candidate selection are similar to the case of the cellular track building [60]. For the extension of tracks with $p_T < p_{T,cut}$ a different procedure is applied, as low p_T tracks will tend to loop in the tracker due to the magnetic field [56].

The building and extension algorithms are executed with several iterations and different tuning of the parameters (see Table 21 in appendix). The pattern recognition is one of the main challenges in track reconstruction at a muon collider, due to the high number of hits in the innermost layers generated by the beam-induced background. Several studies will have to be done in the future to adapt this algorithm to the muon collider environment or determine one optimal.

6.1.2 Track fitting

As mentioned above, the output of the pattern recognition are the cellular tracks candidate. The trajectory followed by a charged particle in an uniform magnetic field and in absence of multiple scattering or energy loss in detector materials is helical, and can be specified by five parameters, once a reference point x_0, taken here the interaction point, is fixed:

Parameter	Description
D_0	the distance between the helix and the reference point in the x-y plane
Φ	the azimuthal angle of the reference point with respect to the center of the helix
Ω	the signed curvature of the track, defined as $\Omega = \frac{p_T}{cBQ}$, where B is the magnetic field and Q is the charge of the particle
Z_0	the distance between the helix and the reference point in the z direction
$tan(\lambda)$	the dip angle, i.e., the angle of the helix to the x-y plane

Table 17: Track parameters definition.

In this case the simplest way to extract the track parameters is to perform a χ^2 fit of the hits belonging to the track, under the assumption that the particle trajectory is a perfect helix. Nevertheless, this assumption is not valid in the presence of multiple scattering and energy loss, because they introduce displacement of the hits from the ideal helix. The Kalman filter algorithm

[61], used to perform track fit in this thesis, deals with systems that evolves according to an equation of motion with random deviations. The track fit develops in these steps:

- **Pre-fit**
  First a simple helix is fitted to three hits of the track (usually the first, middle and last hits). In this way a first estimation of the track parameters is obtained.

- **Kalman Filter**
  These parameters are used to initialize the Kalman filter. In this analysis it starts from the innermost to the outermost layer of the detector. The Kalman filter proceeds through the full list of hits on the track, and updates track vector parameters every time an hit is added, tacking into account the multiple scattering and effects of energy loss.

6.1.3 Good track selection

A selection procedure is applied to ensure good quality tracks. In order to avoid tracks with more than two hits shared, a selection procedure is performed based on the length of the tracks and on the χ^2. Tracks with longer length and lower χ^2, as calculated at the end of the Kalman filter, are kept. In case of equal length, tracks with the best χ^2 are chosen, while longer tracks are usually preferred. Furthermore, a minimum number of three hits is required, in order to reject bad quality tracks.

6.2 Tracking performance

The tracking performance is studied by using a sample of 1000 muons generated with a flat p_T spectrum between 0.1 and 10 GeV, polar angle between 8° and 172° and azimuthal angle between 0° and 360°, with and without the beam-induced background superimposed.

Events reconstruction within the detector acceptance is highly computational demanding because the high number hits on the tracker layers in the presence of the beam-induced background.

To overcome this problem, the detector is split in different angular regions. Figure 36 shows the $y - z$ view of the vertex and the tracker detectors layers. In red the regions used for the "regional" tracking.

The very forward regions are still under study; here the acceptance is limited to $24° < \theta < 156°$. When only muons are reconstructed the number of tracks found is 881, while when the beam-induced background is superimposed 89873 tracks are reconstructed, if no quality cuts are applied.

Figure 37 and Figure 38 show the total number of hits in the tracker and the reduced χ^2 in the two cases respectively. The distributions are normalized at the unitary area in order to compare the shapes of the distributions. Most of the tracks reconstructed in the presence of beam-induced background particles (blue line) have a lower number of hits and higher reduced χ^2 respect to single muons (red line). By requiring $N_{hits} > 6$ and $\chi^2 < 5$, the 98% of the beam-induced background tracks are rejected.

In order to evaluate the possible track degradation due to the presence of the beam-induced background, the parameters of the tracks after the cuts are presented, with their error. In Figure 39 the distributions of the impact parameter and the error on it are shown. Since muons are generated from the interaction point, the distributions for prompt muons (red) and muons with beam-induced background (blue) are peaked at zero. However, the addition of beam-induced background particles introduces hits in the muon reconstruction that broaden the D_0 distribution. Moreover beam-induced background tracks not matched to muons are present. Note that beam-induced background tracks are not constrained to start from the interaction point. The distribution of the error on D_0 shows higher error when the BIB is present, this is due to the high occupancy in particular in the

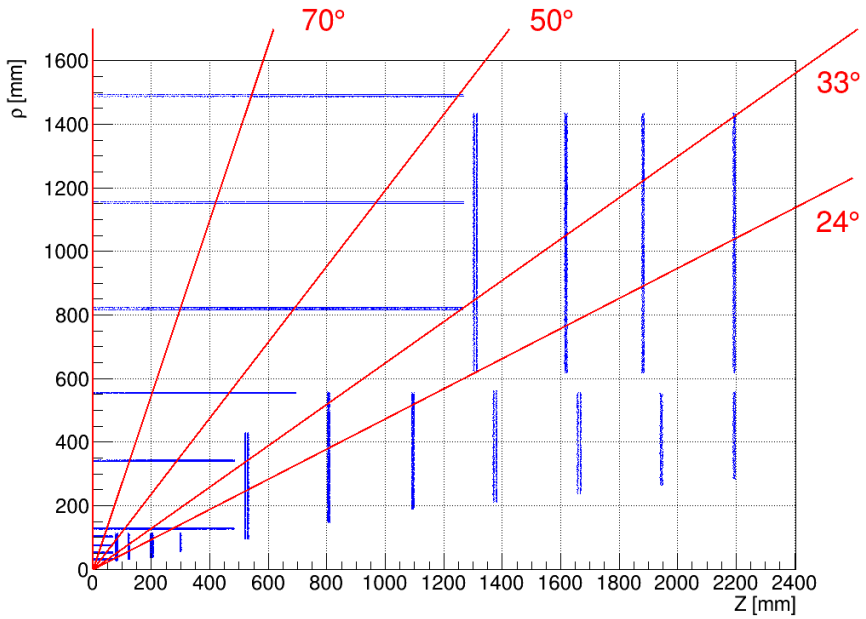

Figure 36: Angular splitting of the detector acceptance, for studies of the track reconstruction performances with the beam-induced background superimposed. The same split is done for the left side of the detector.

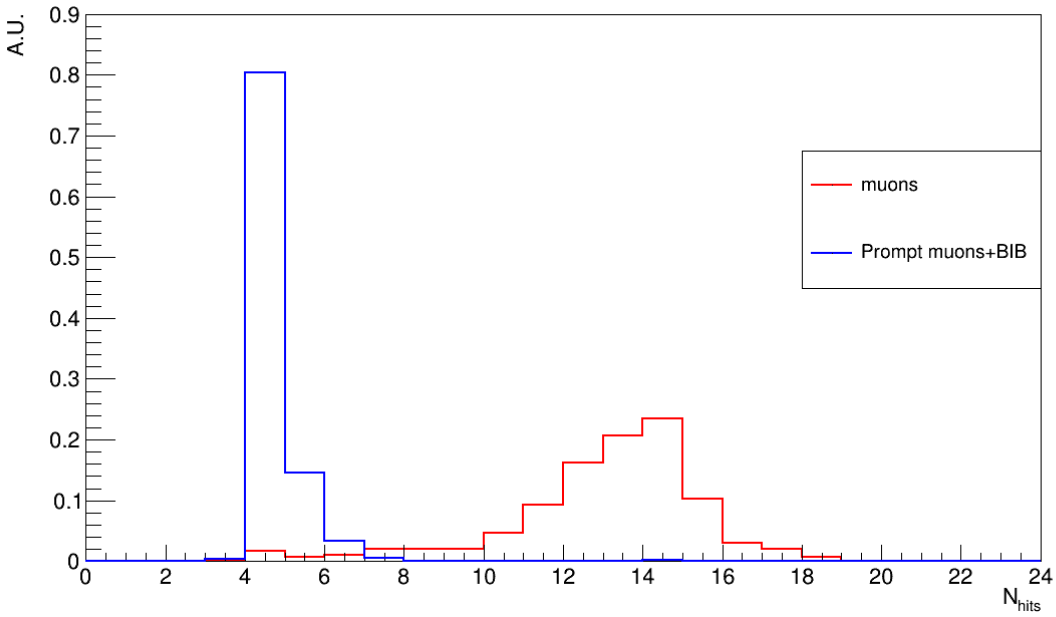

Figure 37: Total number of hits for single muons (red) and muons with beam-induced background (blue). Distributions are normalized at the unitary area.

first layers and the usage of wrong hits to build the track. Similar considerations can be done for the longitudinal impact parameter Z_0 whose distributions are shown in Figure 40.

The distribution of the parameter Ω is shown in Figure 41. Ω is greater than zero for positive charged particles, and less than zero for negative charged particles. Since the muon sample is

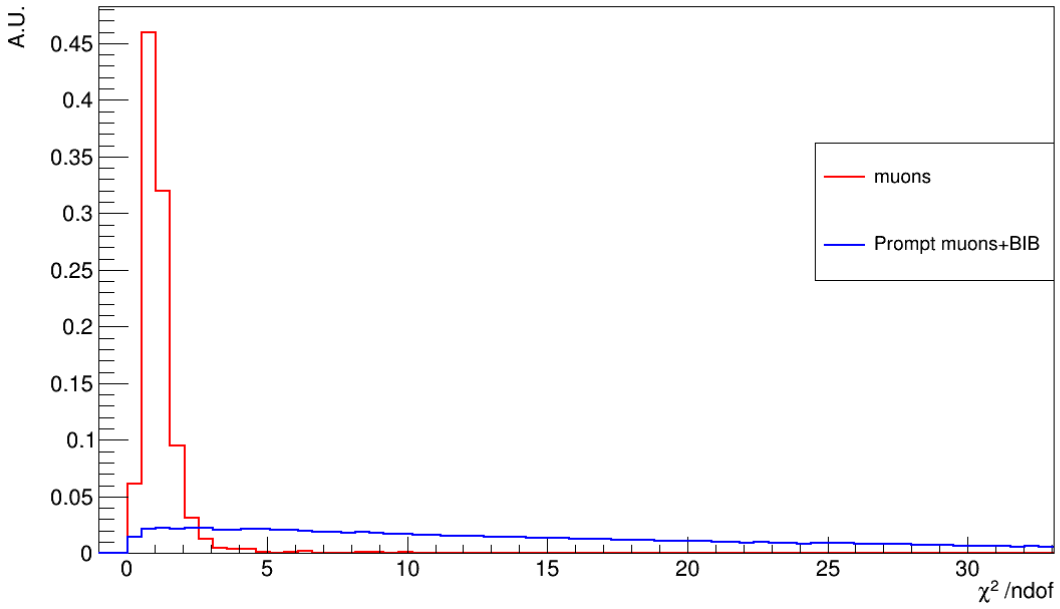

Figure 38: Distribution of the reduced χ^2 for single muons (red) and muons in the presence of the beam-induced background (blue). Distributions are normalized at the unitary area.

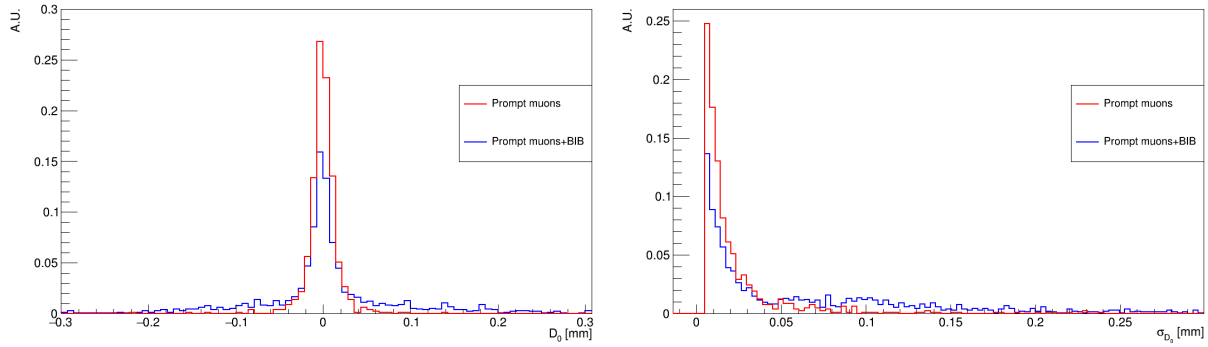

Figure 39: Left: tracks impact parameter distributions for a sample of prompt muons (red) and for a sample of muons in the presence of the beam-induced background (blue). Right: error on the impact parameter.

composed by an equal number of μ^+ and μ^- the distribution is symmetric. The distribution becomes asymmetric when the beam-induced background is superimposed to the muons sample, since there is an higher number of negative charged particles with respect to positive. The gap around zero is due to the lower limit cut on the transverse momentum of particles, that is set at 0.1 GeV. The track transverse momentum is obtained from the Ω parameter via:

$$p_T[\text{GeV}] = \frac{0.3B[\text{T}]}{\Omega[1/\text{m}]} \tag{6.3}$$

and errors on p_T are obtained via error propagation. Figure 42 shows the distribution of the tracks transverse momentum. As expected the p_T distribution for muons is uniform. The presence of BIB generates the peak of low momentum tracks. The error distributions reflect this composition, tracks with higher momentum have a larger error.

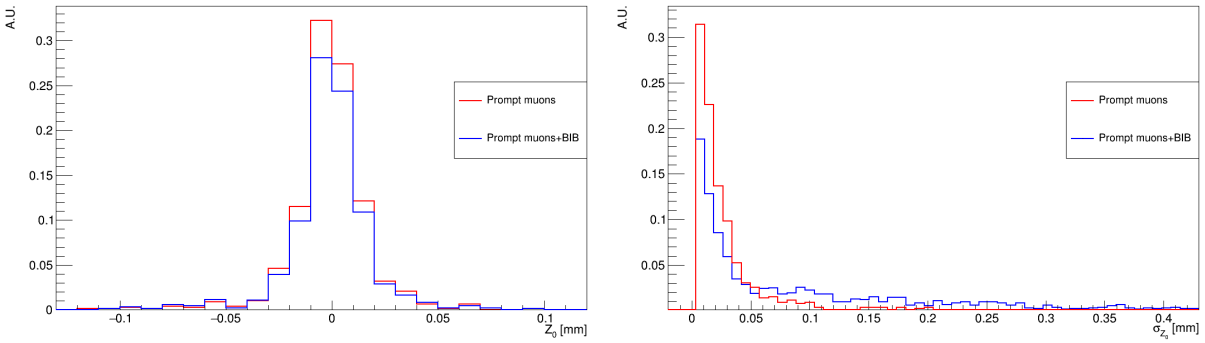

Figure 40: Left: Distribution of the Z_0 parameter (defined in table 17) for a sample of prompt muons (red) and for a sample of muons in the presence of the beam-induced background (blue). Right: error on the Z_0 parameter.

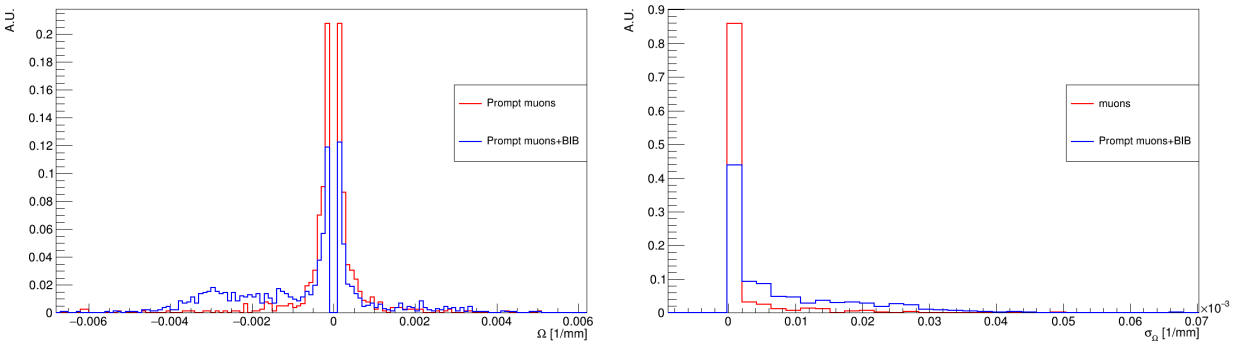

Figure 41: Left: Distribution of the Ω parameter (defined in table 17) for a sample of prompt muons (red) and for a sample of muons in the presence of the beam-induced background (blue). Right: error on the Ω parameter.

The distribution of the $tan(\lambda)$ parameter is shown in Figure 43. From this parameter the polar angle θ can be extracted by using the relation:

$$\theta = \frac{\pi}{2} - \arctan(\tan(\lambda)) \tag{6.4}$$

and the distributions are shown in Figure 44. The θ distribution is uniform, as expected for the sample with only muons, while in the presence of the beam-induced background, tracks at small angles with respect to the z axis appear as expected due to origin of such particles.

The distributions of the azimuthal angle and its errors for the two samples are shown in Figure 45 and, as expected, it is uniform for both samples.

This study shows that the presence of the BIB introduces tracks with low momentum and worsen the error on the track parameter. The selection criteria to define "good" tracks have to be optimize after the study with hadrons (kaons and/or pions) will be repeated. Given the results obtained so far, it is evident that a proper optimization, for example by requiring a minimum number of hits per layer, different layer per layer, will allow to get rid of the BIB for track with $p_T > 1$ GeV or so. A detailed investigation and probably a different tracking strategy will be needed for low momentum tracks.

The track reconstruction efficiency is defined as:

$$\epsilon_{trk} = \frac{N_{reco}}{N_{tot}} \tag{6.5}$$

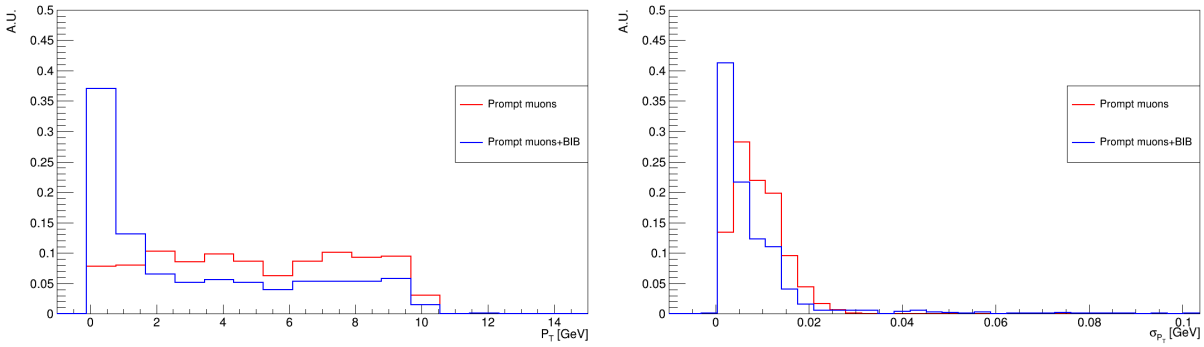

Figure 42: Left: Distribution of the measured track p_T for a sample of prompt muons (red) and for a sample of muons in the presence of the beam-induced background (blue). Right: error on the measured track p_T.

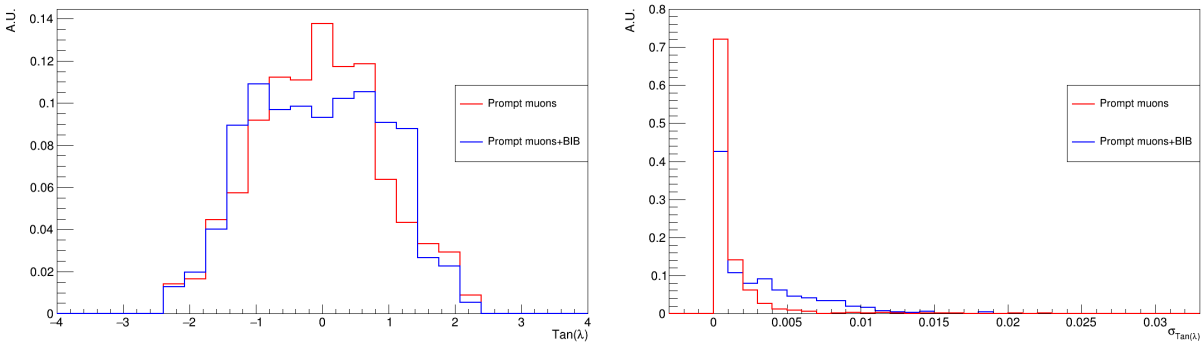

Figure 43: Left: Distribution of the tan(λ) parameter (defined in table 17) for a sample of prompt muons (red) and for a sample of muons in the presence of the beam-induced background (blue). Right: error on the tan(λ) parameter.

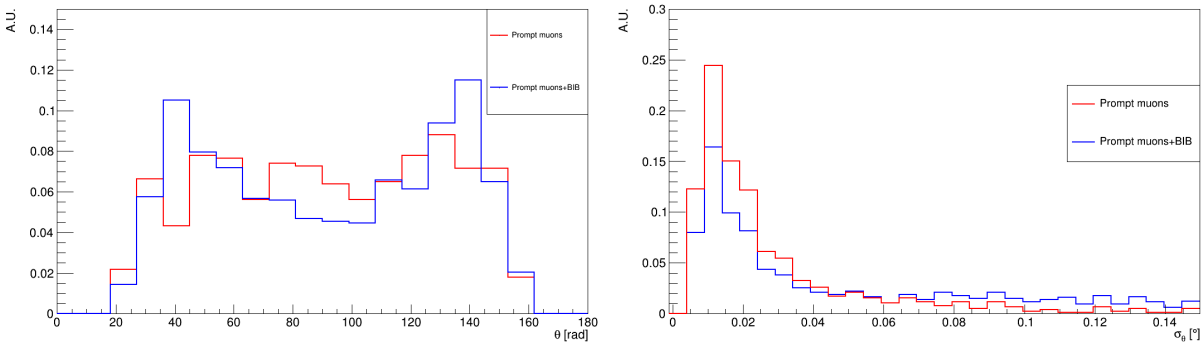

Figure 44: Left: Distribution of the measured track θ for a sample of prompt muons (red) and for a sample of muons in the presence of the beam-induced background (blue). Right: error on the measured track θ.

where, N_{tot} is the number total reconstructable Monte Carlo particles, defined as having $p_T > 0.1$ GeV and at least 4 hits in different layers of the detector. N_{reco} is the number of reconstructed Monte Carlo particles. These are defined as Monte Carlo particles sharing at least one hit with the reconstructed tracks. If more than one track share hits with the MC particle, the one that

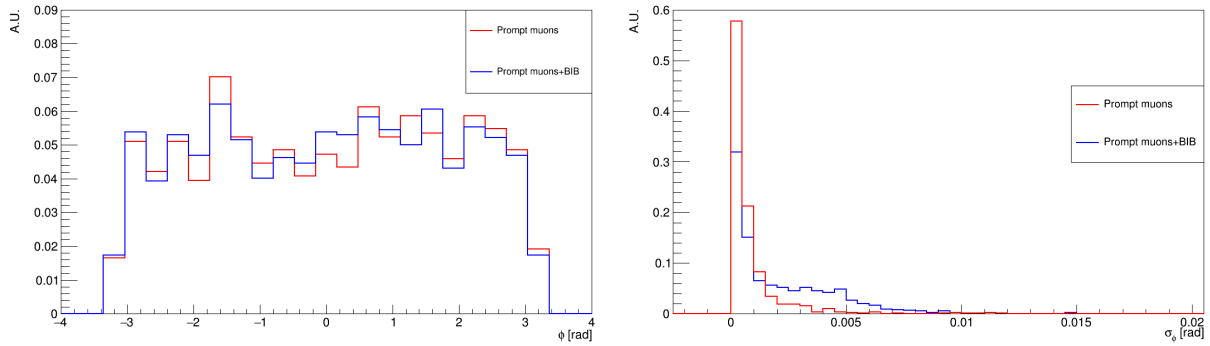

Figure 45: Left: Distribution of the measured track ϕ for a sample of prompt muons (red) and for a sample of muons in the presence of the beam-induced background (blue). Right: error on the measured track ϕ.

shares the maximum number of hits is kept. Figure 46 shows the track reconstruction efficiency as a function of the Monte Carlo particle transverse momentum (left) and polar angle (right).

The main loss in efficiency is due to low p_T tracks. As can be seen, in Figure 46 left for tracks with $p_T < 1$ GeV the efficiency is around 90% for prompt muons, and around $30 - 40\%$ in the presence of the beam-induced background. In Figure 46 there are losses in efficiency in the presence of the beam-induced background for two θ ranges: $20 < \theta < 40$ and $50 < \theta < 70$. This is again due to low transverse momenta particles, as it has been verified that by requiring $p_T > 1$ GeV, the efficiency improves up to $90 - 100\%$.

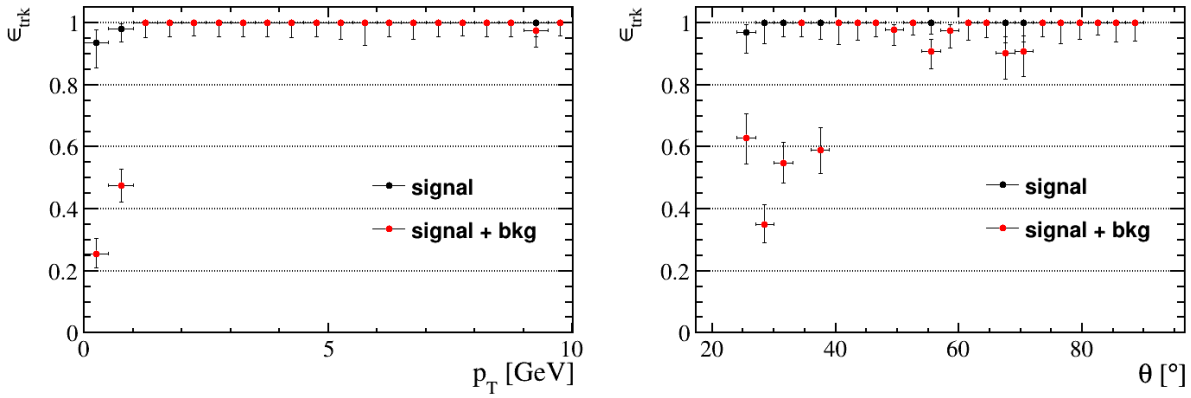

Figure 46: Tracking efficiency as a function of p_T (left plot) and θ (right plot) for a sample of prompt muons (black) and for a sample of muons in the presence of the beam-induced background (red).

The resolution of the tracks transverse momentum has been then evaluated as a function of the p_T and θ.

$$\frac{\Delta p_T}{p_T^2} = \frac{p_{T,MC} - p_{T,track}}{p_{T,MC}^2} \tag{6.6}$$

where $p_{T,MC}$ is the transverse momentum of the Monte Carlo particle and $p_{T,track}$ is the transverse momentum of the reconstructed track associated to the Monte Carlo particle.

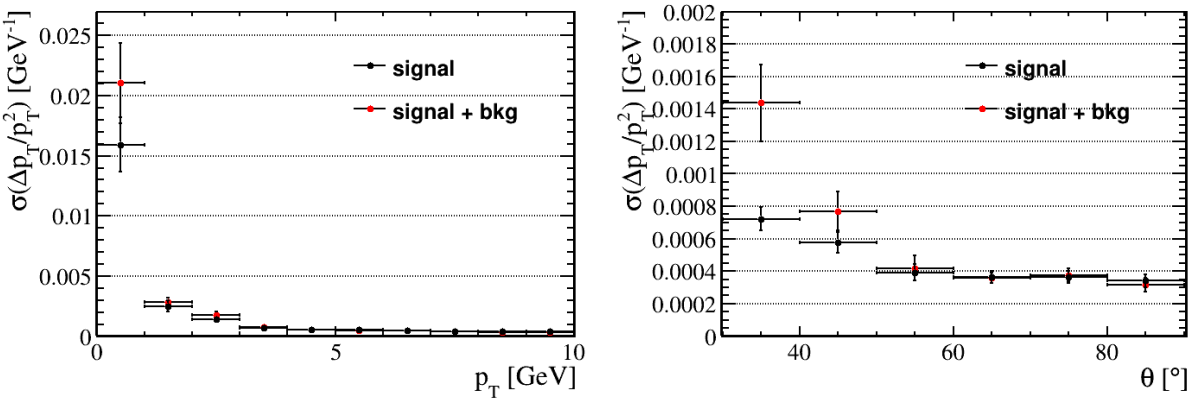

Figure 47: Resolution of the measured track p_T as defined in equation 6.6 as a function of p_T (left plot) and θ (right plot) for a sample of prompt muons (black) and for a sample of muons in the presence of the beam-induced background (red).

6.3 Jet Reconstruction

Jets manifest in the detector as collimated groups of tracks from charged particles in the tracker system and as concentrations of energy in calorimeters. In this chapter techniques for jet reconstruction used in the data analysis of Section 7 are presented. The main steps are:

- the particle flow approach [62] is used as for the reconstruction of all visible charged and neutral particles by exploiting information from both the tracker and the calorimeter system;
- the k_T algorithm [63], takes the particles reconstructed by the particle flow algorithm and clusterize them into jets;
- E-recombination scheme gives the scheme to compute the final jet four momentum.

6.4 Particle Flow

The particle flow approach [64] relies on the idea that energy and momentum for each particle can be extracted from the sub-detector system in which the measurement is expected to be most accurate. The correct reconstruction of particles energy and momentum is fundamental in order to obtain a good jet energy resolution. In a typical jet approximately most of the energy is carried by charged particles (mainly hadrons), a smaller fraction is carried by photons and long-lived neutral hadrons and neutrinos.

In a full calorimeter reconstruction approach the jet energy is obtained from the sum of the energies deposited in the electromagnetic and hadronic calorimeters (ECAL and HCAL). In this case the jet energy resolution is limited by the poor energy resolution of the hadronic calorimeters [65].

The particle flow approach improves the jet energy resolution as charged particle momenta can be measured precisely in the tracker detector, while photon energies can be obtained from the energy deposits in the ECAL. The HCAL is then only used to measure the 10 % jet energy carried by long-lived neutral hadrons.

This concept is schematically expressed in Figure 48, where the standard calorimetric approach (left) is compared to the Particle Flow approach (right).

The particle flow approach is adopted in ILCSoftware and it is expected to reach the target jet energy resolution of $\frac{\sigma_E}{E} \lesssim 3.5\%$ [64], sufficient to cleanly separate W and Z hadronic decays, via the reconstruction of the di-jet invariant masses for 50-500 GeV jets at the ILC and for up to 1.5

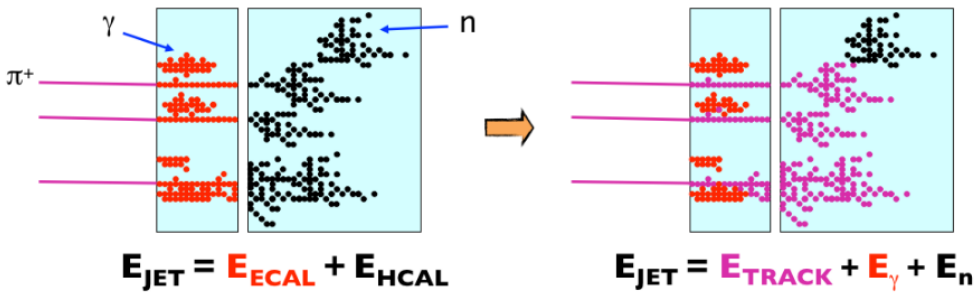

Figure 48: Schematization of standard (left) and particle flow (right) methods for jet reconstruction.

TeV jets at CLIC. It is not possible to reach this resolution with the full calorimetric approaches, in which the 72 % of the energy would be measured in the HCAL, with a typical resolution of $\frac{\sigma_E}{E} \gtrsim 55\%\sqrt{E/GeV}$. The performance of the algorithm at a muon collider has to be studied.

6.4.1 PandoraPFA algorithm

Digitized calorimeter hits and charged particles tracks are given as input to the PandoraPFA, that produces as output reconstructed particles known as particle flow objects. The PandoraPFA algorithm, described in detail in [65], performs calorimeter clustering and the Particle Flow reconstruction in eight main stages (further details can be found in Appendix B, while default values used in the algorithms can be found in the repository [66]):

- Track Selection/Topology: tracks are projected into the front face of the electromagnetic calorimeter. Tracks topologies such as kinks (charged particle decaying into a single charged particles plus neutral particles) or decays of neutral particles into a pair of charged particles are identified.

- Calorimeter Hits Selection and Ordering: a minimum ionising particle (MIP) energy cut is applied to the calorimeter the list of digitized calorimeter hits and their energy is corrected by using the software compensation technique [67], in order to take into account the invisible energy not detected in the hadronic calorimeter.

- Clustering: hits are grouped into clusters by using a cone-based clustering algorithm. It exploits the fact that the direction of the released calorimeter hits is almost the same of the original particle. The algorithm starts by considering as seed the hits corresponding to the projection of the reconstructed tracks onto the front face of the electromagnetic calorimeter as can be seen in Figure 49. The track direction at the ECAL front face determines the initial direction of the cone. If seed calorimeter hits are not associated to projection of any track, the initial cone direction is taken from the interaction point to the calorimeter hit. A cone with a opening angle is formed around the direction of the seed. Calorimeter hits are looped over on a per layer basis, starting from the innermost and going to the outermost layer. Hits that lie within cone defined by existing cluster, and are sufficiently close, are added to the cluster. Unmatched hits, are used to seed new clusters.

- Topological Cluster Merging: neutral clusters that are not already associated to tracks are merged with clusters that have an associated tracks (charged clusters).

- Statistical Re-clustering: if there are discrepancy between the cluster energy and any associated track momenta clustering algorithms are run again, with different configuration parameters.

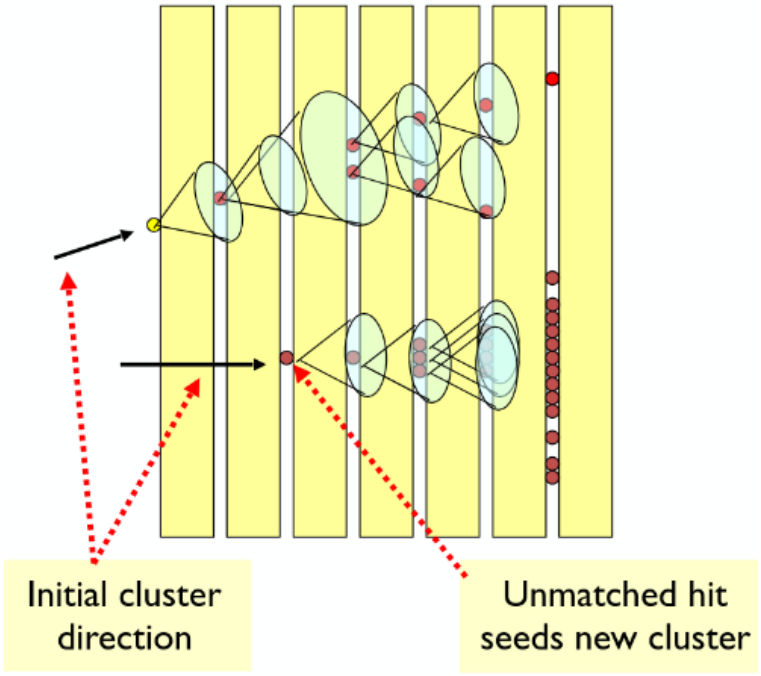

Figure 49: Illustration of the cone-based clustering algorithm used in PandoraPFA, taken from [68]

- Photon Recovery and identification: clusters of calorimeter hits consistent with photons are identified.
- Fragment Removal: remaining neutral clusters that are not identified as photons are merged to charged particle hadronic showers
- Formation of particle Flow objects: reconstructed particle are created. The energy for charged particles is calculated from the track momenta, while neutral particle energies are taken from calorimeter measurements.

6.5 Jet clustering with the kT algorithm

Particles selected by the Particle Flow are used as inputs in the jet clustering algorithm. Several jet finding algorithm exist and are provided by the FastJet package [63] used in this analysis: the one used in this thesis is the "k_T" [69] algorithm that works as follow:

1. a list of all the input particles is created
2. For each pair of particles i, j the k_T distance is calculated:

$$d_{ij} = min(p_{ti}^2, p_{tj}^2)\frac{\Delta R_{ij}^2}{R^2}$$

   with $\Delta R_{ij}^2 = (y_i - y_j)^2 + (\phi_i - \phi_j)^2$, where p_{ti},y_i and ϕ_i are the transverse momentum, rapidity and azimuth of particle i. R is a jet-radius parameter and is taken as 0.7 in this analysis.

3. the distance between each particle i and the beam is calculated with

$$d_{iB} = p_{ti}^2$$

4. The minimum d_{min} of all the d_{ij}, d_{iB} is found. If d_{min} is a d_{ij}, particles i and j are merged into a single particle summing their four-momenta: by considering the 4-momenta $p_i = (E_i, \vec{p}_i)$ the E-recombination scheme the jet 4-momentum is computed as:

$$p_{jet} = (E_{jet}, \vec{p}_{jet})$$

where $E_{jet} = \sum_i E_i$ and $p_{jet} = \sum_i p_i$. If d_{min} it is a d_{iB} then particle i is declared to be a final jet and is removed from the list.

5. if no more particles are in the list the algorithm ends, otherwise it restarts from step 2.

6.6 Jet reconstruction efficiency

In this section the performance of the jet reconstruction algorithms are evaluated by using simulated data. Two classes of jets are reconstructed:

- Monte Carlo jets (jet_{MC}) obtained by clustering the stable truth-level particles (with lifetime $\tau > 10^{-8}s$) are characterized by having the true kinematical quantities, as they are not affected by the detector reconstruction efficiencies;
- reconstructed jets (jet_{reco}) are reconstructed by using detector information.

The differences between jet energies of jet_{reco} and jet_{MC} are evaluated to assess the jet algorithm performance. For this purpouse a simulated sample of 1000 events of $\mu^+\mu^- \to HH\nu\bar{\nu} \to b\bar{b}b\bar{b}\nu\bar{\nu}$ at $\sqrt{s} = 3$ TeV are used. In the Monte Carlo collection, b and $\bar{b}$ quarks are saved with all the relative kinematic variables. Reconstructed jets are matched with truth-level jets associated to b quarks by minimizing the distance in the (η,ϕ) plane. Such distance is calculated as $\Delta R = \sqrt{\Delta\eta^2 + \Delta\phi^2}$, where $\Delta\eta = \eta_{reco} - \eta_{jet_{MC}}$ and $\Delta\phi = \phi_{reco} - \phi_{jet_{MC}}$, it is also required $\Delta R < 0.5$.

For each interval in p_T the standard deviation of $p_{T,reco}$ of the reconstructed jets matched with the jet_{MC} are calculated. In Figure 50 the jet_{reco} transverse momentum is shown, as a function of the truth-jet transverse momentum.

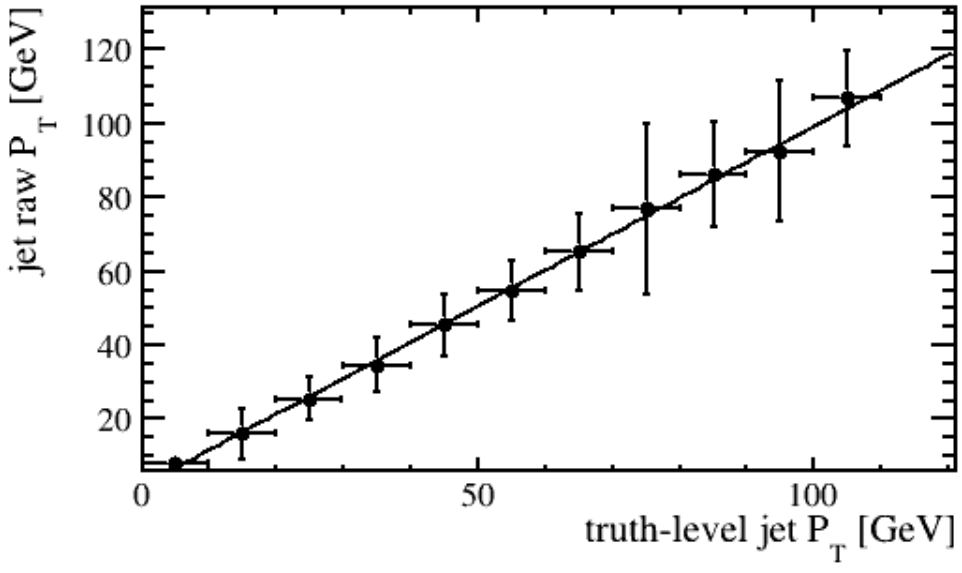

Figure 50: Reconstructed jet P_T as a function of the truth-level jet P_T

The plot is fitted by a function $y = a \cdot x + b$. The result of the fit gives $a = 2 \pm 4$ and $b = 1.0 \pm 0.1$.

Being the intercept of the fit compatible with 1, it can be concluded that the transverse momentum of jet_{reco} is well correlated to the transverse momentum of jet_{MC}.

The jet reconstruction efficiency is calculated as a function of the trasverse momentum of jets and is calculated as:

$$\epsilon = \frac{N_{true,matched}}{N_{true,matched} + N_{true,unmatched}}$$

where $N_{true,matched}$ is the number of true jet matched with reconstructed jets, while at the denominator there is the total number of truth-level jets.

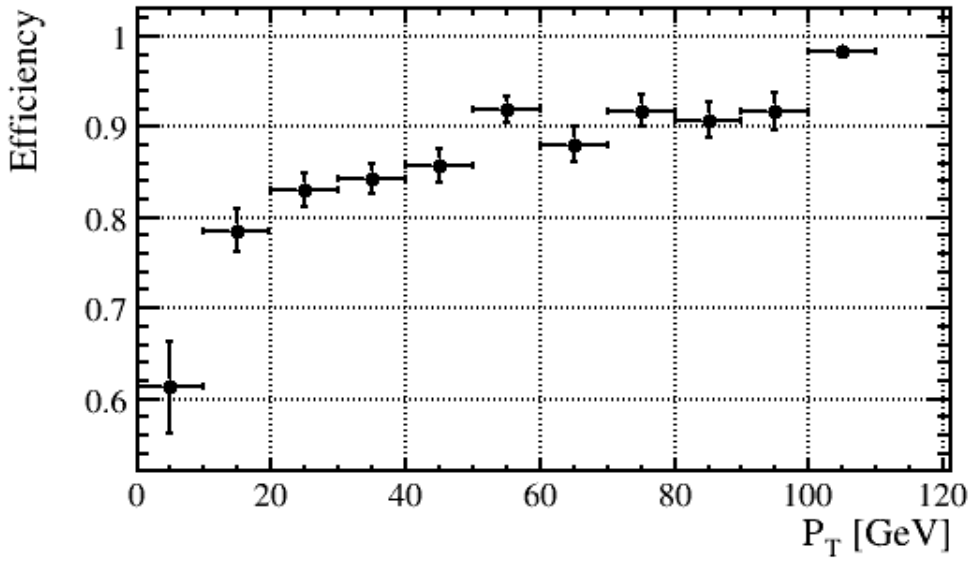

Figure 51: Jet reconstruction efficiency as a function of the jet transverse momentum.

As can be seen in Figure 51 the reconstruction efficiency is around 90 % for $p_T > 50$ GeV while goes to 60% for low $p_T \sim 10$ GeV jets.

The jet transverse momentum resolution is then evaluated. The jet_{MC} are divided into the same intervals in p_T as before, and for each jet the transverse momentum resolution has been calculated as:

$$\frac{\Delta p_T}{p_{T,MC}} = \frac{p_{T,MC} - p_{T,reco}}{p_{T,MC}}$$

Then each p_T interval, the gaussian fit of the distribution of the jet transverse momenta is performed. In Figure 52 can be seen the sigma of the gaussian fit as a function of the p_T. The resolution on the jet transverse momentum is lower than 10% for jets with $p_T > 20$ GeV, while it is higher for jets with $p_T < 20$.

6.7 b-tagging algorithm

The identification of jets originated by heavy quarks (in general b and c jets) is performed via flavour tagging tagging algorithms. The one available in the ILCSoftware has to be optimized for muon collider environment. Therefore the analysis described in Section 7 is performed by assuming the efficiencies on the identification of b jets calculated in [17]. Such efficiencies are expected to be the same in the two analysis, since the vertex detector characteristics are the identical.

In [17] a b-tagging algorithm was optimized to reduce the beam-induced background at 1.5 TeV center of mass energy and its efficiency was evaluated by using b jets coming from the $\mu^+\mu^- \to H\nu\bar{\nu} \to b\bar{b}\nu\bar{\nu}$ process.

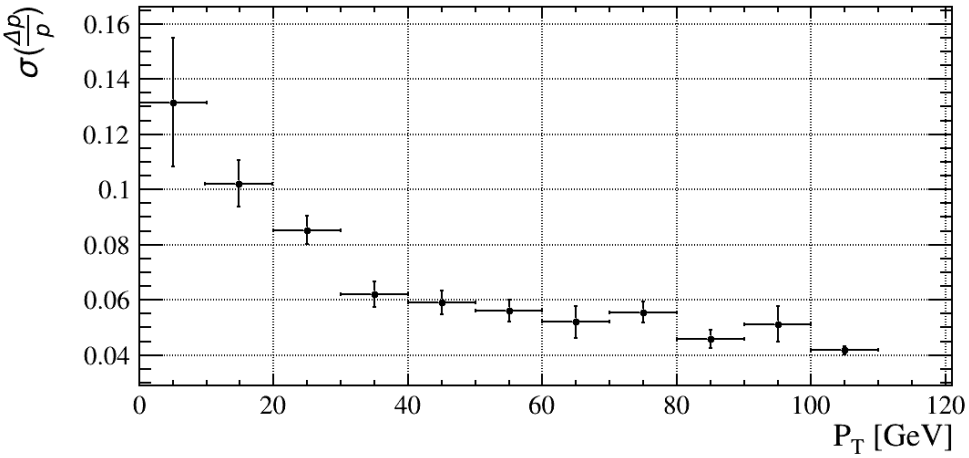

Figure 52: Jet transverse momentum resolution as a function of the jet transverse momentum.

Tracks inside the jet cone were used to identify decay vertices compatible with the decay of b quark. Indeed, since b quarks have lifetime $\tau \sim 1.5$ ps, they travel for an average distance d inside the detector $< d >= \gamma c t \beta$ where c is the speed of light, $\beta = \frac{v}{c}$ where v is the particle velocity, and $\gamma = \frac{1}{\sqrt{1-\beta^2}}$ is the Lorentz factor. In the case of 1.5 TeV $< d >$ is 8.3 mm.

The algorithm performs the following steps for each reconstructed jet:

1. tracks inside the cone with $p_T > 500$ GeV, impact parameter with respect to the $\mu^+\mu^-$interaction point greater than 0.04 cm and with a minimum number of 4 hits are selected.

2. Two tracks vertices are built, by requiring the distance of closest approach between tracks to be less than 0.02 cm, and the total transverse momentum greater than 2 GeV.

3. Three tracks vertices are built by selecting two tracks vertices with one track in common.

4. A jet is tagged as a b jet if at least one three tracks vertex is found.

The b-tagging efficiency, defined as the number of tagged and reconstructed b-jets divided by the total number of reconstructed b-jets, is presented in Figure 53. It can be seen that the it varies from about 40% to about 60% at high jet p_T. The relative low efficiency is due to the tight cuts and requirements needed to keep mis-tag as low as possible. The algorithm will be optimized in the future. The mis-tag rate, defined as the number of non b jets identified as b jets is studied in detail. The beam-induced background can create fake secondary vertex inside jet cones. The ratio between the number of cones with at least one fake secondary vertex respect to the total number of cones is taken as mis-identification rate and is estimated to be $\sim 1\%$. As mentioned in section 3.4 the beam-induced background level decreases as the center of mass energy increases, then at $\sqrt{s} = 3$ TeV the mis-tag is expected to be lower.

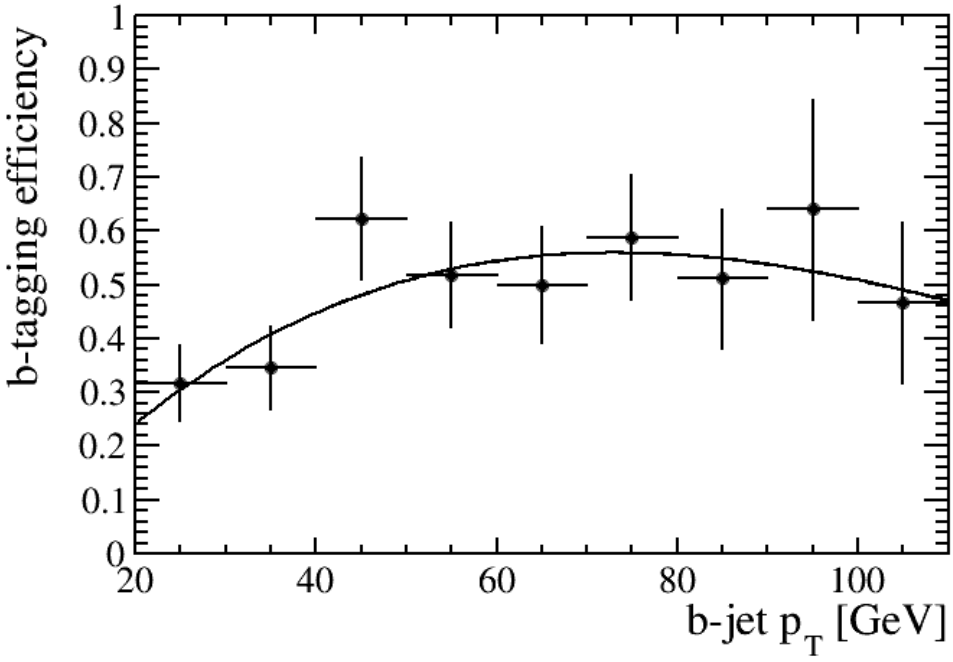

Figure 53: b-tagging efficiency as a function of the P_T.

7 Double Higgs Boson reconstruction in $b\bar{b}b\bar{b}$

As mentioned in section 2.2.2, the trilinear Higgs coupling can be obtained directly from the measurement of the cross section of double Higgs production, once it is known with sufficient precision. The purpose of this chapter is to estimate the statistical uncertainty on the measurement of the double Higgs production cross section with the Higgs decaying into a $b\ \bar{b}$ pair, with muon collisions at $\sqrt{s} = 3$ TeV center of mass energy. The analysis strategy is the following:

- the signal and physics background events are generated and studied with the full detector simulation.
- selection requirements are applied to the reconstructed events.
- observable quantities are given in inputs to a Multivariate Analysis method to separate signal from background.
- the sensitivity on the cross section is calculated. The number of the expected events $\mu^+\mu^- \to HH\nu_\mu\bar{\nu_\mu} \to b\bar{b}b\bar{b}\nu_\mu\bar{\nu_\mu}$ is given by the formula:

$$S = \sigma \cdot \mathcal{L} \cdot t \cdot \epsilon_{sel} \tag{7.1}$$

  where σ is the cross section of the $\mu^+\mu^- \to HH\nu_\mu\bar{\nu_\mu} \to b\bar{b}b\bar{b}\nu_\mu\bar{\nu_\mu}$ process at $\sqrt{s} = 3$ TeV, $\mathcal{L}$ is the instantaneous luminosity, t is the data-taking time, ϵ_{sel} is the selection efficiency.

  The statistical uncertainty on the cross section is calculated as the inverse of the significance, defined as $\frac{S}{\sqrt{S+B}}$, under the assumption that $\mathcal{L}$, t and ϵ_{sel} have no error:

$$\frac{\Delta\sigma}{\sigma} = \frac{\sqrt{S+B}}{S} \tag{7.2}$$

  where B is the number of the expected background events. This formula is commonly used in counting experiments, in which the error associated to the number of events is Poissonian [2].

7.1 Signal and background events generation

The decay channel $H \to b\bar{b}$ is used because, as mentioned in Section 2.1.2, it has the largest branching ratio and consequently is the channel with higher statistics. In this analysis jets in the final state will be required to be tagged and tagging efficiencies reported in section 6.7 will be used. Since the mis-tag efficiency is found to be low, the background coming from light quarks is assumed to be negligible. The main physics background contribution comes from processes with four b jets in the final state and two neutrinos ($\mu^+\mu^- \to b\bar{b}b\bar{b}\nu\bar{\nu}$): it comprises multiple intermediate electroweak gauge bosons and single Higgs production associated with electroweak bosons decaying into b quarks.

The signal and the physics background are generated by using WHIZARD program [70]. PYTHIA was used to simulate the parton showering, hadronization and fragmentation of hadrons. In total, 9991 double Higgs events and 8961 events of physics background are produced. The cross sections of these process, as obtained with WHIZARD at $\sqrt{s} = 3$ TeV center of mass energy are reported in Table 18. The events are then simulated by using the full detector simulation as described in previous chapters.

Processes	σ (fb)
$\mu^+\mu^- \to HH\nu_\mu\bar{\nu_\mu}$	0.84
with $H \to b\bar{b}$	0.3
$\mu^+\mu^- \to b\bar{b}b\bar{b}\nu_\mu\bar{\nu_\mu}$	6.0

Table 18: Cross sections of the signal and physics background processes at $\sqrt{s}$=3 TeV

7.1.1 Reconstruction of Higgs to $b\bar{b}$ events

The detector design and the beam-induced background simulation for a 3 TeV muon collider do not exist, then some considerations and assumptions have to be made. The detector used for this study is the one presented in section 4 and it is designed and optimized to reduce the beam-induced background at $\sqrt{s}$ = 1.5 TeV. However, as mentioned in section 3.4, the beam-induced background level decreases as the center of mass energy increases. The timing windows set for 1.5 TeV are then supposed to allow a sufficient background reduction also for the 3 TeV physics analysis. Furthermore, the optimal angles of the tungsten nozzles for the background reduction are expected to be lower at higher center of mass energy. The main effect of cones optimized for the 1.5 TeV center of mass energy on the 3 TeV physics analysis is to reduce the acceptance of the detector.

With such detector a full simulation of the $\mu^+\mu^- \to H\nu\bar{\nu} \to b\bar{b}\nu\bar{\nu}$ process at $\sqrt{s}$ = 1.5 TeV [17] including the beam-induced background was performed by using a different framework. It was found that the main effects of beam-induced background in the jet reconstruction is to create $\sim 25\%$ of fake jets, and as mentioned in section 6.7, it contributes to the mis-tag rate, that is found to be around 1% [17]. Then by applying the tagging algorithm, background due to mis-tag of fake jets and light quarks is assumed to be negligible.

In addition, the 3 TeV jet reconstruction is done on the reconstructed particles given by the Particle Flow algorithm, described in section 48, which exploits both the energy on the calorimeter and the tracks, and is tuned to give a negligible amount of fake jets [17] even in the presence of beam-induced background. Therefore, the assumption that the mis-tagged jets contribution to the background is negligible is reinforced at this energy.

7.2 Event selection

In order to increase the signal-to-noise ratio, several kinematic requirements are applied. The number of reconstructed jets per event is required to be $N_{jet} > 3$, and the minimum transverse momentum (p_T) is set to 20 GeV. Events with at least four jets are paired with the following criterion:

- The invariant mass is calculated for each jet pair:

$$m_{ij} = \sqrt{(E_i + E_j)^2 - |p_{ij}||p_{ij}|} \tag{7.3}$$

  where i,j are the indices relative to the two jets,

$$|p_{ij}| = \sqrt{(p_{i,x} + p_{j,x})^2 + (p_{i,y} + p_{j,y})^2 + (p_{i,z} + p_{j,z})^2} \tag{7.4}$$

  is the module of the vectors sum of the jets momenta and $E_{i(j)}$ is the energy of the i-th(j-th) jet.

- Among all the calculated invariant masses, the two jets pairs (i,j) and (k,l) that minimize the following relation:

$$\sqrt{(m_{ij} - m_H)^2 + (m_{kl} - m_H)^2}$$

with $m_H = 125$ GeV are selected.

After these cuts, the 66% of signal events and the 82% of background events are removed.

7.2.1 Study of the Kinematic properties

In order to select signal events, a multivariate data analysis method is used, the Boosted Decision Tree. The choice of the input variables has been done by looking at the more discriminating ones that are described here.

- The invariant mass of the two pairs of jets M_{H1} and M_{H2}, calculated in 7.3. M_{H1} is the invariant mass relative to the pair of jets with highest transverse momentum, while M_{H2} is the one relative to the other pair. In Figure 54 and 55 the invariant mass distributions of the signal (black) and the background (red) are presented. It is interesting to notice that while in the signal a single peak is evident at 125 GeV, for the background a peak at 80-90 GeV can be noticed, relative to the electroweak bosons.
- The sum of the energies of the four jets, whose distributions are represented in Figure 56
- The module of the vector sum of the four jets momenta, whose distributions is displayed in Figure 57.
- The angle between each jet pair is calculated for any four jets combination and the maximum angle is chosen. The distribution for the signal and background is represented in Figure 58.

These variables are chosen from a larger set, but the ones that do not help to improve the MVA performance are not used.

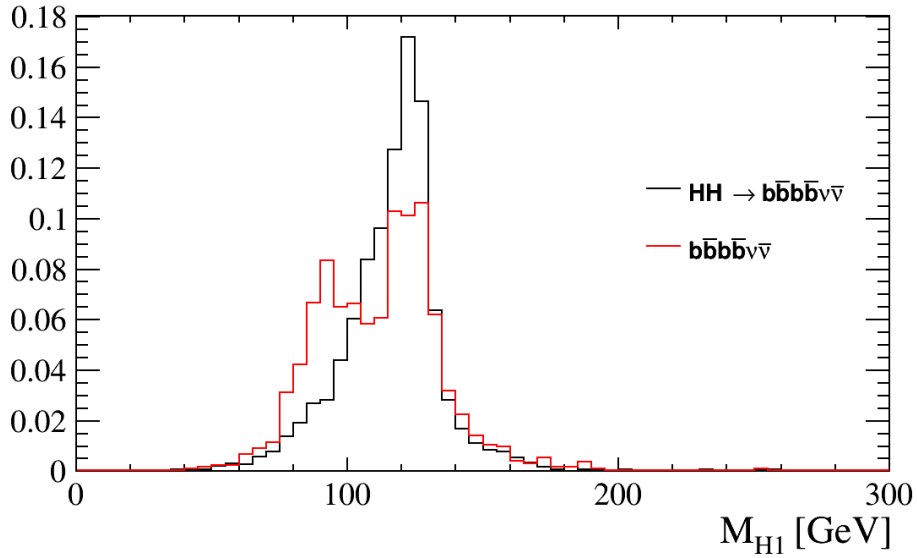

Figure 54: Invariant mass distribution of the jet pair with highest $|p_T|$ for the signal (black) and the background (red) events. The distributions are normalized to the unity area.

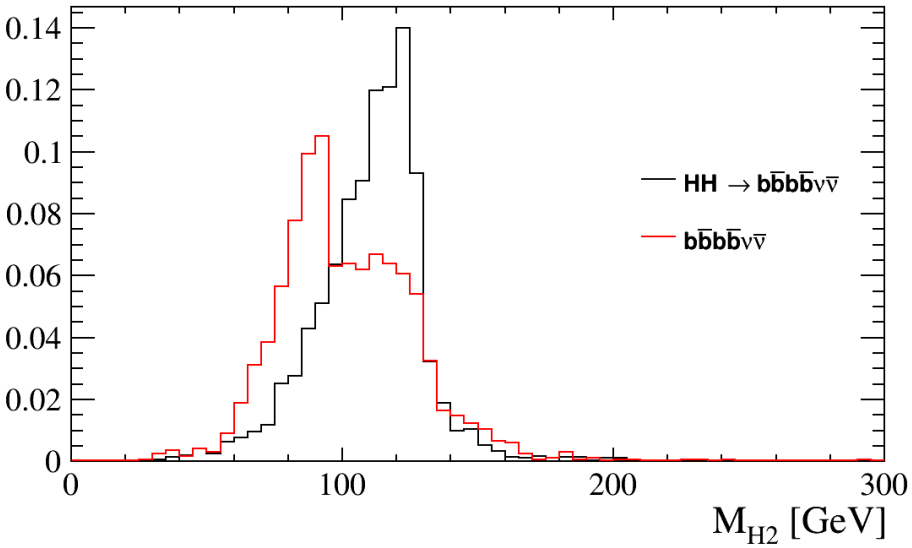

Figure 55: Invariant mass distribution of the jet pair with lower $|p_T|$ for the signal (black) and the background (red) events. The distributions are normalized to the unity area.

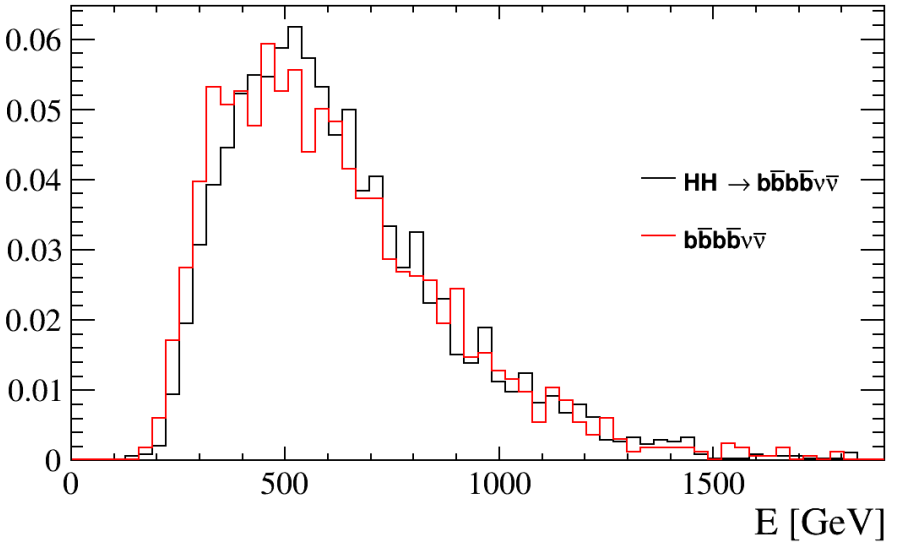

Figure 56: Distribution of the total energy of the four jets, for the signal (black) and the background (red) events. The distributions are normalized to the unity area.

7.3 Multivariate analysis and Boosted Decision Tree

The Toolkit for Multivariate Data Analysis (TMVA) [71] is a package that provides a machine learning environment in ROOT. In this physics analysis, multivariate analysis (MVA) based on a Boosted Decision tree [72] [73] is used to classify candidate events into two classes: the signal class and the background class.

Each event is characterized by a set of variables called *features variables*, that have different distributions for the signal and the background. In general a MVA classification with a supervised learning method as the BDT, consists of:

- The training of the model on a sample of data. In this step features variables relative to signal

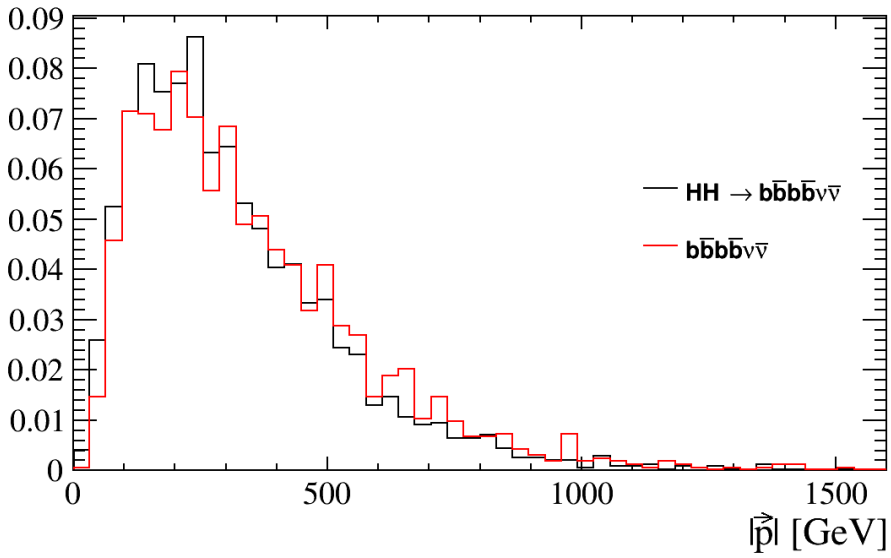

Figure 57: Distributions of the module of the vector sum of the momenta of the four selected jets, for the signal (black) and the background (red) events. The distributions are normalized to the unity area.

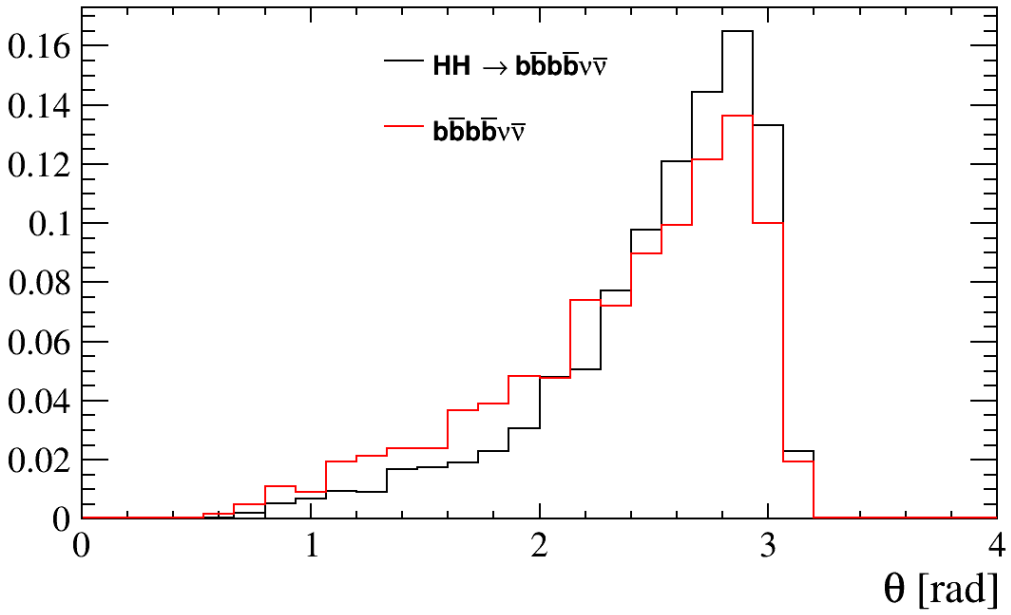

Figure 58: Distributions of the maximum angle for signal (black) and background (red) events. The distributions are normalized to the unity area.

and background events are given as input to the model. On the basis of their distributions the model will tune its parameters in order to learn how to efficiently distinguish events into the two categories. This will be explained in detail in Section 7.4.

- The test of the model on a sample of data different from the one used in the training step, in order to evaluate its performance.

In the next sections 7.4 and 7.4.1, the building blocks of a boosted decision tree are introduced.

7.4 The Decision Tree

A decision tree is a binary tree structured classifier (see Figure 59). The event classification with decision trees consists of applying a set of *cuts* (called c_n in Figure 59) on the features variables (labeled as x_i, x_j, x_k in Figure 59) that are optimized in the training phase in order to maximize signal-background separation. It starts from an initial node, the root node that splits into two branches, until a stopping condition is reached. The end nodes contain signal or background events. If there are more signal than background events in an end node it is labeled as a signal-like end node. The opposite is labeled as background-like end-node.

A decision tree algorithm in the training phase proceeds as follows:

1. A sample of signal s_i and background b_j events, described by feature variables x_k are given in input to the node;
2. If the stopping criterion is satisfied, the node is declared as terminal and exit the algorithm;
3. Values of each variable $\vec{x}$ are sorted;
4. For each variable, the splitting value that allows the best separation between signal and background is found;
5. The variables and splitting values that determine the best separation are fixed, and the node is split into two other nodes. One will contain events that pass the cut, the other one events that does not pass the cut;
6. Previous steps are repeated in a iterative way.

The stopping conditions for the decision tree growth, mentioned in step 2, used in this analysis are the default in TMVA, and are:

- Maximum depth of the tree (that is the maximum number of layers of nodes) set as 3;
- Minimum percentage of training events required in a end node of 2.5%.

The best separation between signal and background is determined by minimizing the Gini index [72] [74], that for a two-class classification is:

$$G = 2p(1-p)$$

where p is the purity, defined as $p = \frac{s}{s+b}$, where s and b are the signal and background counts at each step in the process. In the training procedure variables and cut values that optimises the increase in the Gini index between the parent node and the sum of the indices of the two daughter nodes, weighted by their relative fraction of events are selected.

In the case of boosted decision tree, as will be shown in the next section 7.4.1, s and b are calculated as the sum of the weights associated to the event:

$s = \sum_i w_{i,s}$ and $b = \sum_j w_{j,b}$

where $w_{i,s}$ is the weight associated to the signal event i-th in the branch, and $w_{j,b}$ is the weight associated to the background event j-th in the branch.

7.4.1 Boosted Decision Tree

The boosting of a decision tree extends the concepts explained for a single tree to several trees which form a forest. The idea behind boosting is to create a set of trees that take in input the same training sample, but with weighted events, such that the optimization of the BDT parameters focuses on events that are not classified correctly. The boosting procedure used in this analysis is

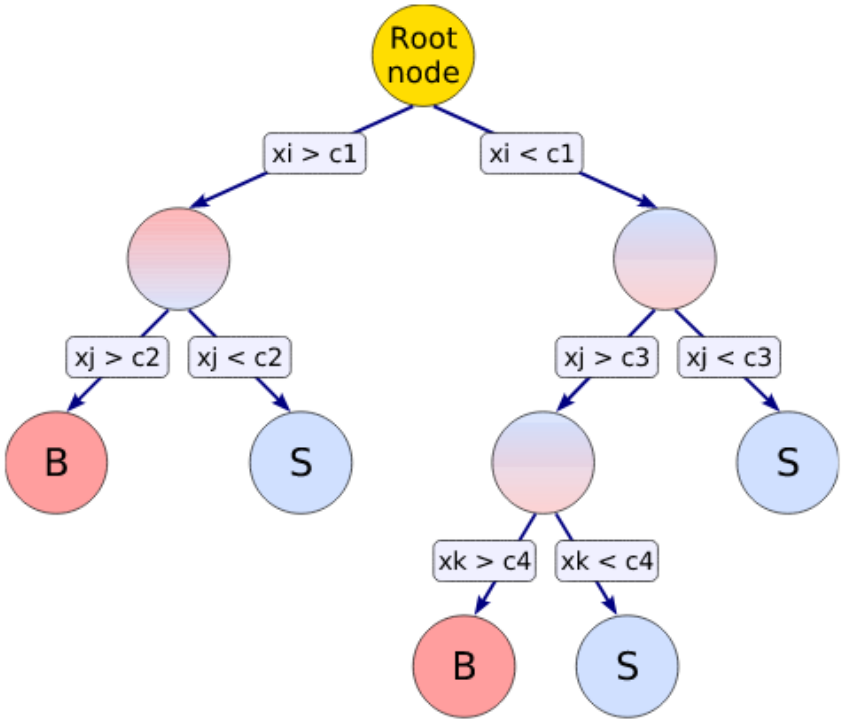

Figure 59: Scheme of a Decision Tree. It starts from a Root Node that splits into branches by applying cuts c_n on the input variables x_i, x_j, x_k relative to the signal (S) and background (B) samples. The ending nodes are classified as S if the number of signal exceed the background, B otherwise.

called adaptive boosting [75] and the steps of the algorithm are now described. Let N be the total number of events given in input to the BDT, and M the number of trees created in the boosting procedure, y_i^m the variable that states if the i-th event ($i = 1, .., N$) is mis-classified or not in the m-th tree ($i = 1, .., M$). Let's take y_i^m= 1 if correctly classified and y_i^m=0 if mis-classified. Let's call w_i^m the weight associated to the i-th event in the m-th tree. The algorithm proceeds as following:

- In the first tree the event weight is initialized to $w = 1/N$ for every event.
- M iterations are performed. In the iteration m, the m-th tree is created and takes in input the weighted samples obtained from the $(m-1)$-th iteration.
- The m-th error function e_m, that calculate the mis-identification rate is calculated:

$$e_m = \frac{\sum_{i=1}^{N} w_i^{m-1} y_i^m}{\sum_{i=1}^{N} w_i^{m-1}}$$

- The mis-identification rate is used to calculate the m-th tree weight, let's call it α_m:

$$\alpha_m = \frac{1 - e_m}{e_m}$$

- The i-th event weight in m-th tree is then changed:

$$w_i^m = w_i^{m-1}(\alpha_m y_i^m)$$

  In this last step it can be seen how weights that are correctly classified remain unchanged from the m-th tree to the $(m+1)$-th tree, while weights for mis-classified events are increased

by a factor α_m. The $(m+1)$-th tree will then have in input a training sample with higher weights for mis-classified events. The weights of the entire event sample are then normalised such that the sum of weights remains constant.

Let's call the output of the classification of the x_i event in the m-th tree as $T_m(x_i)$. It will be 1 if the event will be classified as a signal event (it will ends in a signal like leaf), while -1 if it will be classified as a background event. The final output of a BDT, at the end of the boosting procedure, for the event x_i is a weighted response of each individual tree in the collection.

$$T(x_i) = \frac{1}{M} \sum_{m=1}^{M} ln(\alpha_m) T_m(x_i)$$

As can be seen, the output of all the trees in the boosting procedure are taken into account. The number of trees that are built in the boosting procedure can be set in TMVA. In the following analysis the default value is kept and is 850. The number of trees and the depth of a tree, are important parameter in a BDT: previous studies on BDTs show that the best result is usually achieved by using many small trees [73].

7.5 Event Classification

The signal and background events kinematic distributions presented in the previous Section 7.2.1 are given as input to the BDT. The full sample of signal and background events is split randomly in two. Half of the samples are used as training sample to the BDT, while the others are used as test sample. In Figure 60 the linear correlation coefficients between variables are shown in percentage. Coefficient close to 100% means that two variables are highly correlated, then do not add information in the training of the BDT. In this case, all correlation coefficients are below 64%.

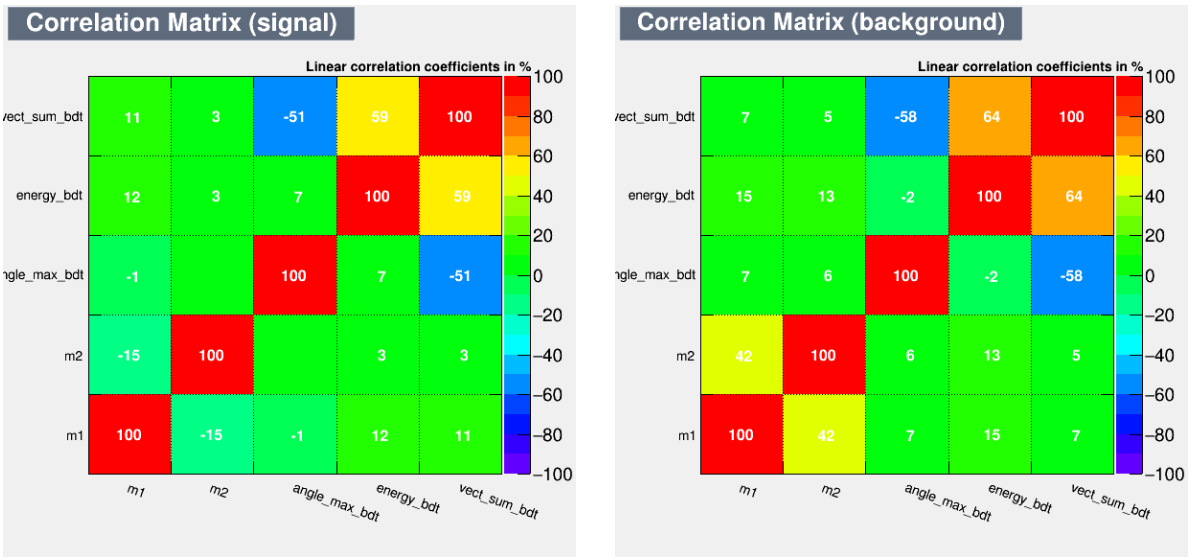

Figure 60: Left: signal correlation matrix among BDT input variables. Right: background correlation matrix among BDT input variables.

7.5.1 Boosted Decision Tree evaluation

A boosted decision tree can overtrain due to the large number of nodes. Overtraining occurs when too many parameters of the algorithms are adjusted to classify a data sample with few events,

leading to a low mis-classification error in the training procedure, but they are not optimal for the testing sample. A convenient way to detect overtraining is to compare the distributions of the classifier output on the training and test sample, each for signal and background. The Kolmogorov-Smirnov test (KS) [74] is used in TMVA to measures the probability that the distributions of the BDT output for the training and test samples are similar. It consists on the calculation of the maximum distance between their cumulative distribution functions. By calling $F(x)$ and $G(x)$ the two cumulative distribution functions of the two distributions of the variable x, they are calculated as:

$$F(x) = \frac{1}{n} \sum_{i=1}^{n} I_{[-\inf,x](x_i)}$$

where n is the total number of x_i and $I_{[-\inf,x](X_i)}$ is equal to one if $x_i < x$ and zero otherwise. The test statistic is given by the maximum distance between two cumulative distributions:

$$D_{KS} = max|F(x_i) - G(x_i)|$$

TMVA returns the p-value of the Kolmogorov-Smirnov test.

The performance of the BDT on the classification of the test sample can be evaluated by mean of the *Receiver Operating Characteristic (ROC)* curve. It shows the signal efficiency as a function of the background rejection. As stated before, in the BDT distribution a different score is given to each event. If a certain value on the BDT output axis is chosen as threshold, the events on its right will be considered as signal and all the ones on the left will be background. To build the ROC curve the following quantities have to be defined:

- background events with BDT output above the threshold are called False Positive (FP);
- bignal events with BDT output above the threshold are called True Positive (TP);
- bignal events with BDT output below the threshold are called False Negative (FN);
- background events with BDT output below the threshold are called True Negative (TN).

True positive rate ϵ_{signal} (signal efficiency) versus the false positive rate $\epsilon_{background}$ (background rejection) for the threshold are then calculated as:

$$\epsilon_{signal} = \frac{TP}{TP + FN}$$

$$\epsilon_{background} = \frac{FP}{TN + FP}$$

By varying the threshold, different number of TP,FN,FP and TN events are selected, and the ROC curve is obtained. In Figure 61 [76] some examples of ROC curves for a given classifier are given, for different distributions of BDT outputs. If the BDT is a good classifier (i.e. the signal and background distributions are more separated) the area under the curve is bigger and the curve is on the top-right of the signal efficiency-background rejection plot.

By calculating the area under the ROC curve (AUC), different classifiers can be compared [74]. If two pairs of events are selected, one from the signal and one for the background, the AUC curve is the probability that a classifier gives a larger classification score to the signal event. Then, the larger the area under the curve (called AUC), the better is the separation of signal from background that can be achieved.

The BDT is trained on signal and background samples in order to determine the parameters that give the best separation between the signal and background events. The overtraining test

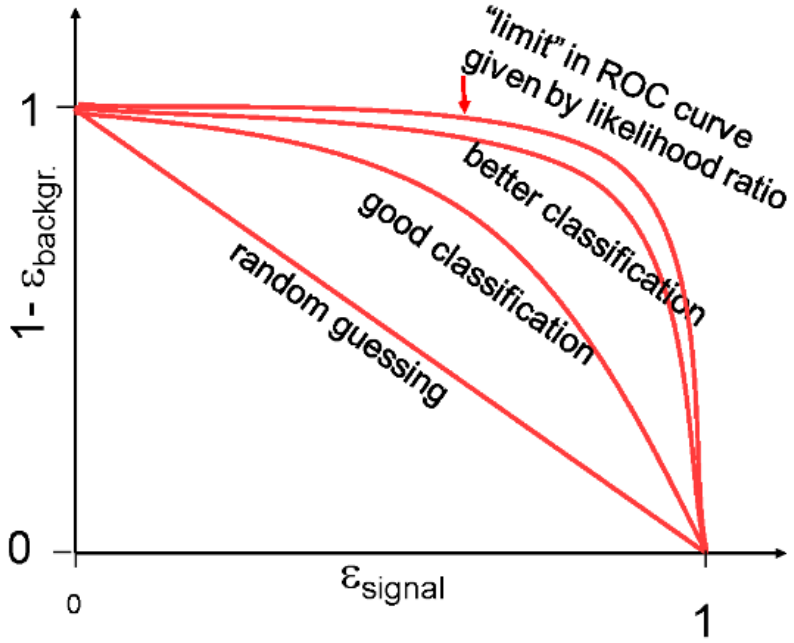

Figure 61: Examples of ROC curve shapes. If the chosen method is a good classifier, the area under the ROC curve is close to 1. If the area is close to 0.5, the method classifies events randomly.

is done separately for the signal and the background samples, as shown in Figure 62. Here the distributions of the BDT output for the training and test samples are compared. It can be seen that the training distributions are not fully compatible with the test distributions. This is confirmed by the Kolmogorov-Smirnov test discussed in section 7.5.1, that in this case gives a zero p-value both for the signal and the background.

In Figure 63 the ROC curve is shown for different classification methods used with TMVA. As explained in section 7.5.1, a better classification is obtained for large AUC values in the ROC curve. In this case it can be seen that the BDT gives the best separation with an AUC value of 0.705.

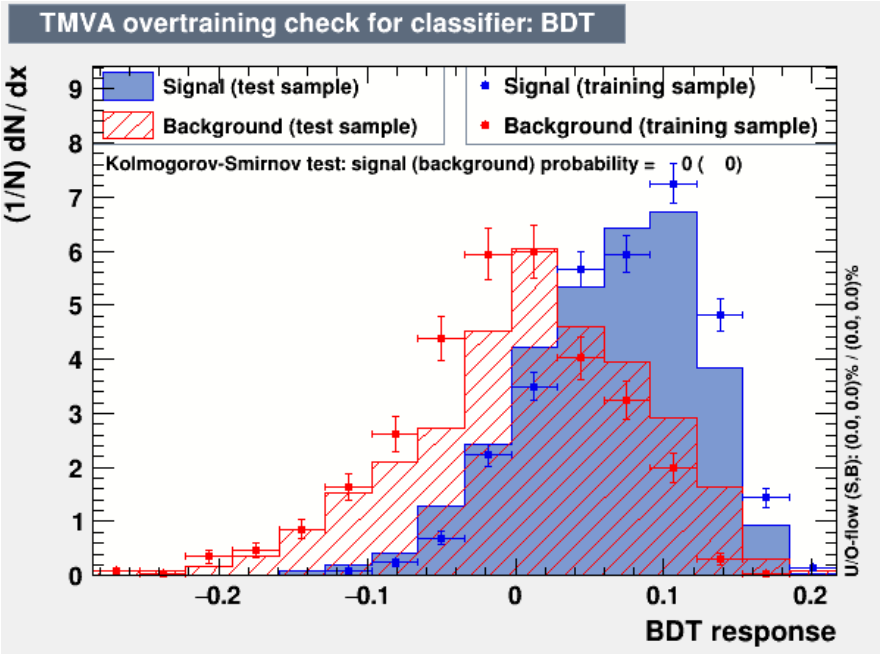

Figure 62: Overtraining check for the BDT classifier. Points are used for BDT output on the training sample, histograms are used for the test samples. The shapes of the training and test samples distributions are compared for the signal (blue) and the background (red) events.

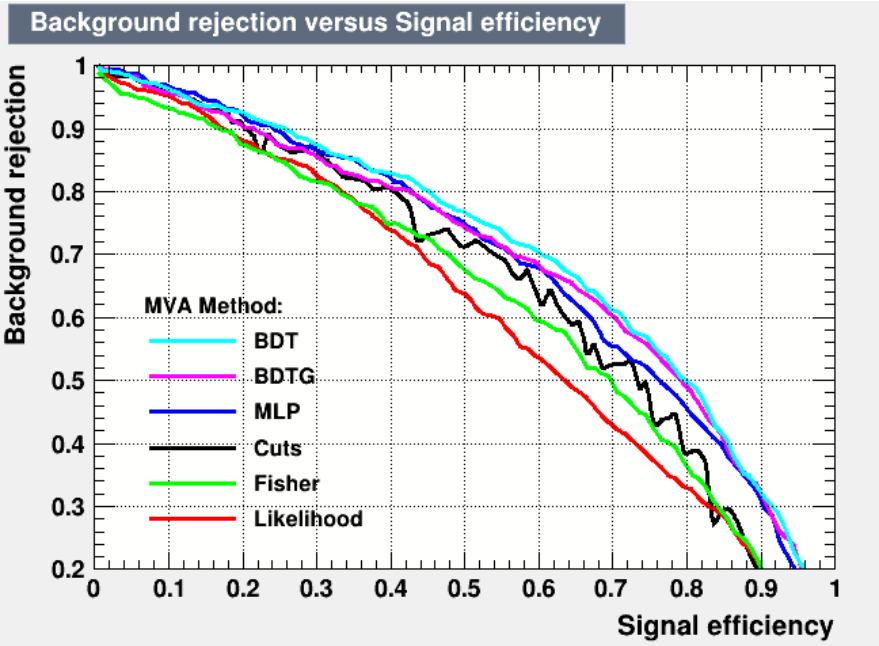

Figure 63: Receiver operating characteristic (ROC) for different MVA methods: BDT with gradient boost (BDTG) Multilayer Perceptron (MLP), Cut optimisation, Fisher discriminant and Likelihood

7.5.2 Cross Checks

Due to the limited number of available events, the final BDT classification is performed on the totality of events used for the training and the test. The re-use of training data can introduce bias on the final distribution of the BDT output. In order to check that the output distribution does not depend on any data sub-sample, two sub-samples of signal and background events are randomly selected from the total number of events, and are classified with the BDT. The output distributions are shown in Figure 64 for the signal and in Figure 65 for the background with the respective statistical errors. Qualitatively the two distributions are compatible. In the future more rigorous checks have to be done, by using for example k-fold cross validation [73].

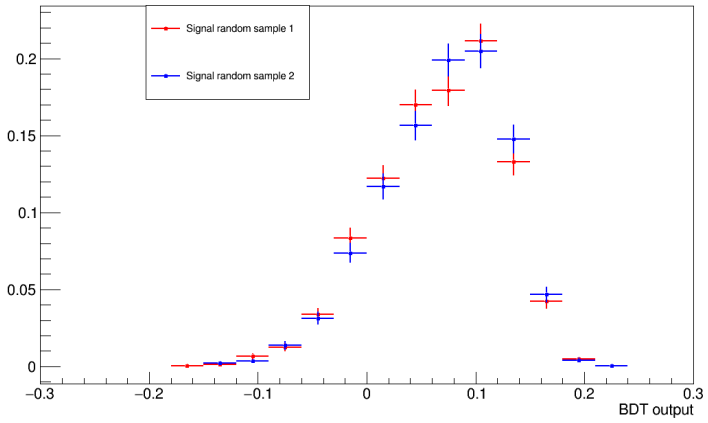

Figure 64: Output distributions of the BDT for two randomly selected signal sub-samples. Statistic error bars are reported to show qualitatively the compatibility between the two shapes.

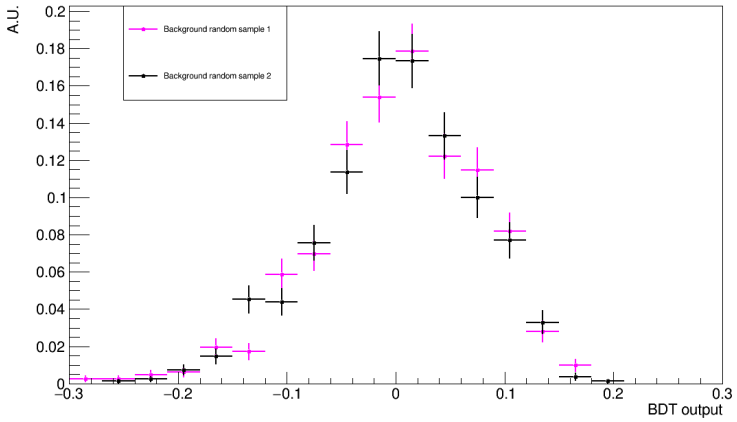

Figure 65: Output distributions of the BDT for two randomly selected background sub-samples. Statistic error bars are reported to show qualitatively the compatibility between the two shapes.

7.5.3 BDT output

The entire dataset of signal and background events is given in input to the BDT. The outputs are shown in Figure 66. In red is displayed the distribution of the background events, while in blue the one of the signal events. In order to determine the significance on the HH cross section, a cut on the BDT output distributions is applied. The cut is optimized by maximizing the significance as discussed in section 7.6.

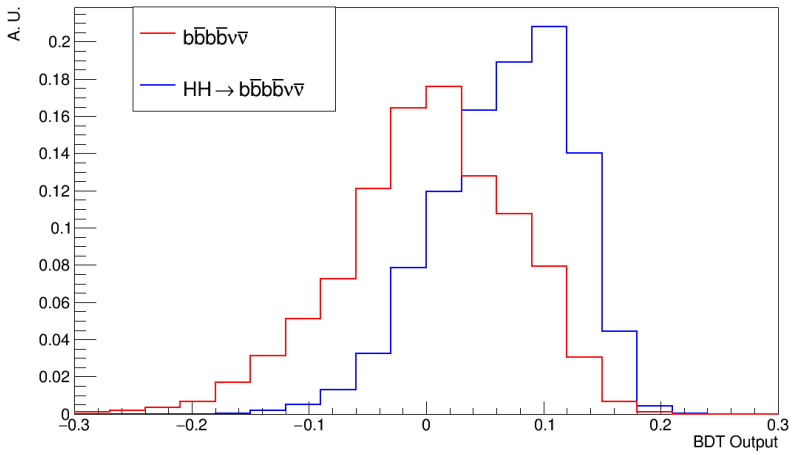

Figure 66: Output distributions of the BDT for the signal (blue) and background (red) samples.

7.6 Determination of the HH cross section precision

In order to determine if a jet is b-tagged, a weight procedure is applied. For each pair of jets, it is required that at least one is tagged by weighting it by using the b tagging efficiencies as function of jet p_T determined in Section 6.7

Let's define: ϵ_1 and ϵ_2 the probability to tag respectively the first and the second jet in the first pair, and ϵ_3 and ϵ_4 the probability to tag, respectively, the first and the second jet in the second pair. Then it can be observed that:

- the probability of do not tag any jet in the first pair is $(1-\epsilon_1)(1-\epsilon_2)$ (same for the second pair with the proper indices);
- the probability of tag at least one jet in the first pair is $(1-(1-\epsilon_1)(1-\epsilon_2))$ (same for the second pair with the proper indices);
- The probability to tag at least one jet in each pair in the event is then:

$$w = (1-(1-\epsilon_1)(1-\epsilon_2))(1-(1-\epsilon_3)(1-\epsilon_4)). \tag{7.5}$$

The w function is used to weight each event that survive the preliminary selection.

In order to calculate uncertainty on the cross section by using equation 7.2, the number of signal and background events after the weight procedure are needed. They are for signal:

$$S_w = \sigma_{HH\nu_\mu\bar{\nu_\mu}\to b\bar{b}b\bar{b}\nu_\mu\bar{\nu_\mu}} \cdot BR(H\to b\bar{b})^2 \cdot \mathcal{L} \cdot t \cdot \epsilon_S. \tag{7.6}$$

Where:

- $\sigma_{\mu^+\mu^-}$ is the cross section of the double Higgs production and $BR(H \to b\bar{b})$ is the branching ratio of Higgs to $b\bar{b}$ quarks;
- $\mathcal{L}$, the instantaneous luminosity, taken for 3 TeV center of mass energy from [11] equal to $4.4 \cdot 10^{34}$ cm^{-2} s^{-1};
- t, the period of time considered, assumed to be $4 \cdot 10^7$ s;
- $$\epsilon_S = \frac{N_{sel,S}}{N_{tot,S}}$$

  $N_{sel,S}$ is the number of signal events that pass the preliminary requirements and after the BDT output cut, weighted as explained. $N_{tot,S}$ is the initial number of signal events.

While the number of background events is given by:

$$B_w = \sigma_{b\bar{b}b\bar{b}\nu\bar{\nu}} \cdot \mathcal{L} \cdot t \cdot \epsilon_B. \tag{7.7}$$

Where:

- $\sigma_{b\bar{b}b\bar{b}\nu\bar{\nu}}$ is the inclusive $b\bar{b}$ production cross section;
- $$\epsilon_B = \frac{N_{sel,B}}{N_{tot,B}}$$

  $N_{sel,B}$ is the number of background events that survive the preliminary requirements, after the BDT output cut and weighted with the described procedure. $N_{tot,B}$ is the initial background events number.

The results of S_w and B_w for different cuts on the BDT output are reported in Table 19. Therefore, the best uncertainty on the cross section is:

BDT_{Cut}	S_w	B_w	Significance	$\frac{\Delta\sigma}{\sigma}$
-0.06	67	618	2.52	0.40
-0.03	64	528	2.62	0.38
0	59	405	2.74	0.37
0.03	51	273	2.84	0.35
0.06	41	178	2.74	0.36
0.09	28	93	2.52	0.40
0.12	13	30	2.01	0.50

Table 19: BDT_{cut} is the threshold chosen for the cut. S_w (B_w) are the number of signal (background) events surviving the cuts on the BDT, weighted for the b-tagging efficiencies. In red is highlighted the best significance and the smaller error on the production cross section determination.

$$\frac{\Delta\sigma}{\sigma} = \frac{\sqrt{S_w + B_w}}{S_w} = 35\%$$

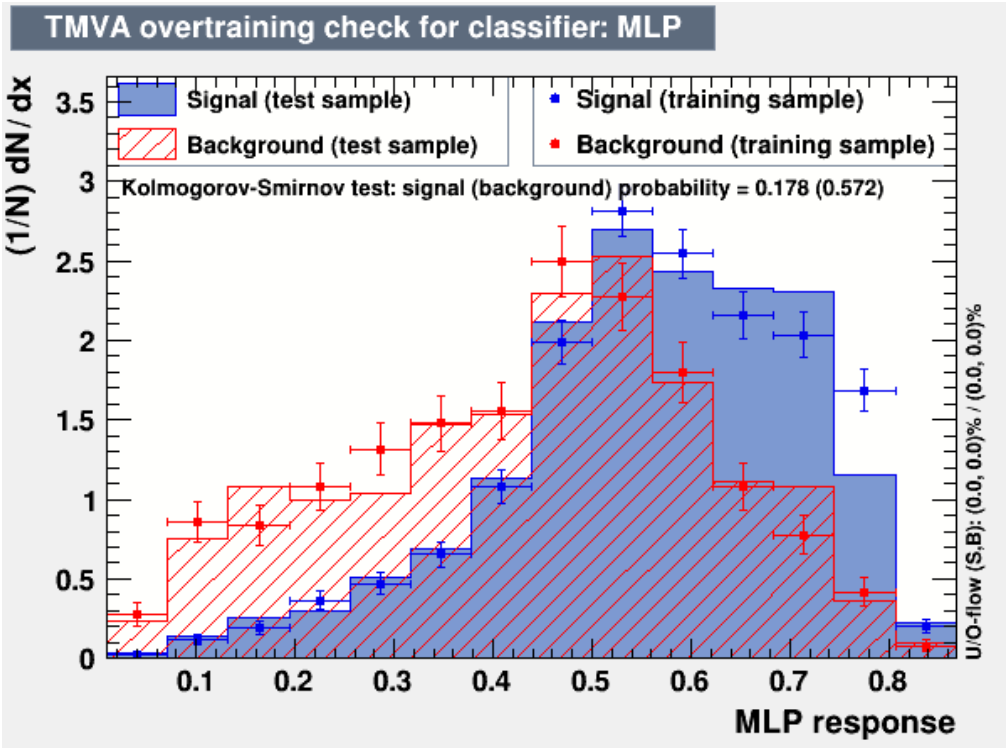

Figure 67: Overtraining plot for the Multi-Layer Perceptron method. Training and test distributions are compared for the signal (blue) and the background (red)

7.7 Future Developments

The presented results obtained for the first time by exploiting muon collisions, will be improved in the next year. The signal to background separation can be improved. As mentioned in section 7.5.1 the main problems of the used method are the overtraining and the low area under the ROC curve. Studies to improve BDT performance are already in progress: new sets of variables will be used for the event classification and different setup of the BDT settings will be investigated by varying the number of tree and the number of nodes.

Alternatively, other multivariate techniques can be evaluated. A first attempt has been already made by training a Multi-Layer Perceptron (MLP) method with TMVA. The input variables given for the training of the method are the one presented in section 7.2.1. As shown in Figure 67 the overtraining is lower respect to BDT, but the AUC is 0.686. The output of the MLP on the full sample of events is reported in Figure 68.

The study described above to arrive to the determination of the error on the cross section, has been repeated by using the MLP discriminant. The iterative procedure to define the best cut on the MLP output gives as results the numbers summarised in Table 20. The best estimate of the uncertainty on the cross section is 39%. This number is very similar to the one obtained with the BDT method, if it is taken into account that no systematic error is considered.

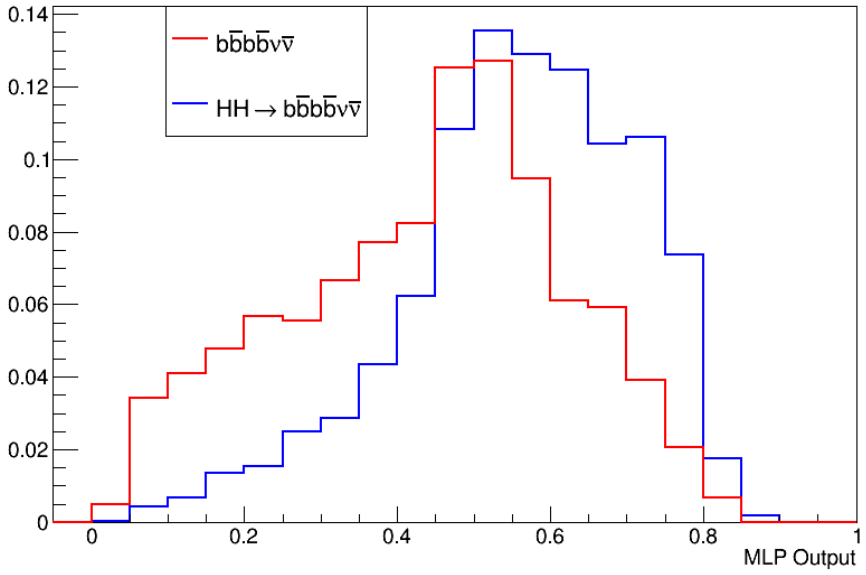

Figure 68: Output of the Multi-layer perceptron method classification for the signal (red) and background (blue) events.

MLP_{Cut}	S_w	B_w	Significance	$\frac{\Delta\sigma}{\sigma}$
0.01	67	725	2.38	0.42
0.02	66	663	2.43	0.41
0.03	63	580	2.49	0.40
0.04	58	472	2.54	0.39
0.05	47	316	2.48	0.40
0.06	30	147	2.23	0.45
0.07	14	53	1.71	0.59

Table 20: MLP_{cut} is the value chosen to cut on MLP output. S_w (B_w) are the number of signal (background) events surviving that cut, weighted for the b-tagging efficiencies. In red is highlighted the best uncertainty on the cross section achievable.

8 Conclusions

This thesis faces, for the first time, the study of the performance of the reconstruction of $\mu^+\mu^- \to HH\nu\bar{\nu} \to b\bar{b}b\bar{b}\nu\bar{\nu}$ at $\sqrt{s} = 3$ TeV with the full detector simulation. In order to obtain that the signal, double Higgs events, the physics background, events with 4 b-jets in the final state, and the beam-induced background have been simulated and reconstructed.

The effects of the beam-induced background particles on detector components have been studied in detail for a muon collider at 1.5 TeV center of mass energy. The design of the detector was optimized for that $\sqrt{s}$ and it has been implemented in the ILCSoftware framework to study the physics object reconstruction performance.

The high occupancy in the tracker system, especially on the first layers close to the beam pipe, can be mitigated with a timing cut. However the presence of a very high number of hits affects the reconstruction of low $p_T < 1$ GeV tracks. A tracking system designed to cope with these characteristics is needed together with a different tracking strategy.

The studies presented in the thesis show that the effects of beam-induced background on the calorimeter are much less severe. With a no optimized algorithm, the reconstruction efficiency is greater of 80% for jets with transverse momentum higher than 20 GeV. The jet tagging used is elementary, cut-based. Improvements in jet finding and b-tagging are foreseen as one the major leap forward in the measurements.

The analysis has been conducted starting from the events generation up to the evaluation of error on the cross section. The tools used are common in high energy physics. A multivariate technique based on Boosted Decision Tree is used to classify the signal and background events. The uncertainty on the cross section, for an integrated luminosity of $L = 1300$ fb $^{-1}$ collected in four years at the nominal instantaneous luminosity, is found to be $\frac{\Delta\sigma}{\sigma} = 35\%$. This is the first evaluation of the error on the double Higgs production cross section in muon collision at center of mass energy of 3 TeV. Given the improvements that are possible and have been described in this thesis, this error can be largely reduced. Nevertheless, the precision obtained is already comparable with that achieved by CLIC, in particular if normalized to the data taking time and considering that this is the first evaluation. This work constitutes the foundation for the determination of the trilinear Higgs self-coupling.

A Conformal Tracking

The Conformal Tracking [56] is a pattern recognition technique for track finding that combines the two concepts of conformal mapping and cellular automata.

A.1 Cellular automata algorithms

Full tracks are created by the CA algorithm [59] in several steps:

Building of cellular tracks candidates
Hits surviving the timing windows fixed in Section 5.2 are used as input to the tracking techniques. In this first step, the hit collection relative to the first layer of the vertex detector is taken as input and all hits are considered the starting point of a cellular track candidate (they are called *seed hits*). Cellular tracks are built by chaining *cells*, that are defined as segments connecting two hits.

The building of cells is performed in the following steps [60]:

1. *seed cells* are built by connecting *seed hits* to hits belonging to layers with smaller conformal radius, that satisfy the following criteria:
   - lay within a window of polar angle in the conformal space ($\Theta = arctan(\frac{u}{v}) + \pi$) fixed to $\Delta\Theta_{neigh} = 0.05$ rad
   - are not already part of a track
2. Seed cells with a length bigger than l_{max} are discarded
3. Seed cells are then prolonged in the radial direction of the conformal space: new cells of maximum length l_{max} are created and chained
4. New cells that form an angle larger than α_{max} with respect to the seed cell are discarded
5. A *weight* is associated to each cell, that is much higher when a cell can potentially be linked to more cells.

Cellular tracks are created from the building cells starting from the highest weighted seed cell. A minimum number of hits for each candidate is also required (N_{min}^{hits}). The candidates are then fitted with a linear regression to obtain the parameters in Equation 6.1.1 and cellular tracks are selected:

1. The linear regression fit is performed twice, both in the conformal space and on the (s, z) plane, where s is the coordinate along the helix arc segment.
2. Only the cellular tracks for which neither of the two normalised $\chi^2_{(u,v)}$ and $\chi^2_{(z,s)}$ values exceeds a threshold χ^2_{max} are considered as valid track candidates.
3. Among the all the cellular track candidates the one with the best total χ^2 and the longer length are selected.

All these steps are done for each seed hit, and at the end of the process, all hits belonging to the created cellular tracks are marked as used.

Extension of cellular track candidates
Cellular tracks are extended according to the particle transverse momentum estimated from the

linear regression fit in the (s, z) plane. Tracks with a transverse momentum above a threshold $p_{T,cut}$ are extended first. In this case the extension procedure and the best track candidate selection is similar to the case of building step:

1. end hits of the cellular tracks are used as seed hits
2. new hits at smaller conformal radius to be chained to the track candidate are searched
3. the best track candidate is chosen based on the χ^2_{tot} values from the linear regression fit in (u, v) and (s, z).

For extension of tracks with $p_T < p_{T,cut}$ a different procedure is applied, as low p_T tracks will tend to loop in the tracker due to the magnetic field. In this case the nearest neighbour search is not performed, and all unused hits are considered for track extension, provided that they are located on the same side of the detector in z with respect to the seed hit. The search for compatible hits is then done including a quadratic term in the regression formula, in order to take into account deviation from a straight line.

Step	Algorithm	Hit collection	α_{max} $[rad]$	l_{max} [mm^{-1}]	N^{hits}_{min} -	χ^2_{max} -	$p_{T,cut}$ [GeV]
1	Building	Vertex Barrel	0.005	0.02	4	100	-
2	Extension	Vertex Endcap	0.005	0.02	4	100	10
3	Building	Vertex Barrel+Endcap	0.025	0.02	4	100	-
4	Building	Vertex Barrel+Endcap	0.05	0.02	4	2000	-
5	Extension	Tracker	0.05	0.02	4	2000	1
6	Building	Vertex + Tracker	0.1	0.015	5	1000	-

Table 21: Overview of the pattern recognition steps and parameters

These two algorithms are run on all reconstructed hits in several iteration and different sets of parameters. The steps of the full pattern recognition chain are listed in Table 21.

- the cellular tracks candidates are built by using the hits in the vertex barrel as input (step 1)
- they are extended by using the hits in the vertex endcap (step 2)
- cellular track candidates are built by us ing the remaining hits in the combined vertex barrel and endcap detector, first using tighter cuts (step 3) and looser cuts afterwards (step 4)
- all cellular track candidates are extended to the tracker detectors (step 5)
- In the last step the remaining hits on both the vertex and the tracker detectors are used to reconstruct remaining tracks most of which are generated by displaced particles. During this step the CA algorithm is run from the outermost layer of the tracker back to the innermost layer of the vertex detector. Moreover, a quadratic term is included in the regression formula to fit the cellular track candidates in conformal space.

B Pandora Particle Flow

B.1 PandoraPFA algorithm

The PandoraPFA algorithm described in detail in [65]. In each step, the PandoraPFA default values are used and can be found in the repository [66].

1. **Track Selection/Topology**
   In this first step tracks are pojected into the front face of the electromagnetic calorimeter, using a helical fit. By studying tracks topologies, kinks or decays of neutral particles are identified. In particular, neutral particles decaying into two charged particles can be identified by searching for pairs of tracks coming from a common point, displaced from the interaction point. Kinks (charged particle decays to a single charged particles plus neutral particles) can be recognized by looking at the distance of closest approach of the parent and daughter tracks. The original track parameters, the projection of the track onto the face of the electromagnetic calorimeter and the identified topologies are given in input to the following analysis.

2. **Calorimeter Hit Selection and Ordering**
   Another collection given in input to the PandoraPFA is the list of digitized calorimeter hits containing the (x, y, z) position, the deposited energy and the layer on the electromagnetic and hadronic calorimeters. Calorimeter hits are processed by performing these steps:

   Hit selection: A minimum ionising particle (MIP) energy cut is applied to the calorimeter hits. First calorimeter hit energy is converted to a minimum ionizing particle equivalent (at normal incidence). Hits are retained if they contain more than a fraction (0.5 for the ECal and 0.3 for the HCAL) of the energy of an incident MIP particle.

   Calibration: Hits energy is corrected by mean of calibration factors that depends on the fact that calorimeter hits can be associated to an electromagnetic or hadronic particle shower. The hadronic showers produced in an hadronic calorimeter are different from the purely electromagnetic showers produced by photons and electrons in the ECAL [77], and are characterized by two distinct components:

   - An electromagnetic component: π^0 and η generated in the absorption process develop electromagnetic showers as they decay into photons
   - A non-electromagnetic component: which comprises all other processes takes place during the absorption and shower development. Almost the 40 % of this component is called invisible energy and consists of the binding energy of nucleons released in the numerous nuclear reactions or neutrinos.

   The presence of this invisible component, leads to a larger detector response for electromagnetic showers with respect to the non electromagnetic one. The HCAL hits are then reweighted by using the software compensation technique developed by the CALICE (Calorimeter for Linear Collider Experiment) collaboration [67].

   These scale factors are used in the following steps once the particle shower type is identified, otherwise, the uncorrected calorimeter hit is used.

   Isolation Requirements: calorimeter hits used in the initial cluster finding algorithm are required to have a minimum number of calorimeter hits within a fixed distance. Hits that do not satisfy this requirement are defined as isolated hits. They are mostly released by low energy neutrons produced in hadronic showers, as they can travel a significant distance from the original shower before deposit energy. These energy deposits are excluded from the initial cluster finding algorithm, as they are difficult to be associated to any particle shower.

   MIP Identification: minimum ionising tracks within the calorimeter are identified on the basis of the energy deposition on the hit and the comparison with surrounding hits on the same calorimeter layer. In particular the energy deposition must not be a number of times the

expected MIP signal and adjacent cells in the same layer. Furthermore no more than one of the adjacent hits in the same layer must be above this thershold.

Hit Ordering: before the clustering algorithm is applied, hits are ordered by energy within each layer of the calorimeters.

3. **Clustering**
   Hits are grouped into clusters using a cone-based clustering algorithm. It exploits the fact that the direction of the released calorimeter hits is almost the same of the original particle. The algorithm starts by considering as seed the hits corresponding to the projection of the reconstructed tracks onto the front face of the electromagnetic calorimeter. The track direction at the ECAL front face determines the initial direction of the cone. In the case that the calorimeter hits taken as seed are not associated to projection of tracks, the initial cone direction is taken the one from the interaction point to the calorimeter hit. A cone with a opening angle is formed around the direction of the seed as can be seen in Figure 69. Calorimeter hits are looped over on a per layer basis, starting from the innermost and going to the outermost layer. Hits that lie within cone defined by existing cluster, and are sufficiently close, are added to the cluster. Unmatched hits, are used to seed new clusters.

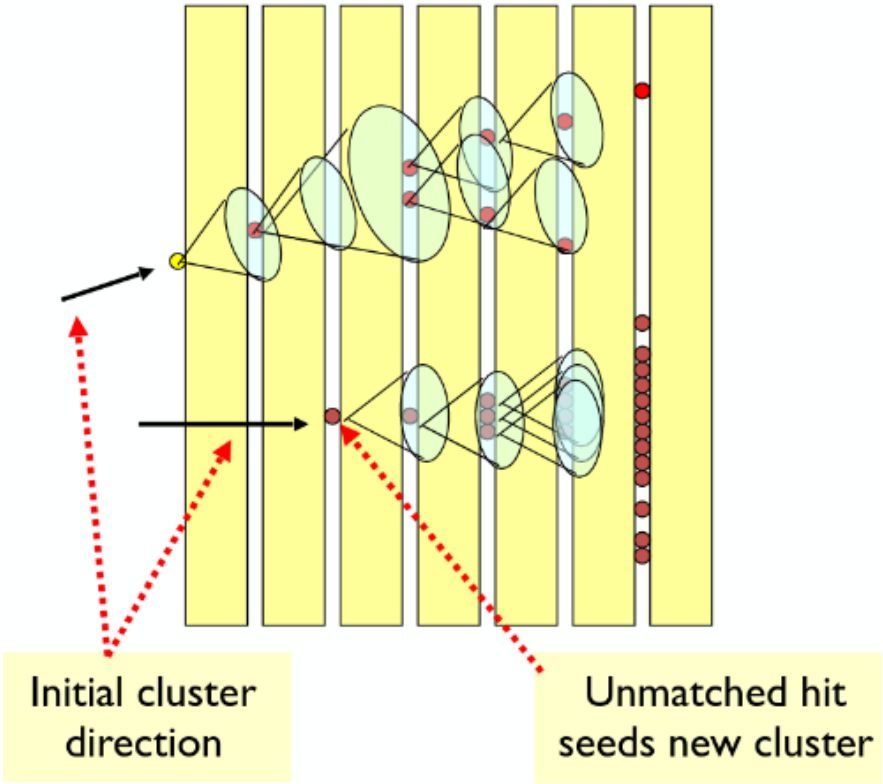

Figure 69: Illustration of the cone-based clustering algorithm used in PandoraPFA, taken from [68]

4. **Topological Cluster Merging** Cluster fragments produced by the initial clustering algorithm are then merged together by a series of algorithms, each of which follows well-defined topological signatures, listed in Figure 70. In this step clusters that are not already associated to tracks (neutral clusters) are merged with clusters which have an associated tracks (charged clusters).

   In particular the possible topological merging procedure that can be performed are:

i Looping tracks: tracks that, due to the high magnetic field, turn back are initially reconstructed as two track-like clusters. The two segments are then projected forward and the clusters are combined if the distance of closest approach of the two projections is less than a prefixed value.

ii Broken tracks: non continuous tracks in the calorimeter can arise when particles cross gaps between subdetectors or dead regions of the calorimeters. The clusters may be merged if the distance of closest approach is small enough.

iii Tracks pointing to showers: in this case the projected forward track-like charged cluster points to the starting point of a cluster located deeper in the calorimeter, and they can be merged.

iv Track-like clusters pointing back to hadronic interaction: if a neutral cluster is track-like segment whose pojection points to a hadronic interaction of charged cluster, the neutral cluster can be merged

v Back scattered tracks: Hadronic interactions can produce particles that propagates backward in the calorimeter, while the clustering algorithm has a forward projective nature, then clusterize them separately. Back-scattered tracks are then identified and merged to the charged cluster if their track-like cluster points to it.

vi Hadronic interactions pointing to neutral clusters: in this case the charged cluster has track-like segments pointing to a cluster located deeper in the calorimeter.

vii Proximity-based merging: by looking at the minimum distance between a neutral and a charged cluster (that is defined as the smaller distance between any of the hits in the two clusters), they can be merged together. In this case the consistency between the associated track momentum and the sum of the energy of the neutral and charged clusters is checked, in order to avoid false matches.

viii Cone-based merging: a cone is defined in the direction of the track-like segment of the charged cluster. Neutral clusters found inside of this cone deeper in the calorimeter can be merged to the cluster.

ix Photon recovery: in dense jets minimum ionizing particles and photons can be reconstructed together as a single cluster. In some cases the hadronic interactions can happen at a certain distance after the end of the electromagnetic shower, then photons overlapping with charged clusters can be recovered.

5. **Statistical Re-clustering** The reclustering step is peformed if there are discrepancy between the cluster energy and any associated track momenta. If these do not agree, clustering algorithms described in point 3. and 4. are run again, with different configuration parameters.

6. **Photon Recovery and Identification** The transverse and longitudinal profile of the energy deposition as a function of number of radiation length from the starting point of the shower in the electromagnetic calorimeter is compared to that expected for an electromagnetic shower. This is exploited to identify clusters of calorimeter hits consistent with photons and to recover photons merged with clusters associated with an hadronic shower.

7. **Fragment Removal** The remaining neutral clusters, not identified as photons, are selected. They can be originated by charged particle hadronic showers, then an attempt to merge them with the appropriate parent cluster is made. The consistency between the track and cluster association is always taken into account when new neutral clusters are merged to the charged one.

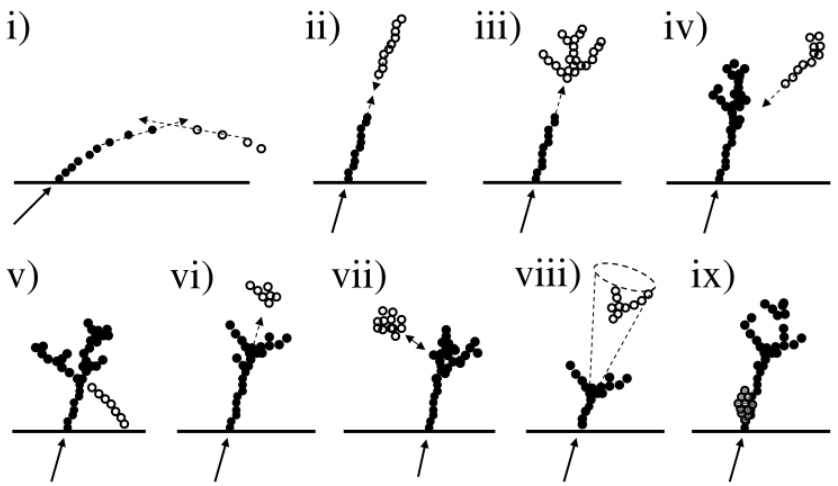

Figure 70: Main topological rules for cluster merging: i) looping track segments; ii) track segments with gaps; iii) track segments pointing to hadronic showers; iv) track-like neutral clusters pointing back to hadronic shower; v)back-scattered tracks from hadronic showers; vi) neutral clusters which are close to a charged cluster; vii) a neutral cluster near to a charged cluster; viii)cone association; ix) recovery of photons which overlap with a track segment. The open points represent neutral cluster, while the arrows represent the tracks. The filled points represent the hits of the clusters associated to the tracks.

8. **Formation of Particle Flow Objects** In this final stage reconstructed particle are created from the results of previous steps. The energy for charged particles is calculated from the track momenta, while neutral particle energies are taken from the calorimeter measurements. Furthermore, the different electromagnetic and hadronic scales are applied to the output neutral particle energies depending on whether the neutral cluster is consistent with a photon.

References

[1] Graham Shaw Franz Mandl. *Quantum field theory*. 2nd edition, Cap. 17-18.

[2] J. Beringer et al. Particle Data Group. *Review of Particle Physics (RPP)*. Phys. Rev. D86 (2012)010001.

[3] J. de Blas et al. "Higgs Boson Studies at Future Particle Colliders". In: (2020). DOI: 10.1007/JHEP01(2020)139. arXiv: 1905.03764 [hep-ph].

[4] Georges Aad et al. "Measurements of the Higgs boson production and decay rates and constraints on its couplings from a combined ATLAS and CMS analysis of the LHC pp collision data at $\sqrt{s} = 7$ and 8 TeV". In: *JHEP* 08 (2016), p. 045. DOI: 10.1007/JHEP08(2016)045. arXiv: 1606.02266 [hep-ex].

[5] J. Ellis and T. You. "Updated global analysis of Higgs couplings". In: *JHEP06(2013) 103, arXiv:* (2013). arXiv: 1303.3879[hep-ph].

[6] Richard Keith Ellis et al. "Physics Briefing Book: Input for the European Strategy for Particle Physics Update 2020". In: (Oct. 2019). arXiv: 1910.11775 [hep-ex].

[7] A. Abada et al. "FCC Physics Opportunities: Future Circular Collider Conceptual Design Report Volume 1". In: *Eur. Phys. J. C* 79.6 (2019), p. 474. DOI: 10.1140/epjc/s10052-019-6904-3.

[8] P. Bambade et al. *The International Linear Collider: A Global Project*. 2019. arXiv: 1901.09829[hep-ex].

[9] CLIC Collaboration CLICdp. "The Compact Linear Collider (CLIC) - 2018 Summary Report". In: CERN Yellow Rep. Monogr. *1802 (2018), 1-19* (2018). DOI: https://doi.org/10.23731/CYRM-2018-002.

[10] CEPC Study Group Collaboration. "CEPC Conceptual Design Report: Volume 2- Physics & Detector". In: *IHEP-CEPC-DR-2018-02, IHEP-EP-2018-01, IHEP-TH-2018-01* (2019). arXiv: 1811.10545[hep-ex].

[11] J-P. Delahaye et al. "Enabling Intensity and Energy Frontier Science with a Muon Accelerator Facility in the U.S.: A White Paper Submitted to the 2013 U.S. Community Summer Study of the Division of Particles and Fields of the American Physical Society". In: *Community Summer Study 2013: Snowmass on the Mississippi*. Aug. 2013. arXiv: 1308.0494 [physics.acc-ph].

[12] LHC Higgs Cross Section Working. URL: https://twiki.cern.ch/twiki/bin/view/LHCPhysics/LHCHXSWG..

[13] E. Aslanides et al. "Charting the European Course to the High-Energy Frontier". In: (Dec. 2019). arXiv: 1912.13466 [hep-ex].

[14] Biagio Micco et al. "Higgs boson potential at colliders: status and perspectives". In: *Reviews in Physics* (Aug. 2020), p. 100045. DOI: 10.1016/j.revip.2020.100045.

[15] Julien Baglio, Abdelhak Djouadi, and Jérémie Quevillon. "Prospects for Higgs physics at energies up to 100 TeV". In: *Reports on progress in physics. Physical Society (Great Britain)* 79 (Nov. 2015). DOI: 10.1088/0034-4885/79/11/116201.

[16] Mauro Chiesa et al. "Measuring the quartic Higgs self-coupling at a multi-TeV muon collider". In: (Mar. 2020). arXiv: 2003.13628 [hep-ph].

[17] N. Bartosik et al. "Detector and Physics Performance at a Muon Collider". In: *Journal of Instrumentation* 15.05 (May 2020), P05001–P05001. DOI: 10.1088/1748-0221/15/05/p05001.

[18] H. Abramowicz et al. "Higgs physics at the CLIC electron–positron linear collider". In: *Eur. Phys. J. C* 77.7 (2017), p. 475. DOI: 10.1140/epjc/s10052-017-4968-5. arXiv: 1608.07538 [hep-ex].

[19] Andreas Papaefstathiou, Gilberto Tetlalmatzi-Xolocotzi, and Marco Zaro. "Triple Higgs boson production to six b-jets at a 100 TeV proton collider". In: *Eur. Phys. J. C* 79.11 (2019), p. 947. DOI: 10.1140/epjc/s10052-019-7457-1. arXiv: 1909.09166 [hep-ph].

[20] Antonio Costantini et al. "Vector boson fusion at multi-TeV muon colliders". In: May 2020. arXiv: 2005.10289 [hep-ph].

[21] G. I. Budker. *Proceedings of the VII International Conference on High Energy Accelerators*. Yerevan, 1969 (Academy of Sciences of Armenia, Yerevan, 1970), Vol. I,pp. 33–39.

[22] J.P. Delahaye et al. *Muon Colliders*. arXiv:1901.06150v1, 2019.

[23] N.V. Mokhov and S.I. Striganov. "Detector Background at Muon Colliders". In: *Physics Procedia* 37 (Apr. 2012). DOI: 10.1016/j.phpro.2012.03.761.

[24] *Accelerator physics of colliders*. URL: http://pdg.lbl.gov/2017/reviews/rpp2017-rev-accel-phys-colliders.pdf.

[25] H. Wiedemann. *Particle Accelerator Physics*. Berlin : Springer, 4th ed., 2015.

[26] D. Alesini et al. "Positron driven muon source for a muon collider". In: (May 2019). arXiv: 1905.05747 [physics.acc-ph].

[27] Mark Palmer. "The US muon accelerator program". In: *5th International Particle Accelerator Conference*. June 2014, TUPME012. DOI: 10.18429/JACoW-IPAC2014-TUPME012. arXiv: 1502.03454 [physics.acc-ph].

[28] S. D. Holmes et al. "Status and Opportunities at Project X: A Multi-MW Facility for Intensity Frontier Research". In: *CONF-13-364-AD-APC-CD-TD* (2014).

[29] Kirk T. McDonald et al. "The MERIT High-Power Target Experiment at the CERN PS". In: (2010). Ed. by Martin Comyn et al., TU4GRI03.

[30] Rolland P. Johnson. "IONIZATION COOLING". In: *Proceedings of COOL 2007, Bad Kreuznach, Germany* (2007), TUM2I04.

[31] Bogomilov et al. "Demonstration of cooling by the Muon Ionization Cooling Experiment". In: *Nature 578* (2020), pp. 53–59. DOI: https://doi.org/10.1038/s41586-020-1958-9.

[32] Alexander Wu Chao et al. *Handbook Of Accelerator Physics And Engineering (2nd Edition)*. World Scientific Publishing.

[33] M. Bonesini. "Emittance Exchange in MICE". In: European Physical Society Conference on High Energy Physics - EPS-HEP2019 -10-17 July, 2019 (2019).

[34] S.A. Bogacz et al. "RECIRCULATING LINEAR ACCELERATORS FOR FUTURE MUON FACILITIES". In: *Proceedings of IPAC'10, Kyoto, Japan* (2012), THOAMH01.

[35] D. J. SUMMERS. *MUON ACCELERATION USING FIXED FIELD, ALTERNATINGGRADIENT (FFAG) RINGS*. International publisher of Modern Physics A.

[36] J. Eldred, V. Lebedev, and A. Valishev. "Rapid-cycling synchrotron for multi-megawatt proton facility at Fermilab". In: *Journal of Instrumentation* 14.07 (July 2019), P07021–P07021. DOI: 10.1088/1748-0221/14/07/p07021.

[37] A.V. Zlobin et al. *STORAGE RING AND INTERACTION REGION MAGNETS FOR A μ^+ μ^- HIGGS FACTORY*. FERMILAB-CONF-13-411-APC-TD, 2013.

[38] A.V. Zlobin et al. *MAGNET DESIGNS FOR MUON COLLIDER RING AND INTERACTION REGIONS*. FERMILAB-CONF-10-132-APC-TD, 2012.

[39] Y. Alexahin et al. *A 3-TeV MUON COLLIDER LATTICE DESIGN*. Proceedings of IPAC2012, 2012.

[40] M-H. Wang et al. *Design of a 6 TeV Muon Collider*. IPAC-2015-TUPTY081, FERMILAB-CONF-15-588-APC, SLAC-PUB-16288, 2015.

[41] Harms USPAS notes Barletta Spentzouris. URL: https://uspas.fnal.gov/materials/10MIT/Emittance.pdf.

[42] N.V. Mokhov, S.I. Striganov, and I.S. Tropin. "Reducing Backgrounds in the Higgs Factory Muon Collider Detector". In: (2014), pp. 1081–1083. DOI: 10.18429/JACoW-IPAC2014-TUPRO029. arXiv: 1409.1939 [physics.ins-det].

[43] C.J. Johnstone and N.V. Mokhov. "Optimization of a muon collider interaction region with respect to detector backgrounds and the heat load to the cryogenic systems". In: *eConf* C960625 (1996), ACC030.

[44] N.V. Mokhov and S.I. Striganov. "Simulation of backgrounds in detectors and energy deposition in superconducting magnets at $\mu^+\mu^-$ colliders". In: *AIP Conf. Proc.* 372.1 (1996). Ed. by J.C. Gallardo, pp. 234–256. DOI: 10.1063/1.50907.

[45] N.V. Mokhov et al. "The Higgs Factory muon collider superconducting magnets and their protection against beam decay radiation". In: *Journal of Instrumentation* 13 (Oct. 2018), P10024–P10024. DOI: 10.1088/1748-0221/13/10/P10024.

[46] N. Bartosik. *Beam background simulation with the CLIC framework*. URL: https://indico.cern.ch/event/876797/contributions/3706171/attachments/1974853/3286503/2020_01_23_bartosik_v0.pdf.

[47] Dominik Arominski et al. "A detector for CLIC: main parameters and performance". In: (Dec. 2018). arXiv: 1812.07337 [physics.ins-det].

[48] C. Gatto et al. *The IlcRoot FrameWork*. URL: http://www.dmf.unisalento.it/~danieleb/IlcRoot/.

[49] Niloufar Alipour Tehrani et al. "CLICdet: The post-CDR CLIC detector model". In: (2017), CLICdp-Note-2017–001.

[50] Ulrike Schnoor. URL: https://indico.cern.ch/event/947018/contributions/3980430/attachments/2089524/3510821/UlrikeSchnoor_2020-08-20-DelphesMuColl.pdf.

[51] ILCSoft repository. URL: https://github.com/iLCSoft.

[52] Markus Frank et al. "DD4hep: A Detector Description Toolkit for High Energy Physics Experiments". In: *J. Phys. Conf. Ser.* 513 (2014). Ed. by D.L. Groep and D. Bonacorsi, p. 022010. DOI: 10.1088/1742-6596/513/2/022010.

[53] S. Agostinelli et al. Geant4 collaboration. "Geant4: A simulation toolkit". In: *Nucl. Instrum.Meth.A506(2003) 250* (2003).

[54] S. Agostinelliet al. Geant4 collaboration. *Geant4 developments and applications*. IEEETrans. Nucl. Sci.53(2006) 270, 2006.

[55] ILCSoft repository. URL: https://github.com/iLCSoft/Marlin.

[56] E. Brondolin et al. "Conformal tracking for all-silicon trackers at future electron–positron colliders". In: *Nuclear Instruments and Methods in Physics Research Section A: Accelerators, Spectrometers, Detectors and Associated Equipment* 956 (Dec. 2019), p. 163304. DOI: 10.1016/j.nima.2019.163304.

[57] W. Riegler and G. Aglieri Rinella. "Time resolution of silicon pixel sensors". In: *Journal of Instrumentation* 12.11 (Nov. 2017), P11017–P11017. DOI: 10.1088/1748-0221/12/11/p11017.

[58] M. Hansroul, H. Jeremie, and D. Savard. “FAST CIRCLE FIT WITH THE CONFORMAL MAPPING METHOD”. In: (Nov. 1988).

[59] A. Glazov et al. “Filtering tracks in discrete detectors using a cellular automaton”. In: *In:Nucl. Instrum. Meth.A329.1* (1993). DOI: DOI:10.1016/0168-9002(93)90945-E.

[60] M. B. Kennel. “KDTREE 2: Fortran 95 and C++ software to efficiently search for near neighborsin a multi-dimensional Euclidean space”. In: *arXiv:0408067v2.* (2004).

[61] K. Fujii. *Extended Kalman Filter*. URL: http://www-jlc.kek.jp/subg/offl/kaltest/doc/ReferenceManual.pdf.

[62] M.A. Thomson J.S. Marshall. *The Pandora Software Development Kit for Pattern Recognition*. 2015. DOI: https://doi.org/10.1140/epjc/s10052-015-3659-3.

[63] Matteo Cacciari et al. *FastJet user manual*. CERN-PH-TH/2011-297, 2011.

[64] M.A. Thomson J.S. Marshall. “Pandora Particle Flow Algorithm”. In: (Aug. 2013). arXiv: 1308.4537v1.

[65] M. Thomson. “Particle Flow Calorimetry and the PandoraPFA Algorithm”. In: *Nuclear Instruments and Methods in Physics Research Section A Accelerators Spectrometers Detectors and Associated Equipment* 611 (July 2009). DOI: 10.1016/j.nima.2009.09.009.

[66] PandoraPFA repository. URL: https://github.com/PandoraPFA.

[67] Huong Lan Tran et al. “Software compensation in Particle Flow reconstruction”. In: *Eur. Phys. J. C* 77.10 (2017), p. 698. DOI: 10.1140/epjc/s10052-017-5298-3. arXiv: 1705.10363 [physics.ins-det].

[68] J. S. Marshall. *Presentation on PandoraPFA with LC Reconstruction*. URL: https://github.com/PandoraPFA/Documentation/blob/master/Pandora_LC_Reconstruction.pdf.

[69] S. Catani et al. “Longitudinally invariant K_t clustering algorithms for hadron hadron collisions”. In: *Nucl. Phys. B* 406 (1993), pp. 187–224. DOI: 10.1016/0550-3213(93)90166-M.

[70] *The WHIZARD Event Generator*. URL: https://whizard.hepforge.org/.

[71] A. Hoecker et al. *Toolkit for Multivariate Data Analysis with ROOT*.

[72] L. Breiman et al. *Classification and regression trees*. Wadsworth international group,Belmont, California, USA, 1984.

[73] R. Tibshirani T. Hastie and J. Friedman. *The Elements of Statistical Learning: Data Mining, Inference, and Prediction, Second Edition*. 2009, Springer New York.

[74] Ilya Narsky and Frank C. Porter. *Statistical Analysis Techniques in Particle Physics*. Wiley-VCH. ISBN : 978-3-527-41086-6, 2013.

[75] Yoav Freund and Robert E. Schapire. “Experiments with a New Boosting Algorithm”. In: *Proceedings of the Thirteenth International Conference on International Conference on Machine Learning*. ICML’96. Bari, Italy: Morgan Kaufmann Publishers Inc., 1996, pp. 148–156. ISBN: 1558604197.

[76] P Speckmayer at al. *The Toolkit for Multivariate Data Analysis, TMVA 4*. publisher of Physics: Conference Series219(2010) 032057, 2010.

[77] Richard Wigmans. *New Developments in Calorimetric Particle Detection*. arXiv:1807.03853v1, 2018.